Fluorescence correlation spectroscopy studies of diffusion in and over nanostructured soft and hard materials

by

Omid Shafiee

B.S., Shiraz University, 2010
M.S., Tarbiat Modares University, 2013

AN ABSTRACT OF A DISSERTATION

submitted in partial fulfillment of the requirements for the degree

DOCTOR OF PHILOSOPHY

Department of Chemistry
College of Arts and Sciences

KANSAS STATE UNIVERSITY
Manhattan, Kansas

2024

Abstract

This dissertation explores mass transport of molecules confined within soft and hard nanostructures, by employing the method of fluorescence correlation spectroscopy (FCS). FCS is a single molecule spectroscopy method that allows for the study of diffusion by fluorescent molecules at a (far)-sub-ensemble level. Lyotropic liquid crystals (LLCs) made from $C_{12}EO_{10}$ surfactants comprised the soft matter nanostructures explored in this dissertation. The hard matter nanostructures included nanoporous anodic aluminum oxide (AAO) membranes and polyethylene terephthalate (PET) microplastic surfaces. Nile red (NR) and Rhodamine B (RhB) were two fluorescent probes that were used in these studies.

In the first study, solute diffusion within LLC gels prepared from a series of water and decaethylene glycol monododecyl ether ($C_{12}EO_{10}$) mixtures was explored using variable area fluorescence correlation spectroscopy (va-FCS). Aqueous $C_{12}EO_{10}$ gels were prepared in concentrations ranging from 55:45 to 70:30 wt% surfactant to water. Three different NR dyes were employed as model solutes. Each was separately doped into the LLC gels at nanomolar concentrations. Included were a hydrophilic form of NR incorporating an anionic sulfonate group ($NRSO_3^-$), a hydrophobic form with a fourteen-carbon alkane tail (NRC_{14}), and the commercial NR as an intermediate case. FCS data acquired from the gels showed that $NRSO_3^-$ diffused primarily in three dimensions, with its diffusion coefficient decreasing monotonically as gel concentration and micelle packing density increased. This behavior is consistent with the confinement of $NRSO_3^-$ by exclusion from the micelle cores. NRC_{14} exhibited the smallest diffusion coefficient, likely due to its larger size and enhanced interactions with the micelle cores. Commercial NR displayed an intermediate diffusion coefficient and the most anomalous behavior of the three dyes. The latter was attributed to its facile partitioning between core and corona regions

of the micelles, and greater participation in one-dimensional diffusion. The results from these studies enhance our understanding of molecular mass transport through soft-matter nanomaterials, such as those being developed for drug delivery and membrane-based chemical separations.

In the second study, FCS was utilized to investigate organic molecules adsorbed from aqueous solution onto the surfaces of synthetic secondary microplastics. Both fresh and artificially aged PET plastics were employed. The plastics were artificially aged in a UV-ozone chamber. Raman and infrared spectra confirmed the composition of the PET microplastics. Water contact angle and surface roughness measurements revealed an increase in wettability and surface roughness with aging, consistent with oxidation of the plastic surface. Rhodamine B dye was used as a fluorescent probe in FCS studies and served as an analogue for organic pollutants commonly found on microplastics. The FCS results revealed the accumulation of dye on the PET surfaces as they were aged. Dye motion was significantly slower on the plastics than in bulk aqueous solution and occurred by anomalous sub diffusion. The rate of diffusion became dramatically slower and more anomalous as the plastics were aged. Surface diffusion is likely slowed by either ionic interactions or hydrogen bonding between the dye and plastic. These results provide new insights critical to understanding how microplastics accumulate and transport organic pollutants as they weather in the environment.

In the third study, the diffusion of NR doped toluene-ethanol mixtures confined within 10 nm and 20 nm AAO nanopores was investigated. The results showed two distinct diffusion components, characterized as fast and slow diffusion. The fast diffusion coefficient (D_f) was attributed to molecules that pass through the cylindrical pores largely unimpeded. However, the D_f values were consistently smaller than the bulk diffusion coefficient (D_b), with further reduction observed in 10 nm pores compared to 20 nm pores. This reduction in diffusion coefficient is attributed to long range dipole-dipole interactions between the pore surface and NR molecules. Additionally, D_f values were correlated with mixture composition, mirroring the trend observed for D_b, thus reflecting their dependence on solution viscosity. The slow diffusion coefficient (D_s) values were markedly smaller than D_f but also followed the viscosity-dependent trends in D_b. The D_s values were more than one- and two-orders-of-magnitude smaller than $D_{\mathbf{b}}$ for the 20 nm and 10 nm pores, respectively. The dramatic reduction in the rate of diffusion by the slow mechanism was attributed to adsorption of the dye to the pore surface by a hydrogen bonding mechanism. These findings contribute to a deeper understanding of diffusion through nanoporous structures and the effects of nanoconfinement. The knowledge gained will allow for optimization of the performance of nanomaterials being developed for use in chemical separation. This new knowledge will also afford an improved understanding of the role played by nanoconfinement in gas and oil production from nanoporous shale rocks.

Fluorescence correlation spectroscopy studies of diffusion in and over nanostructured soft and hard materials

by

Omid Shafiee

B.S., Shiraz University, 2010
M.S., Tarbiat Modares University, 2013

A DISSERTATION

submitted in partial fulfillment of the requirements for the degree

DOCTOR OF PHILOSOPHY

Department of Chemistry
College of Arts and Sciences

KANSAS STATE UNIVERSITY
Manhattan, Kansas

2024

Approved by:

Major Professor
Professor Daniel A. Higgins

Copyright

Abstract

This dissertation explores mass transport of molecules confined within soft and hard nanostructures, by employing the method of fluorescence correlation spectroscopy (FCS). FCS is a single molecule spectroscopy method that allows for the study of diffusion by fluorescent molecules at a (far)-sub-ensemble level. Lyotropic liquid crystals (LLCs) made from $C_{12}EO_{10}$ surfactants comprised the soft matter nanostructures explored in this dissertation. The hard matter nanostructures included nanoporous anodic aluminum oxide (AAO) membranes and polyethylene terephthalate (PET) microplastic surfaces. Nile red (NR) and Rhodamine B (RhB) were two fluorescent probes that were used in these studies.

In the first study, solute diffusion within LLC gels prepared from a series of water and decaethylene glycol monododecyl ether ($C_{12}EO_{10}$) mixtures was explored using variable area fluorescence correlation spectroscopy (va-FCS). Aqueous $C_{12}EO_{10}$ gels were prepared in concentrations ranging from 55:45 to 70:30 wt% surfactant to water. Three different NR dyes were employed as model solutes. Each was separately doped into the LLC gels at nanomolar concentrations. Included were a hydrophilic form of NR incorporating an anionic sulfonate group ($NRSO_3^-$), a hydrophobic form with a fourteen-carbon alkane tail (NRC_{14}), and the commercial NR as an intermediate case. FCS data acquired from the gels showed that $NRSO_3^-$ diffused primarily in three dimensions, with its diffusion coefficient decreasing monotonically as gel concentration and micelle packing density increased. This behavior is consistent with the confinement of $NRSO_3^-$ by exclusion from the micelle cores. NRC_{14} exhibited the smallest diffusion coefficient, likely due to its larger size and enhanced interactions with the micelle cores. Commercial NR displayed an intermediate diffusion coefficient and the most anomalous behavior of the three dyes. The latter was attributed to its facile partitioning between core and corona regions

of the micelles, and greater participation in one-dimensional diffusion. The results from these studies enhance our understanding of molecular mass transport through soft-matter nanomaterials, such as those being developed for drug delivery and membrane-based chemical separations.

In the second study, FCS was utilized to investigate organic molecules adsorbed from aqueous solution onto the surfaces of synthetic secondary microplastics. Both fresh and artificially aged PET plastics were employed. The plastics were artificially aged in a UV-ozone chamber. Raman and infrared spectra confirmed the composition of the PET microplastics. Water contact angle and surface roughness measurements revealed an increase in wettability and surface roughness with aging, consistent with oxidation of the plastic surface. Rhodamine B dye was used as a fluorescent probe in FCS studies and served as an analogue for organic pollutants commonly found on microplastics. The FCS results revealed the accumulation of dye on the PET surfaces as they were aged. Dye motion was significantly slower on the plastics than in bulk aqueous solution and occurred by anomalous sub diffusion. The rate of diffusion became dramatically slower and more anomalous as the plastics were aged. Surface diffusion is likely slowed by either ionic interactions or hydrogen bonding between the dye and plastic. These results provide new insights critical to understanding how microplastics accumulate and transport organic pollutants as they weather in the environment.

In the third study, the diffusion of NR doped toluene-ethanol mixtures confined within 10 nm and 20 nm AAO nanopores was investigated. The results showed two distinct diffusion components, characterized as fast and slow diffusion. The fast diffusion coefficient (D_f) was attributed to molecules that pass through the cylindrical pores largely unimpeded. However, the D_f values were consistently smaller than the bulk diffusion coefficient (D_b), with further reduction observed in 10 nm pores compared to 20 nm pores. This reduction in diffusion coefficient is attributed to long range dipole-dipole interactions between the pore surface and NR molecules. Additionally, D_f values were correlated with mixture composition, mirroring the trend observed for D_b, thus reflecting their dependence on solution viscosity. The slow diffusion coefficient (D_s) values were markedly smaller than D_f but also followed the viscosity-dependent trends in D_b. The D_s values were more than one- and two-orders-of-magnitude smaller than $D_{\mathbf{b}}$ for the 20 nm and 10 nm pores, respectively. The dramatic reduction in the rate of diffusion by the slow mechanism was attributed to adsorption of the dye to the pore surface by a hydrogen bonding mechanism. These findings contribute to a deeper understanding of diffusion through nanoporous structures and the effects of nanoconfinement. The knowledge gained will allow for optimization of the performance of nanomaterials being developed for use in chemical separation. This new knowledge will also afford an improved understanding of the role played by nanoconfinement in gas and oil production from nanoporous shale rocks.

Table of Contents

List of Figures

List of Tables

Acknowledgements

Completing this PhD dissertation has been a long and challenging journey, and I would not have been able to accomplish it without the support, guidance, and encouragement of many individuals and institutions.

First and foremost, I would like to express my deepest gratitude to my supervisor, professor Daniel A. Higgins, for his unwavering support, invaluable guidance, and insightful feedback throughout this research. His mentorship has been instrumental in shaping my academic and professional growth.

I am also profoundly grateful to my dissertation committee members, Dr. Jun Li, Dr. Paul Smith, Dr. Bret Flanders, Dr. Takashi Ito, and Dr. Behzad Ghanbarian, for their time, expertise, and constructive comments, which have greatly improved the quality of this work. Additionally, I wish to extend my appreciation to my previous advisor, Dr. Viktor Chikan, and to Dr. Jun Li for encouraging me to apply to the Chemistry Department at K-State. Dr. Christer Aakeroy is also thanked for his help during the application and admission process.

I would like to extend my appreciation to the non-graduate faculty and staff of the Chemistry Department at K-State. Michael Hinton is thanked for his great support as lab director, helping me grow as a teaching assistant. Tomohiro Kimura is thanked for teaching me how to perform and analyze the PFG-NMR method. Jim Hodgson is thanked for making cylindrical glasses to use in sample cells for FCS and Raman measurements. Tingting Liu is thanked for his guidance both as lab director and safety officer. Tobe Eggers is thanked for helping in troubleshooting electronic devices. Ron Jackson is thanked for making new parts as needed for the measurements. Dr. Lianjie Xue is thanked for his help in teaching me how FCS works and how to analyze data. Dr. Akash Nathani is thanked for helping me learn AFM and analyze the data.

A heartfelt thank you to my colleagues and friends in Dr. Higgins's research group at Kansas State University, especially Hamid Rashidi, for all his guidance throughout my PhD journey, from day one to the very last day. Your camaraderie, intellectual discussions, and moral support have been a source of strength and motivation during difficult times.

I would like to acknowledge the financial support provided by the Division of Chemical Sciences, Geosciences, and Biosciences, Office of Basic Energy Sciences of the U.S. Department of Energy, the National Science Foundation (NSF), the American Chemical Society Petroleum Research Fund, the Chemistry Department at K-State, and PLU, which made this research possible.

I owe a great debt of gratitude to my family, whose unconditional love and belief in me have been my anchor throughout this journey. To my mother, "Maman," who always encouraged me to pursue my education to the next level, thank you for your endless encouragement and sacrifices. To my brother, Ali, who encouraged me to apply to universities in the United States. To my dear lovely wife, Soheila, your patience, understanding, and support have been invaluable. And to my little Hannah, you are my inspiration and joy.

Lastly, I would like to thank everyone who has contributed to my academic journey in one way or another. This accomplishment is not just mine, but a testament to the collective support and encouragement I have received from all of you.

Thank you.

Omid Shafiee

Dedication

To my beloved father, “Baba”, whom I never had a chance to say goodbye to. Your memory has been a constant source of strength and inspiration throughout this journey. This thesis is dedicated to you, with all my love and gratitude.

Chapter 1 - General Introduction

1.1 Diffusion

1.1.1 What is Diffusion?

In general, diffusion in a fluid is defined as the movement of molecules from a region of high concentration to a region of lower concentration over time. More specifically, diffusion is often categorized into two types: mutual diffusion and self-diffusion. Mutual diffusion arises when molecular motion occurs along a gradient in chemical potential, while self-diffusion occurs by the random thermally-excited (i.e., Brownian) motion of fluid molecules. The latter is the subject of this dissertation.

The term Brownian motion is frequently used to describe molecular motion in fluids in recognition of early 19th century work by Robert Brown, who reported observing the random motions of pollen particles in water under a microscope. However, it is interesting that Robert Brown was actually not the first scientist to observe these motions. Rather, it was Anton van Leeuwenhoek who observed them in the 17th century. The real cause of the observed motion remained unknown after this initial observation. Even Brown himself was unsure about their origins. He wrote "I have formerly stated my belief that these motions of the particles neither arose from currents in fluid containing them, nor depended on that intestine motion which may be supposed to accompany its evaporation"[1]. In 1905, Einstein claimed that "according to the molecular-kinetic theory of heat, bodies of microscopically visible size suspended in a liquid will perform movements of such magnitude that they can be easily observed in a microscope, on account of the molecular motions of heat. It is possible that the movements to be discussed here are identical with the so-called Brownian molecular motion"[2]. Today, we know that Brownian motion is caused by the internal kinetic energy of molecules and their collision with each other.

The rate of diffusion can be measured as the mean squared displacement (MSD) of particles as a function of time and has the SI unit of $\frac{m^2}{s}$. The reason that the mean *squared* distance is used is because of the random nature of Brownian motion. The mean displacement is actually zero, while the mean squared displacement increases in time. Diffusion provides valuable information about the environment in which it occurs, whether it is a confined space, such as a pore, in a membrane, on a surface, or in bulk solution. The rate of diffusion is quantified by the diffusion coefficient, *D*, where MSD = *nDt*, in which n is the dimensionality of molecular motion, and t is time. Most commonly, *D* is related to physical parameters such as the viscosity of the local environment. In this dissertation, diffusion measurements are instead focused on understanding how confinement of molecular motions affects the MSD[3]. To quantify the rate of diffusion, that is to determine the diffusion coefficient, it is imperative to know the parameters affecting it.

1.1.2 Parameters Affecting Diffusion

There are three main factors influencing diffusion. These are temperature, size of the diffusing molecule and the viscosity of the environment. These factors are related to each other by the Stokes-Einstein-Sutherland equation:

$$D = \frac{K_B T}{\xi} \qquad \text{Equation 1.1.}$$

where D is again the diffusion coefficient in $\boldsymbol{\frac{m^2}{s}}$, K_B is the Boltzmann constant in $\boldsymbol{\frac{J}{K}}$, T is temperature in K and $\boldsymbol{\xi}$ is the friction coefficient in $\boldsymbol{\frac{J.s}{m^2}}$. The friction coefficient of a spherical particle can be calculated using Equation 1.2.

$$\xi = b\pi\eta R_H \qquad \text{Equation 1.2.}$$

where R_H is the hydrodynamic radius of the particle in meters, η is the viscosity of the environment in Pa·s and b depends on the boundary condition of the particle-solvent interface. In most cases, it is assigned a value of 6. Combining Equation 1.1 and Equation 1.2 gives Equation 1.3, which is commonly used to calculate the diffusion coefficient of a spherical particle in solution[3,4].

$$D = \frac{K_B T}{6\pi\eta R_H} \qquad \text{Equation 1.3.}$$

Finally, the diffusion coefficient, diffusion time and MSD are related by Equation 1.4,

$$MSD = <(r_1 - r_0)^2> = nDt \qquad \text{Equation 1.4.}$$

where $<(r_1-r_0)>^2$ is the mean squared displacement in m^2, t is diffusion time in seconds and the value of n is 2, 4, or 6 for one-, two-, or three-dimensional diffusion, respectively [3]. Equation 1.3 and Equation 1.4 apply specifically to free diffusion, where there is neither a means of restriction to the movement of molecules nor any force moving the molecules in a particular direction. In reality, many systems show restricted or hindered diffusion[3]. For instance, consider a molecule of 1 nm size moving inside a 10 nm pore. Its movement in this nanoconfined space would differ significantly from its movement in bulk solution. There should be parameters other than temperature and viscosity that are affecting its diffusion. Parameters such as electrostatic interactions and hydrogen bonding between the molecule and the pore surface. All such interactions exhibit a strong dependence on distance, and so, the pore size also plays a crucial role in limiting the diffusion behavior of molecules confined within them.

Understanding the dynamics of diffusion within these confined nanoscale spaces holds considerable importance. Addressing questions about the impact of pore size, interactions, and the broader significance of diffusion in such restricted environments is essential. These inquiries will be explored in the course of this dissertation. First, however, this dissertation delves into the importance of nanoconfinement, its potential applications, and prior research in the field is reviewed.

1.1.3 Diffusion in Nanoconfined Spaces

Nanoconfinement and the behavior of molecules in nanoconfined spaces both in soft and hard matter are important because of their numerous applications. One of the most important applications of nanoconfinement is drug delivery. Many drug delivery carriers have porous structures, such as carbon nanotubes[5] and mesoporous silica[6]. Nanoconfinement affords a means of protecting drug molecules from degradation prior to reaching the intended site of action and also a potential means for guiding or timing their release into those environments. The availability of these drugs then depends on how nanoconfinement limits their motions.

Beyond drug delivery, investigating diffusion in nanoconfined spaces is vital for other applications including in catalysts[7-11], energy storage[12-15], sensors[16-19], water purification[20-23], biomedical imaging[24,25], cancer treatment[26,27] and liquid crystals[28-30]. This vast spectrum of applications emphasizes the importance of molecular diffusion within confined nanoscale environments. Such understanding is essential for advancing technologies and optimizing performance across diverse fields.

Dong et al[7] investigated nanoconfinement within core-shell nanoporous catalysts using single molecule imaging techniques. They reported that nanoconfinement leads to unusual behaviors such as lower adsorption strength but higher catalytic activity. Their work highlights the importance of understanding the fundamental aspects of confinement effects to engineer more efficient catalysts.

In a more recent publication[10], the same group of researchers have reported the contradictory behavior of faster reaction rate and higher activation energy in hydrophobic nanopores, which was attributed to confinement effects. In other work, Wordsworth et al[9] authored a review article on the effects of nanoconfinement on electrocatalysis. They concluded that even though studies of nanoconfinement in electrochemistry are becoming more common, only a nascent understanding of its importance exists at present. Furthermore, they note that the utilization of nanoconfinement as a route to improving electrocatalysis requires further investigation to fully understand what can be achieved. Fichtner[12] in his study on nanoconfinement effects on energy storage materials have concluded that these effects can be used to optimize the electrochemical potential and the overpotentials during charge and discharge cycles. Nielsen et al[13] and Comanescu[14] independently published two review papers on nanoconfined hydrides for energy storage. They both demonstrated that nanoconfined metal hydrides have great potential for energy storage applications because they can improve hydrogen desorption kinetics and thermodynamic properties. Their analyses highlighted the capacity of nanoconfined systems to enhance hydrogen desorption kinetics and thermodynamic properties. Notably, a thorough review of existing studies revealed a marked enhancement in kinetics within nanoconfined spaces compared to bulk systems. Khatri et al[18] studied the impact of nanoconfinement on single molecule detection of small molecules with nanopipettes. They reported a great increase in sensitivity with increased nanoconfinement. Qian et al[20] conducted an extensive review on the application of nanoconfinement in water treatment. They reported that water molecules show unique structural, thermodynamic, and dynamic properties, due to changes in the structure of the hydrogen bond network in nanoconfined spaces compared to bulk solution. They reported formation of one or several ordered layers of water on the pore wall. These layers have a different density from bulk solution, a different number of hydrogen bonds per molecule than in bulk solution, and the molecules tend to be oriented. Formation of such surface layers have been reported elsewhere as well[31]. However, they emphasized the necessity for further studies to deepen the comprehension of nanoconfinement effects on water molecules[20]. Koone et al[32] explored liquid diffusion in porous sol-gel glass. They found that the sticking of polar molecules to the pore surface reduces the effective pore size, resulting in a slowing of their motion. They also found that liquids having large dipole moments move faster than those with smaller dipole moments. This surprising result was attributed to faster motion of the molecules with larger dipole moments near the surface of the pores Kang et al[26] studied the influence of nanoconfinement on cancer theranostics using gold nanoparticles. They concluded that even though gold nanoparticles have important emerging applications in cancer theranostics, these have been limited by low imaging resolution, insufficient heat production, and low sensitivity. They proposed employing nanoconfinement of gold nanoparticles within other nanoparticles (known as particle-in-particle or PIP materials) to overcome these constraints. Finally, Thompson[33] reviewed studies of solvation dynamics in nanoconfined liquids and concluded that "*The chemical dynamics of liquids confined on nanometer length scales are an exciting area of research with much left to understand*" and *"…nanoconfined liquids are relevant to a wide range of potential applications, which will be furthered by a better understanding of their properties*". These constitute two main motivations of the work performed for this dissertation.

The above literature review has highlighted the need for further studies of nanoconfinement due to its applications across diverse fields. The following section provides an elucidation of the research projects undertaken for this dissertation. They encompass investigations of both soft and hard nanostructures. These projects are aimed at contributing substantively to the understanding of nanoconfinement and in helping to identify its potential implications for advancements in various scientific and technological domains.

1.2 Objectives and Motivations

In seeking to understand how soft matter nanostructures may affect molecular diffusion, one project was undertaken to investigate the diffusion behavior of NR and its derivatives within nanostructured LLCs composed of $C_{12}EO_{10}$. Variable area-fluorescence correlation spectroscopy (va-FCS), fluorescence spectroscopy, and small angle x-ray scattering (SAXS) were used to study the diffusion of the NR dyes and for characterization of the LLCs, respectively. The aqueous LLCs exhibit a distinct structure that includes a hydrophobic core surrounded by a hydrophilic corona region. The main focus of the work was to investigate how the polarity of dye molecules affects its partitioning within this structure. Despite the widespread applications of LLCs, the mass transport dynamics of guest molecules within them remain inadequately explored. A better understanding of these dynamics is necessary to optimize them for any potential applications, such as in water filtration membranes. This knowledge gap served as the principal motivation behind this study. The results revealed the challenging nature of discerning the effects of confinement in soft matter systems.

To better uncover such phenomena, studies of hard matter nanomaterials in which dense physical features rigorously block diffusive motion were also investigated. The focus of the research project in this case was centered on exploring the diffusion rate and mechanism of NR dye in a series of toluene-ethanol mixtures confined within nanoporous AAO membranes, using FCS. The AAO membranes employed had pore sizes of 10 and 20 nm. The findings revealed compelling evidence of adsorption, surface diffusion, and subsequent desorption of dye molecules from the pore surfaces in both 10 nm and 20 nm membranes. Further investigation of the time transients via autocorrelation function analysis revealed two distinct mechanisms for the diffusion of NR confined within solvent-filled 10 nm and 20 nm AAO membranes: slow and fast diffusion.

The fast diffusion component was associated with molecules traversing the pore without surface adsorption. Conversely, the slow component was attributed to dye molecules adsorbing to the surface, possibly diffusing on the surface, and subsequently desorbing back into solution. The findings of these investigations provide valuable insights into the behavior of solutes and solvents under nanoconfinement within AAO membrane nanopores.

As a related project, the diffusion dynamics of dye molecules over the surface of nanostructured polymeric materials were also explored. In particular, the effects of artificial weathering on the uptake and diffusion of RhB dye over polyethylene terephthalate (PET) plastics were explored by FCS. These materials served as models for microplastic particles found throughout the natural environment. Various analytical techniques were employed to assess changes in the surface composition and structure of the PET microplastics, including sessile drop contact angle measurements, Raman scattering, attenuated total internal reflection Fourier transform infrared (ATR-FTIR) spectroscopy, and atomic force microscopy (AFM). The primary objective of this research was to study surface adsorption and desorption of RhB dye as a model pollutant on the PET surface at the single molecule level. The results showed that as the PET plastic ages, its surface oxidizes, and nanostructures are formed. These increase RhB uptake by the surface. A notable decrease in RhB diffusion rate with increasing aging time was also observed and was attributed to intensified ionic and hydrogen bonding interactions between dye molecules and the aged surface of the PET microplastics.

1.3 Outline of the Dissertation

Chapter 1 provides a general introduction to the concept of diffusion, followed by a comprehensive literature review on diffusion in nanoconfined spaces. Finally, the objectives and motivation of the present dissertation are explained. Chapter 2 details the materials and the fluorescent dyes that were employed during this work. Chapter 3 elucidates the techniques and methods that were utilized to characterize the behavior of the materials. Chapters 4, 5, and 6 describe specific projects that were undertaken to fulfill the objectives of the dissertation. Chapter 4 explores dye diffusion in nanostructured lyotropic liquid crystals, while Chapter 5 covers studies of dye diffusion on microplastic surfaces, and Chapter 6 reports studies of dye diffusion in anodic alumina nanopores filled with different mixtures of toluene and ethanol. Chapter 7 summarizes the conclusions of this dissertation and gives suggestions for future work. Finally, chapter 8, provides a comprehensive list of references used in this dissertation.

Chapter 2 Materials and Fluorescent Probes

2.1 Lyotropic Liquid Crystals

Liquid crystals were initially discovered in 1888 by an Austrian scientist named Friedrich Reinitzer[34]. They represent a distinct state of matter, bridging the characteristics of crystalline structured solids and disordered liquids. This unique state of matter exhibits a degree of molecular order that is less than high level of order observed in crystalline solids while also being more ordered than common liquids. Liquid crystals also exhibit a degree of molecular mobility that is less than that of liquids and more than in solids.

Figure 2.1 shows these differences in order and mobility schematically. Depending on their formation mechanisms, liquid crystals can be classified as being either thermotropic or lyotropic. Thermotropic liquid crystals form over a specific range of temperatures whereas lyotropic liquid crystals form over specific concentration ranges by dissolving surfactants in appropriate solvents[35-38]. Lyotropic liquid crystals are exclusively explored in this dissertation and no further mention will be made of thermotropic liquid crystals.

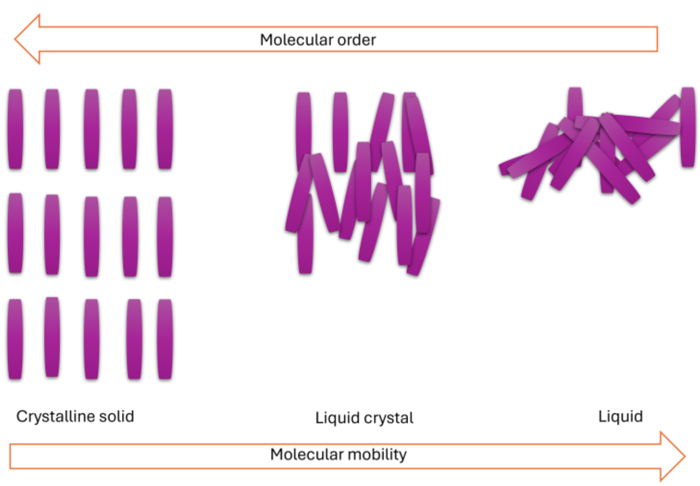

Figure 2.1. Molecular organization and mobility in solids, liquid crystals and liquids. Molecular order increases from right to left, while molecular mobility increases from left to right.

Surface-active agents (i.e., surfactants) are amphiphilic molecules incorporating both hydrophobic and hydrophilic moieties. They can be either ionic or nonionic molecules. At low concentrations in aqueous solution surfactants assemble into monolayers at the water surface. By increasing the surfactant concentration, these molecules undergo a transition called micellization, forming spherical or cylindrical structures known as micelles. The critical concentration threshold at which this transition occurs is known as the critical micelle concentration (CMC). The hydrophilic part (corona) of the micelle is in contact with water while the hydrophobic part (core) avoids water. A further increase in the surfactant concentration leads to increased organization and reduced mobility of the micelles. At relatively high concentrations, the resulting solution transitions into an organized gel that is known as a lyotropic liquid crystal (LLC). LLCs can exhibit different phases that exhibit different molecular organization. These depend upon the surfactant type, the temperature, and the surfactant concentration in solution. These phases include, but are not limited to, normal and reversed hexagonal, normal and reversed cubic, and lamellar[39-41]. The micelle shape is influenced by both intramicellar and intermicellar interactions. A typical phase diagram of an LLC is depicted in Figure 2.2.

One of the common classes of surfactant that are employed to make LLCs are the poly(oxyethylene) monoalkyl ethers. These are the surfactants used in this dissertation and are discussed further, in the next section.

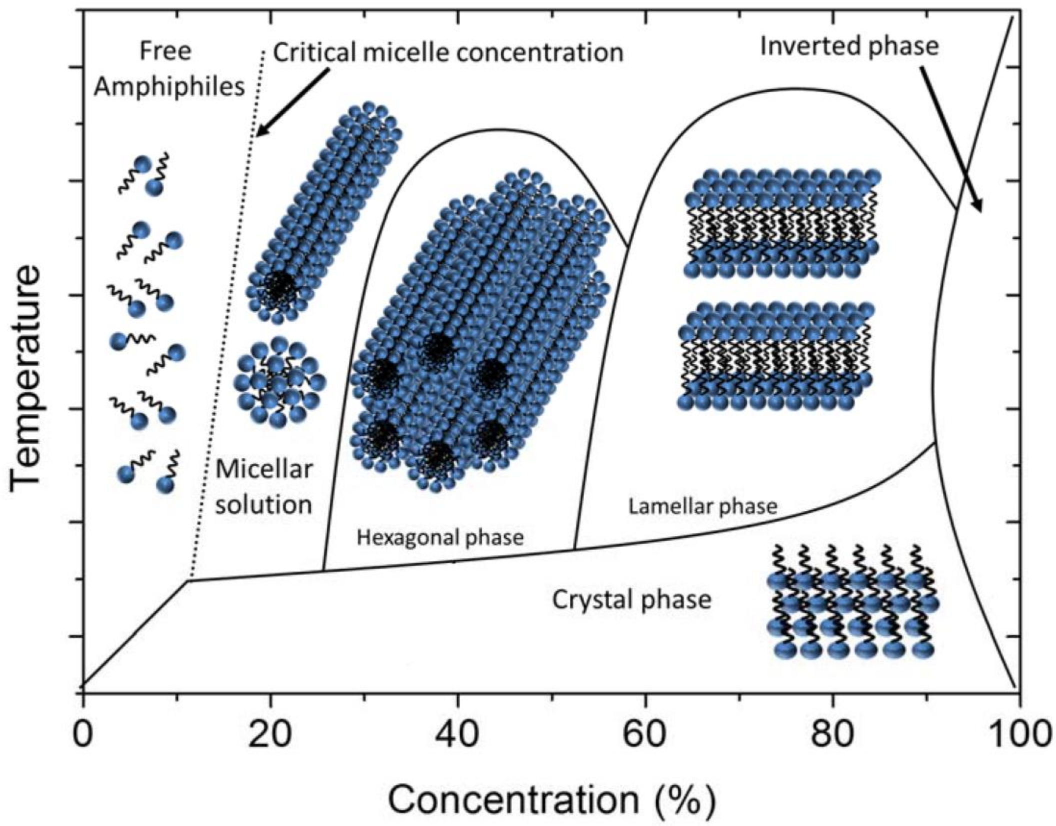

Figure 2.2. Phase diagram of a LLC which shows the structure of the LLCs and of their component micelles and lamellar structures. The x-axis could be mole, volume, or weight percent. Modified with permission from Ref. 38.

Poly(oxyethylene) monoalkyl ethers are a common class of non-ionic surfactants with wide-ranging applications in cosmetics, pharmaceutical formulations, and detergents.[39,40] Their molecular formula is $RO(C_2H_4O)_mH$ where R refers to a saturated alkyl chain and m is the number of repeated ethylene oxide (EO) groups. These surfactants are often designated by the generic formula of C_nEO_m, with n indicating the number of carbons in the alkyl chain and m the number of ethylene oxide groups. The C_nEO_m surfactants are environmentally friendly, and their properties depend on the number of hydrophilic EO groups present and the length of the hydrophobic alkyl chain. The driving forces for aggregation and micelle formation in this class of surfactants includes hydrophobic interactions, hydration, and hydrogen bonding[40]. In this dissertation, the specific surfactant under examination was $C_{12}EO_{10}$.

Decaethylene glycol monododecyl ether has an empirical formula of $C_{32}H_{66}O_{11}$. When it is mixed with water in appropriate mass ratios, it yields highly viscous and optically transparent LLCs. Within the concentration range employed in this dissertation, these LLCs are comprised of cylindrical micelles having a core diameter of a few nanometers and lengths of a few hundred nanometers. While the exact phase diagram of $C_{12}EO_{10}$ is not available in the literature, it has been reported that $C_{12}EO_{10}$ forms normal and reverse spherical micelles, and a normal hexagonal phase of cylindrical micelles. Notably, the critical micelle concentration (CMC) of $C_{12}EO_{10}$ is reported to be 9.1×10^{-5} M [28,40,41]. Figure 2.3.a. shows the molecular structure of $C_{12}EO_{10}$, while Figure 2.3.b. shows the structure of cylindrical micelles and hexagonal LLCs formed by this surfactant. The detailed procedure used for preparation of the LLCs employed in this dissertation is provided in section 4.2.1.

A primary purpose of the work performed in this dissertation was to study the mechanisms and rates of solute diffusion within nanoconfined spaces such as the LLC core, the corona regions and in the regions between. For this purpose, the fluorescent dye NR was incorporated to these LLCs at nanomolar concentrations.

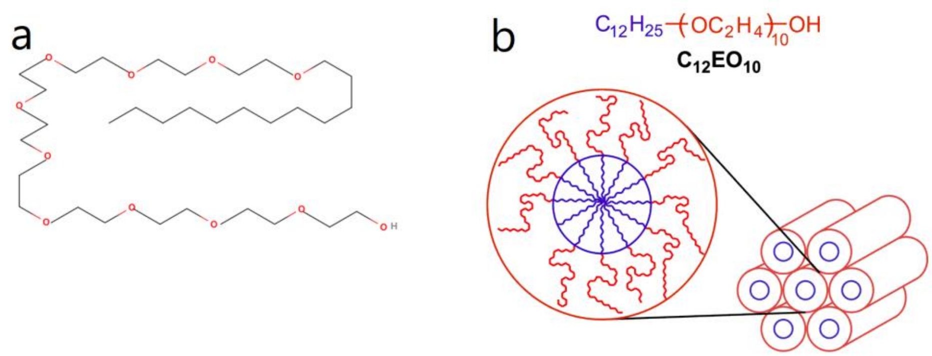

Figure 2.3. a. Molecular structure of $C_{12}EO_{10}$ and b. Hexagonal LLCs made from $C_{12}EO_{10}$. The blue part is the hydrophobic core and red part is the hydrophilic corona of the micelle, Modified from Ref. 28.

2.2 Anodic Aluminum Oxide Membranes

Nanoporous anodic aluminum oxide (AAO) possesses a honeycomb-like structure that includes arrays of parallel and uniform cylindrical pores, fabricated through an anodization process. The AAO membranes utilized in this study were purchased from InRedox, LLC and had a diameter of 10 mm, a thickness of 50 µm, pore diameters of 10 nm and 20 nm and pore densities of $12\pm\mathbf{2}\%$. Figure 2.4 presents scanning electron microscopy (SEM) images of 20 nm and 10 nm AAO membranes[31,42]. AAO membranes can serve as good models upon which to base studies of mass transport in hard nanostructures under nanoconfinement. In this study, AAO nanopores were used as models for shale samples, allowing for studies of diffusion by organic molecules under nanoconfinement. Unfortunately, real shale samples could not be employed because of the high autofluorescence of kerogen in these samples.

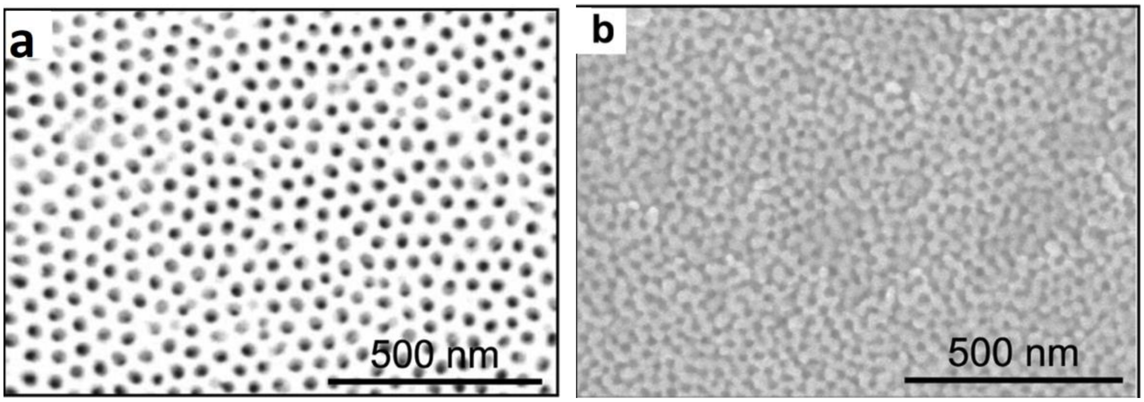

Figure 2.4. SEM images of the surface of a. 20 nm and b. 10 nm AAO membranes, reprinted with permission from Ref. 31.

2.3 Polyethylene Terephthalate Microplastic

Polyethylene terephthalate (PET) stands as one of the most widely used polymers. It is synthesized from ethylene terephthalate monomers with repeating units of $C_{10}H_8O_4$ and has a chemical formula of $(C_{10}H_8O_4)_n$[43-49]. Figure 2.5 shows the molecular structure of PET plastic. PET production has increased exponentially in the last decades. According to a 2021 analysis, around 490 billion tons of PET were manufactured in 2016 alone[43]. This number was predicted to increase to 600 billion tons in 2021. The popularity of PET originates from its excellent physical and chemical characteristics including its light weight, high strength, chemical resistance, thermal stability, impermeability to gases and liquids, and its optical transparency. These features make it ideal for use in certain applications. For instance, its oxygen impermeability makes PET a perfect choice for food packaging and beverages bottles. PET has also been approved by multiple health organizations as safe for direct contact with drinks and foods. Other applications of PET plastic include its use in medicine containers, electronic components, and in textiles (i.e., as polyester).

Plastic waste in general is becoming a major issue worldwide, and plastics that find their way into bodies of water are of special concern. Of particular alarm is the projected entry of 32 million tons of plastic waste into the Earth's oceans annually by 2050[44]. While this waste is comprised of many different plastics, PET waste is a key component. PET waste has been reported to be the second most prevalent plastic polymer detected in coral samples and deep-sea sediments in the Atlantic Ocean, the Indian Ocean, the Mediterranean Sea and on US beaches. Since PET density is higher than water, these materials often sink in the water column, negatively affecting aquatic life. As one obvious adverse outcome, aquatic animals often get entangled or wrapped in PET waste. A more subtle and potentially more harmful effect arises from the accumulation of organic contaminants on PET plastic surfaces. The adsorption and transport of organics on PET plastics are likely to be exacerbated as the plastic weathers in the environment[43,49]. In this dissertation, Rhodamine B (RhB) dye was used to emulate the behavior of common organic contaminants found in the natural environment.

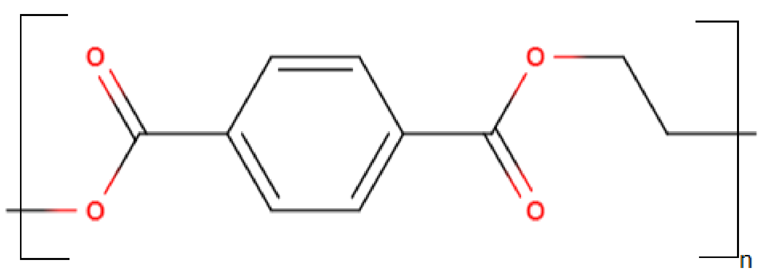

Figure 2.5. Molecular structure of PET.

2.4 Nile Red and its Derivatives

Nile red has a chemical formula of $C_{20}H_{18}N_2O_2$ and is a fluorescent dye with unique properties that make it particularly well suited to single molecule level investigations. The commercial form of NR is depicted in Figure 2.6. In this form, NR is relatively non-polar and uncharged. In order to better explore the different environments (i.e. core and corona) expected to be present in the LLCs studied under this dissertation, other forms of the NR dye were also obtained and employed. These incorporated an alkane tail or charged groups. They comprised a less polar form of NR, designated as NRC_{14} and a more polar form, designated as $NRSO_3^-$. The molecular structures of these dyes are also shown in Figure 2.6**.** These two NR derivatives are unique to this dissertation and were synthesized and characterized by Dr. Takashi Ito and his student Samantha Jenkins. They graciously provided these dyes for use on this project.

The Nile red fluorescence quantum yield and emission spectrum both depend on the polarity of its surrounding environment (i.e., normally the solution in which it is dissolved). In this dissertation, the environment may also comprise any of a variety of nanostructures. The quantum yield of NR has been reported to be 0.38 in methanol (a polar solvent) and 0.48 in n-heptane (a non-polar solvent). Furthermore, its emission maximum shifts from being peaked at 638 nm in methanol to 529 nm in n-heptane[50]. The latter effect, in which a dramatic shift in emission wavelength is observed between polar and non-polar solvents, is known as solvatochromism. This useful attribute allows for the location of the dye to be determined. While most commonly implemented in bulk solutions, this phenomenon is realized at the single molecule level in this dissertation, in complex mixtures such as nanostructured LLCs[50-52]. It can also be used to quantitatively characterize the polarity of its local environment[28].

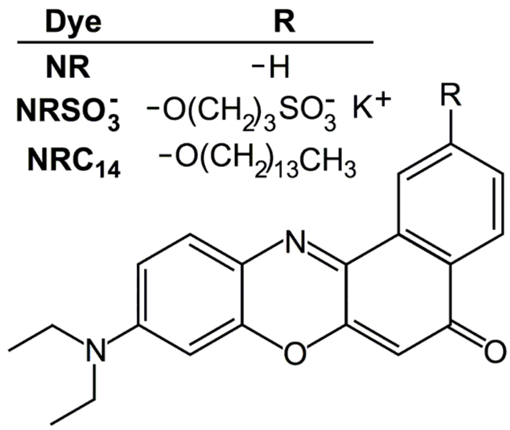

Figure 2.6. Molecular structure of NR, $NRSO_3^-$ and NRC_{14}.

Solvatochromism is a complicated phenomenon which involves various intermolecular forces and depends on dynamic processes of the molecule and the solvent.[53] Its detailed description is beyond the scope of this dissertation. Briefly, solvent molecules can interact with the dipole moment of NR in the ground state that leads to a distribution of oriented solvent molecules around the dye. Upon optical excitation of NR by visible light, a large increase in the NR dipole moment occurs. This occurs upon excitation of the molecule to the first electronically excited state, which is known as a twisted intramolecular charge transfer or TICT state[51,52,54]. The amino group located at the 9-position undergoes rotation around its bond to the ring structure. This rotation allows for strong charge transfer into the ring structure, increasing the dipole moment across the NR molecule. The much greater dipole moment of the TICT excited state then induces a rearrangement of the solvent molecules surrounding the dye. The excited molecule first loses some of its energy and relaxes to the lowest vibrational level of excited state. This occurs on a picosecond timescale. The solvent molecules then reorient around the excited fluorophore on a time scale of 10 to 100 picoseconds. This phenomenon, which is often referred to as solvent reorganization assists in stabilizing and further decreasing the energy of the excited NR molecule. This solvent-equilibrated excited state has a lower energy than the one prepared upon initial excitation. Subsequent emission from this state back to the ground state is therefore red-shifted from that of the initial excited state, giving emission of longer wavelength. Solvents with larger dipole moments more effectively stabilize the more polar excited NR molecule, leading to greater red shifting of its emission. Conversely, in non-polar media, the dipole moments of the solvent molecules are usually too weak to stabilize the large dipole of the excited NR[51,54]. Figure 2.7 provides an overview of the process.

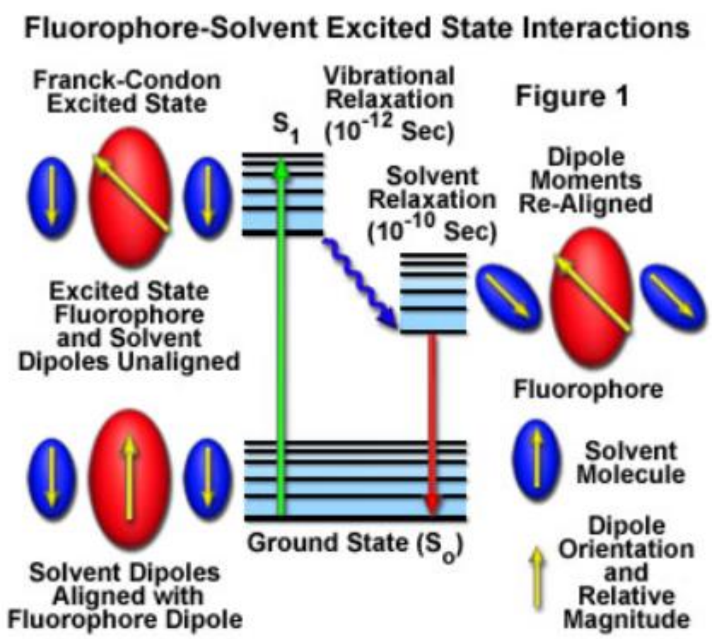

Figure 2.7. Effect of solvent polarity on emission spectra. Reproduced with permission from Ref. 54.

2.5 Rhodamine B

RhB is a water-soluble and highly fluorescent dye characterized by the chemical formula of $C_{28}H_{31}N_2O_3Cl$. Even though it is a carcinogen and genotoxic, it has been used extensively for dyeing textiles and plastics. It has also been added to food products such as sausages and pepper oil to enhance their color[55,56]. RhB yields an emission spectrum peaking at 565 nm in ethanol, and exhibits negligible solvatochromism[31]. RhB has functional groups and heteroatoms similar to many organic pollutants. Figure 2.8 shows the molecular structure of RhB. This dye was utilized in this dissertation to study the diffusion of pollutants over the surface of PET microplastics.

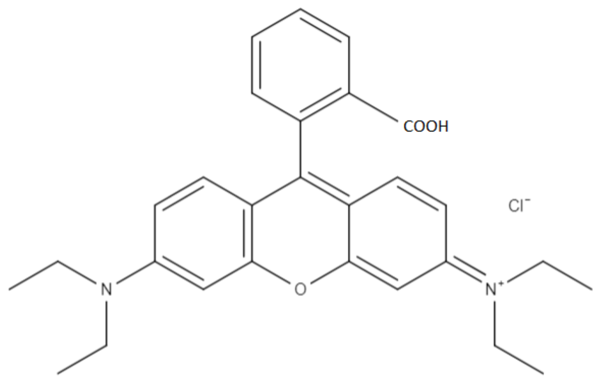

Figure 2.8. Molecular structure of RhB.

Chapter 3 Characterization Methods

3.1 Fluorescence Correlation Spectroscopy

3.1.1 Introduction

Fluorescence correlation spectroscopy, or FCS, is a single-molecule (or near-single molecule) spectroscopic technique renowned for its high resolution spatial and temporal analysis of fluorophore dynamics. FCS was first introduced by Madge, Elson, and Webb in 1972 and was employed to study the diffusion and chemical dynamics of DNA-drug intercalation. This initial work was followed by the work of many other researchers to study particle concentration and the dynamics of molecular diffusion in two and three dimensions. The presentation here will begin with a discussion of the phenomenon of fluorescence itself, followed by an elucidation of the principles underlying FCS.

When a photon of light is absorbed by a molecule, the energy carried by the photon is transferred to the molecule, leading to promotion of the molecule to an excited state (S_1 in Figure 3.1). Within the context of this dissertation, electronic excited states are most important and are produced by absorption of visible photons. Subsequent to excitation, there are several radiative and non-radiative processes that an excited molecule can undergo. However, the most important process in this dissertation involves the return of the excited molecule to its ground electronic state (S_0 in Figure 3.1), releasing its energy. When this energy is released radiatively, this process is called fluorescence and the light emitted by the molecule is known as fluorescent light. Notably, the energy of the photon emitted in this process is often lower than the energy of the photon originally absorbed by the molecule. Hence, the several possible emission transitions shown in Figure 3.1 (downward pointing arrows) are shown in red, while the upward arrow showing the absorption process is depicted in green. Green light has a higher energy than red.

While the energy of the emitted fluorescent photon provides knowledge of the energy difference between the ground and excited electronic states of a molecule, the rate at which photons are emitted is also of considerable importance, and helps determine the emission intensity. It is known that the intensity of the fluorescent light is directly proportional to the analyte concentration at low concentrations (below 1μM)[57]. This principle applies to FCS as well, since in FCS solutions of nanomolar concentrations are being used.

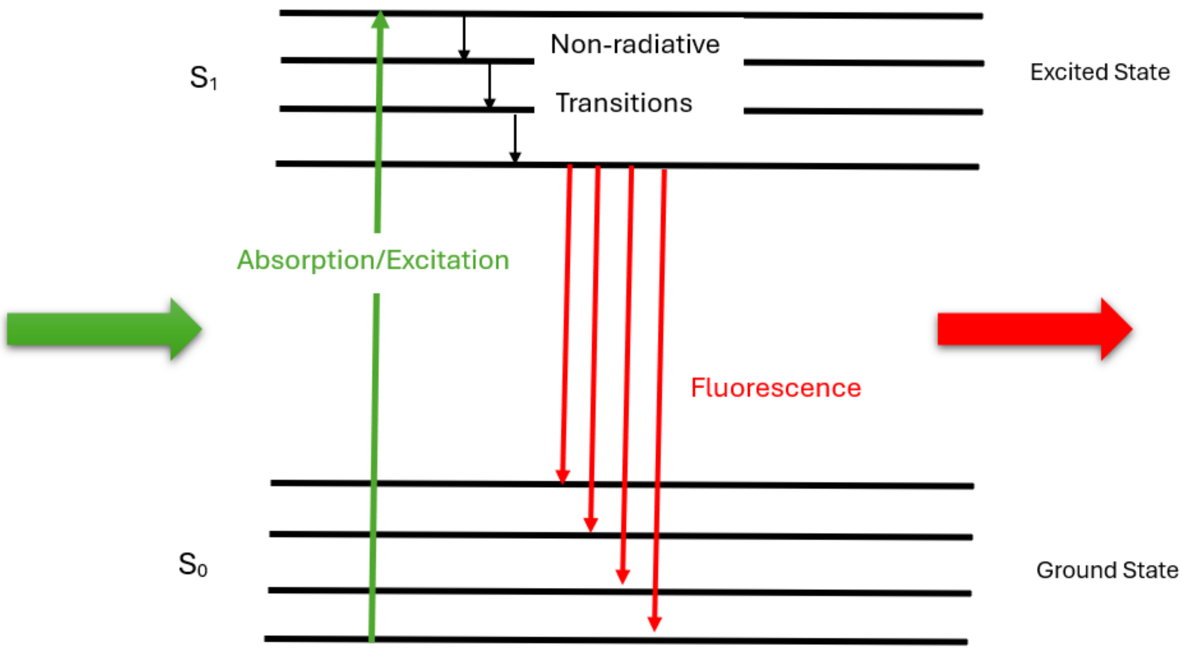

Figure 3.1. Fluorescence process. Here, S_0 and S_1 are ground and excited electronic states respectively. Radiative transitions are shown as green and red vertical arrows while non-radiative transitions are shown as black vertical arrows.

In FCS, it is not the absolute intensity of emission that is important, but rather the fluctuations in fluorescence intensity that matter most. These fluctuations in bulk solutions originate from variation in the number of fluorescent molecules in the detection volume. This variation is mainly caused by Brownian motion of fluorescent molecules in and out of the detection volume. However, there are other phenomena that are beyond the scope of this dissertation and can cause a change in number of fluorescent molecules including triplet blinking and photobleaching.

If there is only one molecule in the detection volume, moving of that molecule causes a great change in fluorescence intensity, but if there are 50 molecules in the detection volume moving one molecule out of it, does not give a significant change against the large average signal. It might not be even noticeable. This causes a poor signal-to-noise ratio[58]. This issue can be better described by an analogy. In a scenario where an individual is in an overcrowded shopping mall with his friend. Due to the presence of other people in the mall, it is almost impossible for him/her to discern whether their friend has entered or left the mall along with the time that it takes for him/her to do that. But in scenarios where the shopping mall has very few people in it, each person's actions can be observed and analyzed separately. Similarly in FCS, in order to investigate spontaneous fluctuations effectively, it is necessary to minimize the number of fluorescent molecules in the detection volume, so each of the fluorophores contribute substantially to the measured signal. To achieve that, the first prerequisite is employing dyes with high quantum yield. Quantum yield is the ratio of the number of emitted photons to the number of absorbed photons. Quantum yield is an indicative of how efficiently a fluorophore converts excitation light into fluorescence[59]. For example, the quantum yield of RhB in ethanol is 0.64[60] and for NR is 0.48 in n-heptane[50]. Secondly, a robust and stable light source is required to excite the dye molecules because the fluctuations caused by variations in excitation light intensity should be avoided. Laser light serves as the stable source that is being employed in FCS. Thirdly, optical devices including an objective lens and pinhole are utilized to confine the detection volume. Fourthly, an ultra-sensitive detector is employed to capture the minute fluctuations in fluorescent signal. Lastly, a dilute solution of the fluorescent dye is needed, so that few molecules will be in the detection region at any instant in time.

For optimal signal-to-noise ratio in FCS, the concentration range typically falls within the nanomolar range[61,62]. Employing small detection volumes, FCS achieves the single molecule level, where the fluorescent intensity is directly proportional to the concentration of the fluorescent solution. For example in this study, as calculated in section 3.1.2, the detection volume (also known as confocal volume) is 0.36 femtolitres. This suggests that to have one fluorescent molecule in this minute volume on average, the solution concentration should be 4.6 nM. However, as mentioned before, the main interest of FCS is not the emission intensity, but rather, the fluctuations of fluorescence intensity.

These fluctuations can be quantified by their duration and rate by autocorrelating the intensity signal. Autocorrelation analysis assesses the self-similarity of the time series signal, furnishing valuable information about the underlying processes (which is diffusion in this dissertation) that cause the fluctuation. To understand autocorrelation functions, one needs to grasp the concept of correlation itself. Correlation tells whether two parameters are unrelated to each other, or, if not, the degree to which they are related. A simple example is the measurement of absorbance for a series of solutions of known concentrations. From the Beer-Lambert law it is known that absorbance is directly related to concentration. When the experiment is performed properly, a linear relationship is found between absorption and concentration. A correlation coefficient (R^2) can be calculated from the result. If $R^2 = 1$, then the change in absorbance is fully explained by a change in the concentration. The data sets are said to be perfectly correlated. If $R^2 = 0$, then the data sets are not correlated. In the context of FCS, the focus is on identifying the correlation between fluorescence intensity at time t, and the same fluorescent time transient data, but at a time τ later. This is called autocorrelation, because it looks at the correlation of a data set with itself[63].

3.1.2 FCS Setup

Figure 3.2 illustrates the experimental set up that was utilized in this dissertation for FCS measurements. The light source that was used was a solid-state laser emitting light at a wavelength of 532 nm. The laser light was first directed through two lenses to ensure it is of appropriate diameter and remains collimated. The appropriate diameter is determined by the diameter of the back aperture of the objective. The beam diameter should closely match the aperture diameter, which is 5 mm. The laser beam is next directed through a series of polarization optics. This series consists of a prism-based polarizer, followed by a half waveplate and then an absorptive sheet polarizer[64]. A polarizer is an optical device that converts unpolarized light into a linearly polarized form. They are often used in pairs. If both polarizers are in a parallel alignment, the maximum intensity will pass through them, but if one is rotated 90 degrees relative to the other, no light can pass through them. The polarizers are used here to set the intensity of the light by insertion of a half waveplate between them[65]. The half waveplate is rotated to adjust the power of laser light sent to the microscope.

Upon entering the microscope, the light is reflected by a dichroic mirror into the back aperture of the objective lens. A dichroic mirror is a mirror with two significantly different reflection properties in different wavelength regions. In fluorescence spectroscopy they can be used to separate emission light from excitation light[66]. In this dissertation the dichroic mirror is chosen as a way to reflect the green excitation light from the laser and transmit red light emitted by the fluorophores. When the light passes through the objective lens and hits the surface of the specimen, it illuminates the sample and excites the fluorescent molecules. The excited molecules emit fluorescence, which is partly collected by objective lens, passes through the dichroic mirror and is directed to a pinhole.

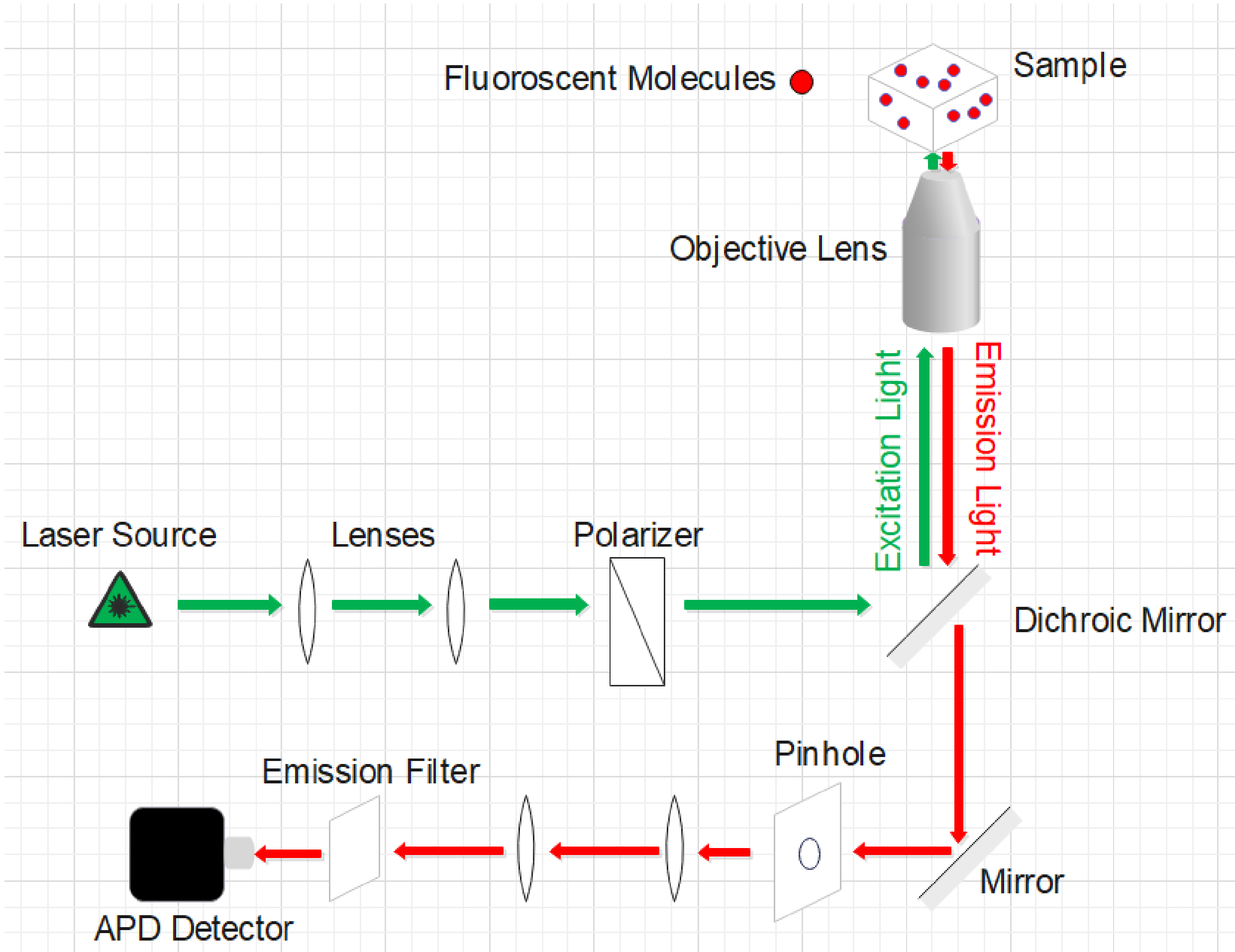

Figure 3.2. FCS setup used in this dissertation.

The pinhole blocks any light that does not originate from the confocal volume, hence providing axial resolution[61]. Then, the fluorescent light passes through two lenses and finally is delivered to the detector. The first lens is positioned one focal length beyond the pinhole, precisely aligned so that the light passes through its center. This arrangement ensures that the light is collimated (i.e. focused at an infinite distance) after passing through this lens. The second lens is positioned at a distance equivalent to its focal length from the detector, so the collimated light gets refocused to the center of the detector. It is imperative to note that a bandpass emission filter is placed right before the detector to filter out any residual laser light and to exclude any stray light coming from other sources at other wavelengths.

The detector utilized in FCS is an avalanche photodiode, abbreviated as APD. The light sensitive element of the APD is very similar to a standard silicon-based photodiode. But it incorporates an 'avalanche region' that is exposed to a high electric field, thus providing an avalanche of electrons for every detected photon. There is a pulse of electrons from the avalanche process and this pulse rapidly terminates, making it nanoseconds in length. This allows phenomena on timescales ranging from nanoseconds to a few seconds to be explored. In this dissertation, the detector counts the number of photons hitting its surface every 40 nanoseconds. This method, counting the number of photons at a specific time interval, is called time-stamping. These pulses are easily counted and processed by computer as elaborated in the following section.

3.1.3 Calculation of Important Parameters

In this this section, important parameters in FCS including axial and lateral resolution, pinhole size, confocal volume and collection efficiency are calculated. All of these parameters are strongly affected by the objective lens and specifically by its numerical aperture or NA. NA defines the light gathering ability of the objective lens and affects lateral and axial dimension of the confocal volume. NA is directly related to the refractive index of the medium (n) and the angle of the cone of light collected between the front lens of the objective and the specimen (α)[67]. This is illustrated in Equation 3.1and Figure 3.3. Immersion oil is employed to improve NA and collection efficiency of the objective lens. The refractive index of air is 1, it is 1.33 for water, and for the immersion oil used in this dissertation, it is 1.518. Two different objective lenses were used in this dissertation. One (Nikon Apo-TIRF) had NA of 1.49 and magnification of 100X and the other (Nikon Plan Fluor) had NA of 1.3 and magnification of 100X.

$$NA = n\sin\alpha \qquad \text{Equation 3.1.}$$

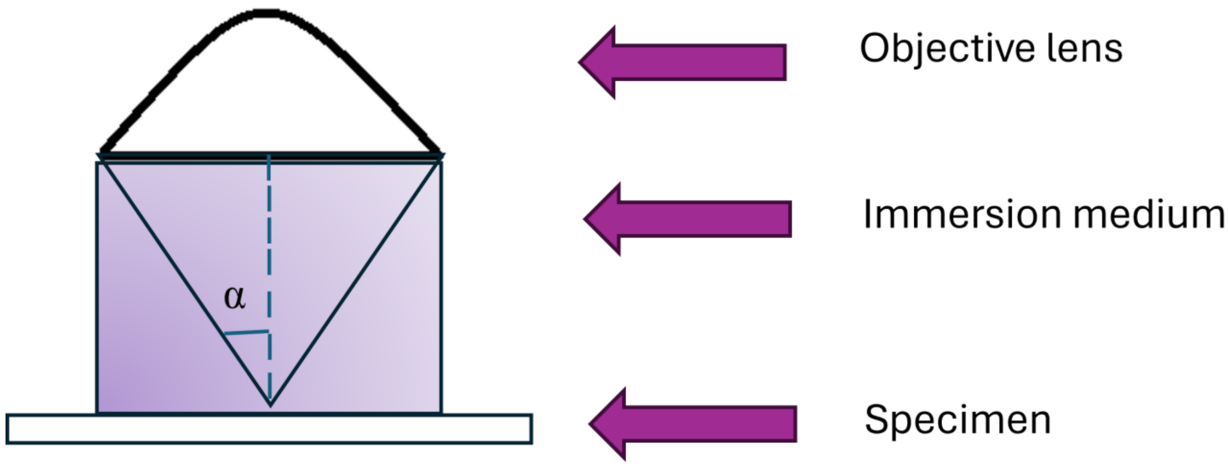

Figure 3.3. Schematic illustration of Numerical aperture.

NA is inversely related to lateral (δ_T) and axial (δ_L) resolution (or dimension) of the confocal volume. This is shown in Equation 3.2 and Equation 3.3, respectively[64]. The lateral and axial dimensions of the confocal volume is illustrated in Figure 3.4. Here, w_{xy} represents the lateral dimension and z_0 represents axial dimension (also known as depth of focus) of the confocal volume.

$$\delta_T = \frac{0.61\lambda}{NA} \qquad \text{Equation 3.2.}$$

$$\delta_L = \sqrt{\left(\frac{0.88\lambda}{n-\sqrt{n^2-NA^2}}\right)^2 + \left(\frac{\sqrt{2}nP}{M_T NA}\right)^2} \qquad \text{Equation 3.3.}$$

In Equation 3.2, λ represents the wavelength of the excitation light. Substituting 532 nm for wavelength of the excitation light and 1.3 for NA gives the radius of the detection volume, which turns out to be 250 nm. In Equation 3.3, M_T is the magnification of the objective lens. The objective provides magnified images ranging from 2X to 100x[68] (100X in this dissertation). Parameter P is the pinhole size. Equation 3.4 is used to determine the pinhole size (P) required[64]:

$$P = 2M_T\delta_T \qquad \text{Equation 3.4.}$$

Replacing 100 as the objective lens magnification and 250 nm as the resolution, the pinhole size turns out to be 50 microns. By substituting λ=532 nm, n=1.518, NA=1.3, P=50 µm and M_T=100, a value of 1000 nm would be obtained for depth of focus, which is z_0 in Figure 3.4.

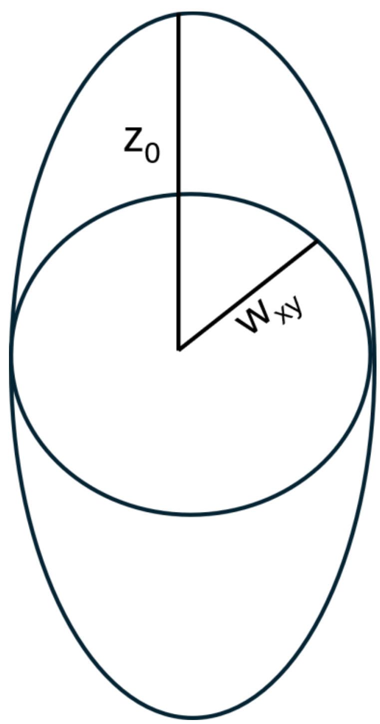

Figure 3.4. Ellipsoidal detection volume.

After calculating the dimensions of the confocal volume, the next step is calculating the confocal volume. The confocal volume refers to the in-focus volume within a specimen that is detected. In FCS, it has an approximately ellipsoidal shape and has a volume in a range of a femtoliter (10^{-15} liters) or less. As can be seen from Equation 3.2, Equation 3.3 and Equation 3.5, the confocal volume is mainly dictated by NA. Pinhole size also affects the confocal volume. There are two ways of calculating confocal volume[69]. First method includes employing Equation 3.5 to calculate the ellipsoidal volume. It should be noted that in Equation 3.5, the effective volume (V_{eff}) has been employed rather than the confocal volume. It has been stated that V_{eff} is $2^{\frac{3}{2}}$ times greater than confocal volume, when the volume is approximated with a 3D Gaussian function[69].

$$V_{eff} = \pi^{\frac{3}{2}} z_0 w_{xy}^2 \qquad \text{Equation 3.5.}$$

To calculate the theoretical value of confocal volume, Equation 3.2, Equation 3.3 and Equation 3.4 should be utilized. Substituting z_0 and w_{xy} values in Equation 3.5 gives a confocal volume of 0.36 femtoliters. This calculations employ the theoretical value of w_{xy}, which is true only under perfect optical conditions. In the experiments described in this dissertation, the value employed has been measured (see below) using standard dyes instead of using the predicted theoretical value.

To find the experimental value of w_{xy}, a solution of a dye with a known diffusion coefficient was utilized each day. Equation 3.6, which is derived from Equation 1.4, was then employed to calculate w_{xy}. In this equation, D is the diffusion coefficient and τ denotes the diffusion time. Section 3.1.4 explains how to obtain the diffusion time (τ) from the FCS data. The experimental values of w_{xy} vary from 260 nm to 300 nm in this dissertation.

$$D = \frac{w^2}{4\tau} \qquad \text{Equation 3.6.}$$

The second method employs Equation 3.7 to compute the effective volume. In this equation, G_0 represents the autocorrelation amplitude. The value of G_0, is inversely related to the average number of molecules in the confocal detection volume, <n>, in which $G_0 = 1/\langle n \rangle$[69]. In using Equation 3.7, N_A is Avogadro's number and c denotes the molar concentration of the sample. For a 5 nM solution, with G_0 of 1, V_{eff} is calculated to be 0.33 femtoliters.

$$V_{eff} = \frac{1}{G_0 N_A c} \qquad \text{Equation 3.7.}$$

Finally, to calculate collection efficiency, Equation 3.8 is used. The NA value as well as the refractive index of medium affect the collection efficiency of the objective lens. Theoretically, the maximum collection efficiency is 0.5 according to Equation 3.8. By substituting 1.518 for refractive index and 1.3 for NA, the collection efficiency of the FCS was computed to be 0.24 or 24%.

$$F = \frac{1}{2}(1 - \sqrt{1 - \frac{NA^2}{n^2}}) \qquad \text{Equation 3.8.}$$

3.1.4 Data Analysis

Software written by others in the research group was employed to analyze the data obtained. This software takes the photon time-stamped results and converts it into a graph called a time transient, which is photon counts as a function of time. Figure 3.5 (a) and (b) depicts time transient graphs for the case of free diffusion of NR in ethanol and confined NR diffusion within ethanol-filled 10 nm pores of an AAO membrane. The contrast between the fluctuations in these two graphs provides valuable insight into the differences in diffusion rates and mechanisms in these two cases. However, while informative, these graphs alone do not offer quantitative information about molecular dynamics within the confocal volume. The fast fluctuations revealed in Figure 3.5 (a) are attributed to fast passage of freely diffusing molecules through the confocal volume. In Figure 3.5 (b) the fluctuations are much more apparent because they are much slower and are separated by relatively long periods of background counts. These slower fluctuations are attributed to a dramatic slowing of dye motion through the confocal volume when confined within the nanometer sized AAO pores. This is uniquely different from what happens in bulk solution and understanding the origins of the slow motions is the purpose of the work reported in this dissertation. While these plots allow qualitative interpretations of the different rates and mechanisms of diffusion, quantitative information can only be obtained through further mathematical analysis. Here, this analysis involves calculating their autocorrelation functions and fitting these to an appropriate model for the expected diffusion mechanism.

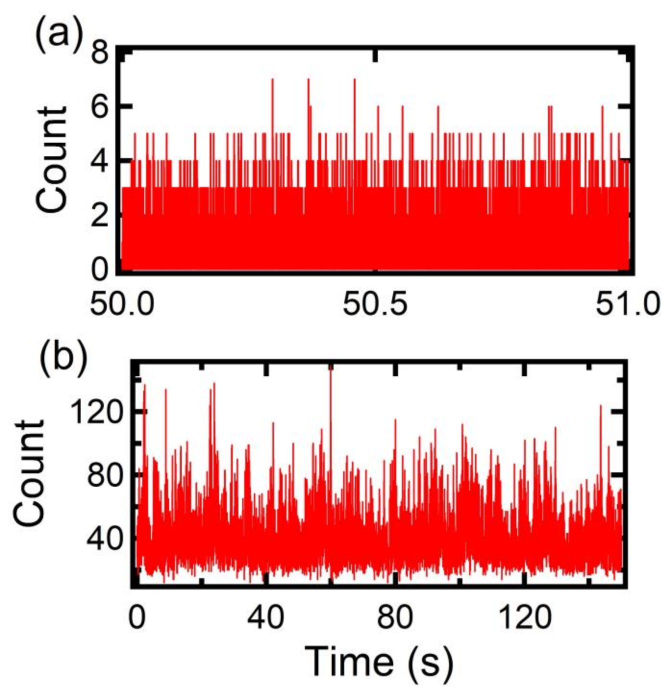

Figure 3.5. Time transient of 20 nM NR in (a) bulk ethanol (100 μs bin time) and (b) ethanol in 10 nm pores (10 ms bin time).

A better understanding of autocorrelation data may be obtained by considering the following example. Table 3.1 gives the fluorescence intensity in 5 ms time intervals from data collected in our lab for diffusion of NR in ethanol-filled 10 nm pores.

If one plots the intensity along the y axis as a function of the same intensity data along the x axis, the graph would be perfectly linear with correlation coefficient of 1. Doing the same thing but with a 5 ms time delay (i.e. the first point is (18,12)) yields an R^2 of 0.52. Subsequently, changing the time interval to 40 ms decreases R^2 to 0.26 and by using 640 ms time interval it would further drop to 0.009. This is shown in Figure 3.6.

Table 3.1. Fluorescence intensity in 5 ms time intervals (first 10 data points)

Intensity	Time (s)
18	0
12	0.005
16	0.01
32	0.015
26	0.02
21	0.025
13	0.03
15	0.035
8	0.04
15	0.045

A graph of the correlation coefficient as a function of the time delay (τ), is what is referred to as the autocorrelation function in FCS. The time required for the correlation coefficient to reach zero depends on how fast the fluorophores move (diffuse) in and out of the confocal volume. The faster the molecules move, the faster the autocorrelation function decays. In the above example, as shown in Figure 3.7 the correlation coefficient gets very close to zero (0.009) after 640 ms

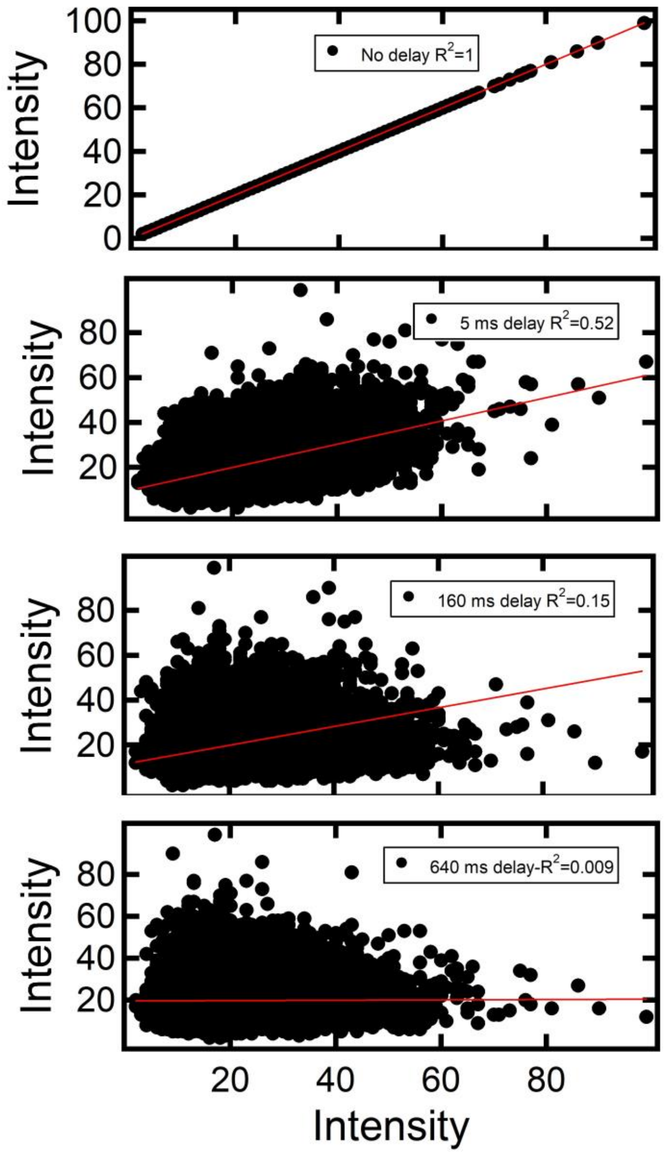

Figure 3.6. Intensity vs intensity with 0, 5, 160 and 640 ms time delays. The red line shows fitting of the data points to a line.

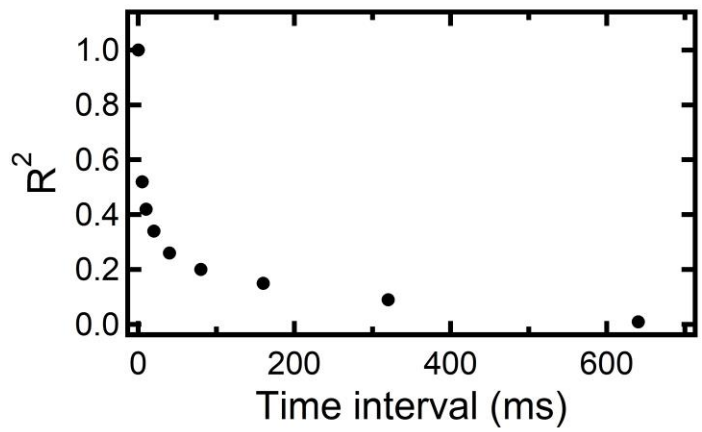

Figure 3.7. Correlation coefficient vs time. In this example there is almost no correlation between intensity data after 640 ms.

Calculation of the autocorrelation function from a time transient is rather simple. Equation 3.9 is employed for this purpose.

$$G(\tau) = \frac{<F(t)F(t+\tau)>_t}{<F(t)>_t^2} - 1 \qquad \text{Equation 3.9.}$$

here $G(\tau)$ represents the autocorrelation function, the brackets given by $< >_t$ indicate that the time average is employed, $F(t)$ is fluorescence intensity at time t and $F(t+\tau)$ is the fluorescence intensity at time $t+\tau$. Equation 3.9 can also be written in terms of fluctuations in fluorescence intensity as $G(\tau) = \frac{<\delta F(t)\delta F(t+\tau)>_t}{<F(t)>_t^2}$ where $\delta F(t) = F(t) - < F >_t$.

In this research, calculation of the autocorrelation function is done using C++ code written in-house, because the process can be very slow when run by interpreted code, rather than compiled code. As noted above, obtaining quantitative data from the autocorrelation function requires fitting it to selected models to identify the one the gives the best fit. Here, the best fit is determined by the model that gives the smallest X^2 (i.e., the smallest sum of the relative mean squared residuals). Depending on the dimensions of diffusion, the number of active diffusion mechanisms, and the type of diffusion (i.e., free or anomalous), there are multiple models available in the literature[28,31,49]. Equation 3.10 gives an example of a two-dimensional one-component diffusion model that can be used to obtain the diffusion time. Note that a one-component model is used when a single diffusion mechanism governs the motion of the dye.

$$G(\tau) = A + \frac{B}{\left(1+\frac{\tau}{\tau_D}\right)} \qquad \text{Equation 3.10.}$$

Here, τ_D denotes the diffusion time or the decay time of the autocorrelation function, A is an offset, which is close to zero, and B is the amplitude of the autocorrelation function. This equation shows that when $G(\tau)$ reaches $\frac{B}{2}$, $\tau = \tau_D$. While this assignment works for 2D diffusion, 1D and 3D diffusion give more complex dependences in which τ_D is not so easily identified from $G(\tau)$, and fitting the data is the simplest means to extract its value.

3.1.5 Variable Area FCS

In certain instances, adjusting the size of the confocal volume is essential to thoroughly elucidate the diffusion mechanism. For example, changing the observation area is essential to perform what are called FCS diffusion law measurements. The FCS diffusion law is rooted in Equation 3.6. As is evident in Equation 3.6, a graph of diffusion time (τ) versus observation area (w^2) should give a Y-intercept of zero. However, this is only expected in the case of free Fickian diffusion. In situations where diffusion is constrained, a positive intercept is observed, consistent with anomalous sub-diffusion. In contrast, anomalous super-diffusion results in a negative intercept[28,70-72].

Various methods exist to change the observation area. In previous work, a common method of doing this involved simultaneously changing the size of the incident laser spot using a variable optical telescope in the path before the objective lens while simultaneously varying the detection volume by changing the pinhole size[73,74]. This method was deemed overly complicated. To simplify the experiments under this dissertation, a broad illumination spot of fixed size was instead employed while systematically changing pinhole size. Changes in the pinhole size were implemented here by employing a pinhole wheel. The pinhole wheel that was employed contains apertures ranging from 25 microns to 2000 microns. The systematic alteration of the detection area gives rise to a new sub-class of FCS called variable area FCS or va-FCS.

3.2 Fluorescence Spectroscopy

Fluorescence spectroscopy stands as an analytical method that is employed extensively due to its high sensitivity and its non-destructive nature. Its sensitivity surpasses that of techniques relying on absorption by one to three orders of magnitude[75], primarily due to the fact that fluorescence spectroscopy is a dark background method. In fluorescence spectroscopy the light emitted from the molecules is measured against a dark background, hence a minute change in the emitted light intensity is detectable. While in methods like absorption spectroscopy a reduction in light intensity is being measured.

Figure 3.8 illustrates a simplified setup of a fluorescence spectrophotometer, or fluorometer for short. Radiation sources in fluorescence spectroscopy include mercury arc lamps, xenon arc lamps, metal halide lamps and LEDs[76]. A Xenon arc lamp was used in this dissertation. These sources produce a broad range of wavelengths for use in fluorescence excitation. The light passes through a monochromator that selects excitation light of the desired wavelength. Monochromators include a diffraction grating to disperse light, entrance and exit slits and mirrors so that the desired wavelength can be selected. Various wavelengths can be selected to exit through the slit by rotating the grating. The narrow band of wavelengths selected is then directed onto the sample. The molecules in the sample absorb some of the excitation light and become excited. Following the processes described in Figure 3.1, the molecules later emit fluorescence. The emitted fluorescence is then collected and directed through another monochromator, which allows the emission to be recorded as a function of wavelength. Finally, Photomultiplier tubes (PMTs) are commonly employed as detectors in fluorescence spectroscopy, as is the case in the instrument employed here[77].

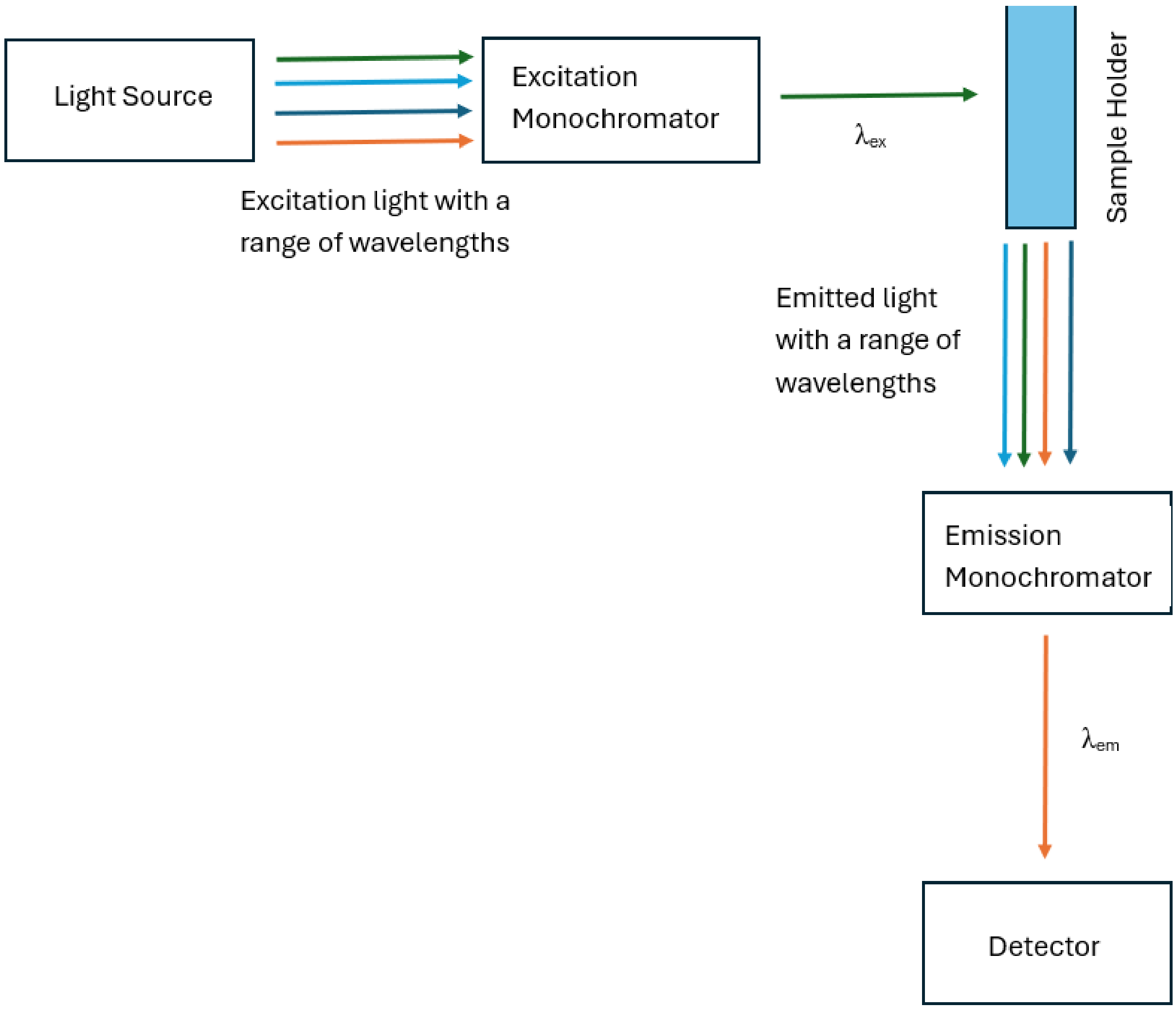

Figure 3.8. Fluorescence spectroscopy setup.

In this dissertation, the most important data obtained from fluorescence spectroscopy were the excitation and emission wavelengths of the dyes, specifically NR. Because, as discussed in section 2.4, NR is a solvatochromic dye, meaning that its peak emission wavelength depends on the polarity of the solvent. In this dissertation, NR is used in a variety of solutions and gels of different polarities. This information is needed to select the appropriate emission filter for the FCS measurements.

3.3 Raman Spectroscopy

The term "Raman" is used in honor of the person that first discovered this form of spectroscopy in 1928, an Indian physicist named C.V. Raman. He later won the Nobel prize in physics in 1930 for this discovery. Raman scattering refers to the inelastic scattering of photons that happens when incident light interacts with molecules in a sample[78]. Inelastic scattering is a type of scattering in which the energy of the scattered light is different than the energy of the light incident. Figure 3.9 depicts the Raman scattering process schematically. Upon interaction with the sample, incident light creates a polarization of the molecular electron cloud that is commonly called a virtual state. Virtual states have energy that is different from any of the electronic states of the molecule. Three possible scenarios can unfold following creation of the virtual state: 1. The polarization of the molecule can relax back to the original state, launching a new photon of the same energy as the incident photon in a process called Rayleigh scattering (green downward arrow). Since the scattered light has the same frequency as the incident light, this constitutes an elastic process. Although by far the predominant process (occurring 99.999% of the time), elastic scattering does not provide significant information about the sample. 2. The electronic polarization relaxes to a state that is higher in energy than the original state. The original state in this case is usually the ground vibrational state of the ground electronic state, while the final state is a vibrationally excited state of the electronic ground state. The scattered photon in this case carries less energy than the incident photon. This inelastic process is called Stokes Raman scattering. 3.

The electronic polarization relaxes to a state that is lower in energy than the original state of the molecule. In this case, the original state may be a vibrationally excited state of the electronic ground state and the final state the vibrational ground state of the electronic ground state. The scattered photon gains energy from the molecule in this inelastic process. This process is called anti-Stokes Raman scattering.

Although Stokes and anti-Stokes Raman scattering collectively comprise a mere 0.001% of the scattered light, they furnish invaluable insights into molecular bonds and structure of the molecule under study. With advancements in modern optics and detectors, this minute portion of scattered light can be accurately detected and analyzed, allowing for detailed characterization of samples[79].

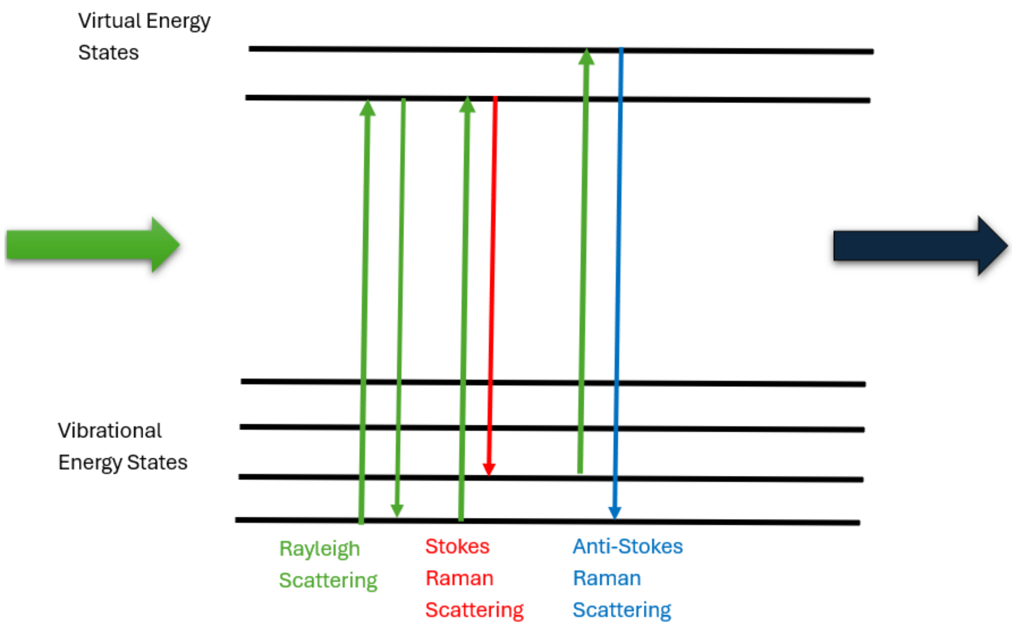

Figure 3.9. Rayleigh and Raman scattering.

The Raman spectroscopy setup utilized in this research closely resembled the FCS setup, and in fact employed the same optical microscope and many of the same optical components. The one main exception was the use of a 532 nm holographic notch filter (with 532 nm incident laser light) in place of the usual bandpass filter. The notch filter was used to eliminate Rayleigh scattering. Another important difference was the use of an electron multiplying charged-coupled device detector (EM-CCD) in place of the APD used in FCS. As an array detector, the EM-CCD allowed for the recording of Raman spectra across a broad range of wavelengths. Finally, since the Raman measurements were employed on the solutions in the absence of dyes, photobleaching was not a concern. Hence, the laser power that was used was much higher (800 times) than FCS.

The main reason for using confocal, and not ordinary, Raman spectroscopy is that we are interested in measuring the solution composition inside 10 nm and 20 nm pores and then comparing it with bulk solution composition. The confocal setup is employed to achieve small detection volumes (femtoliter), appropriate to study solution composition in nanopores. Confocal Raman spectroscopy has been used previously to study localization of nanomaterials in the cells[80], uptake of nanoparticles into culture cells[81], single living cells and chromosomes[82] and protein distribution inside biological cells[83].

3.4 Small Angle X-ray Scattering (SAXS)

SAXS is a powerful method for characterizing the structure of soft materials including proteins, liquid crystals, colloids, polymers and lipids[28,84-86]. In SAXS, a collimated X-ray beam is directed onto the sample where it interacts with the local nanostructures. The X-ray beam is scattered from organized structures in the sample in much the same way as light is scattered from a diffraction grating. This process is known as Bragg scattering[87], and the angle and direction into which the X-rays are scattered provide information on the organization, orientation, and the spacing of materials nanostructures. To acquire X-ray scattering data, the intensity of the scattered X-ray beam is recorded as function of scattering angle by an X-ray detector.

Figure 3.10 shows a simplified setup for SAXS experiments. Here, 2θ is the scattering angle between the scattered and transmitted X-ray beam. Equation 3.11 provides the mathematical relationship between the scattering angle, the X-ray wavelength, λ, and the scattering wavenumber, q.

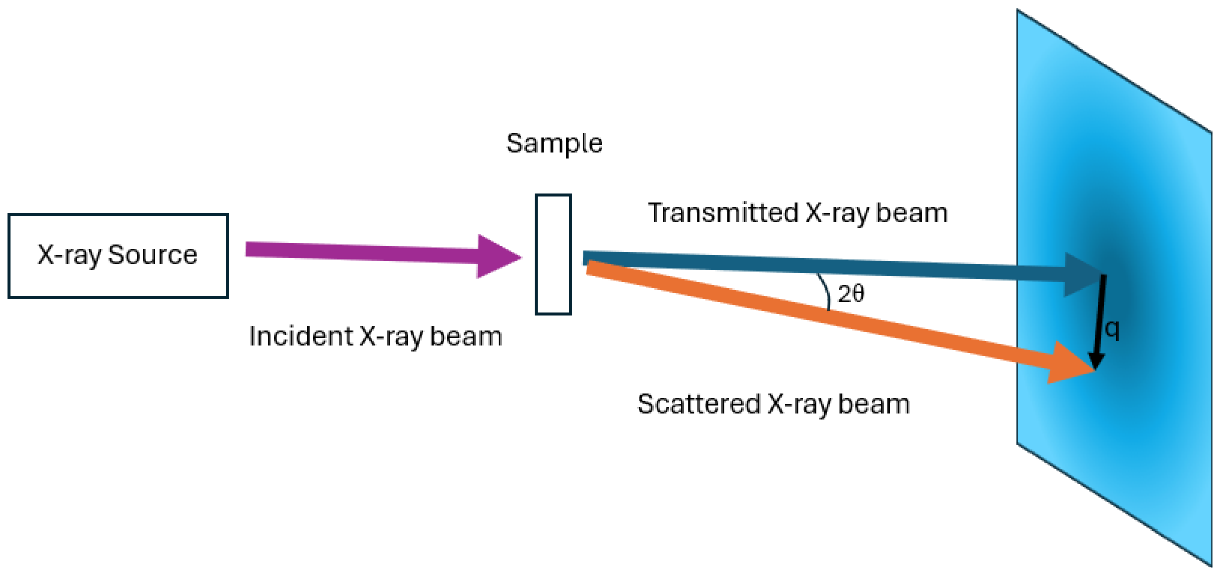

Figure 3.10. SAXS setup.

$$q=\frac{2\pi}{\lambda}(\hat{s}_0-\hat{s}_1)=\frac{4\pi\sin\theta}{\lambda} \qquad \text{Equation 3.11.}$$

Here, $\hat{s}_0$ and $\hat{s}_1$ denote the scattering vectors associated with the incident and scattered X-ray beams, respectively.

The desired information from SAXS experiments is frequently the spacing between materials nanostructures. This information can be obtained by applying Braggs law (Equation 3.12) to Equation 3.11, yielding Equation 3.13.

$$n\lambda = 2d\sin\theta \qquad \text{Equation 3.12.}$$

$$q = \frac{2\pi}{d} \qquad \text{Equation 3.13.}$$

In Equation 3.13, d is the desired distance between the scattering planes (i.e. the nanostructures) comprising the sample.

In this dissertation, SAXS was employed to study the organized nanostructures found within lyotropic liquid crystals (LLCs). In this case, 2D SAXS scattering was employed to not only determine the d-spacing for the LLC nanostructures, but also the orientations of these nanostructures via the scattering anisotropy (i.e. the direction in which the X-rays were scattered). Figure 3.11 shows the schematic of hexagonal LLCs studied with SAXS. The 2D scattering image therefore aids in discerning the ordering and directional alignment of the micelles within the LLC (Figure 3.12), while an intensity versus q graph provides insights into the nanostructure spacing in the materials. The latter also provides information on the exact organization of the micelles. For instance, a material exhibiting hexagonal organization of micelles will give scattering peaks at relative positions of $1{:}\sqrt{3}{:}\sqrt{4}{:}\sqrt{7}$ [88].

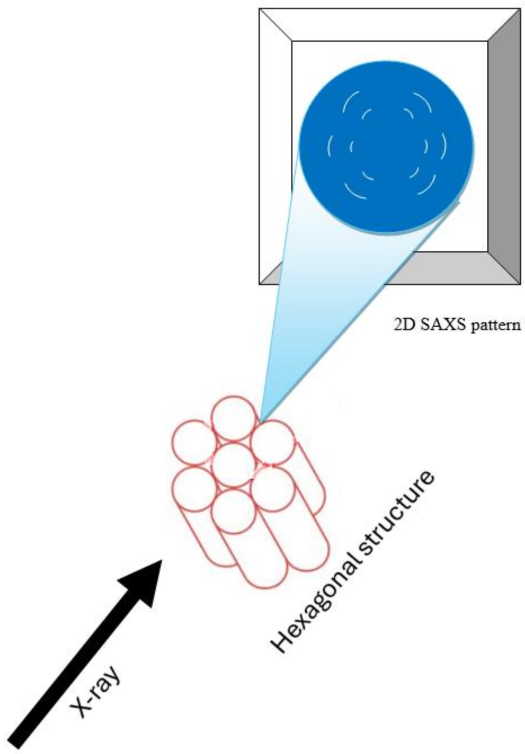

Figure 3.11. Schematic of hexagonal LLCs studied with SAXS.

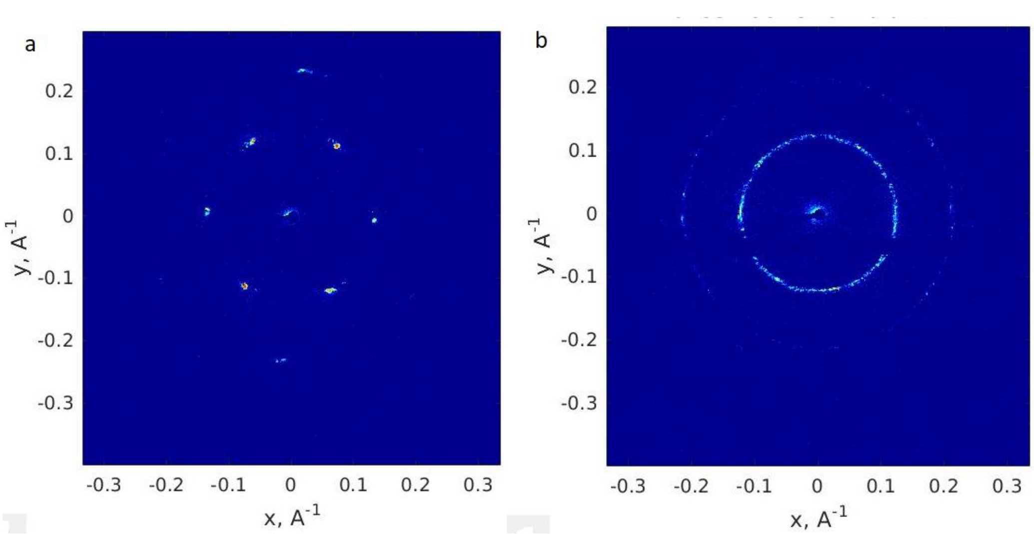

Figure 3.12. 2D SAXS image of a. ordered and b. disordered lyotropic liquid crystal.

3.5 Sessile Drop Water Contact Angle Measurement

Sessile drop water contact angle measurements offer a straightforward and accessible means to measure the wettability of a surface. The contact angle provides valuable information about the degree of hydrophilicity/hydrophobicity of the surface. The procedure involves depositing a minute volume of water (typically 1-2 µL) onto a flat surface of the sample. After taking an image of the sample, the angle between the surface and the droplet is measured (Figure 3.13). The contact angle is related to surface energy through Young-Dupre equation[89] (Equation 3.14).

$$\gamma_{sv} - \gamma_{sl} = \gamma_{lv} \cos\theta \qquad \text{Equation 3.14.}$$

Here, γ_{sv}, γ_{sl} and γ_{lv} are energy per unit area of solid-vapor, solid-liquid and liquid-vapor interfaces, respectively. The θ parameter denotes the contact angle. If this angle is greater than 90 degrees the surface is categorized as hydrophobic, otherwise it is called hydrophilic[90]. When $\theta > 90°$, the term $\cos\theta$ would be negative, which makes γ_{sl} a larger value, compared to $\theta < 90°$, where the term $\cos\theta$ would be positive. A large solid-liquid energy is unfavorable. This means that the solid tends to minimize the surface that is in contact with the liquid. This is a hydrophobic surface, where the area of the solid in contact with the liquid is minimized and the contact angle is high.

In this dissertation, contact angle measurements were employed to investigate the effect of surface oxidation on wettability of PET microplastics.

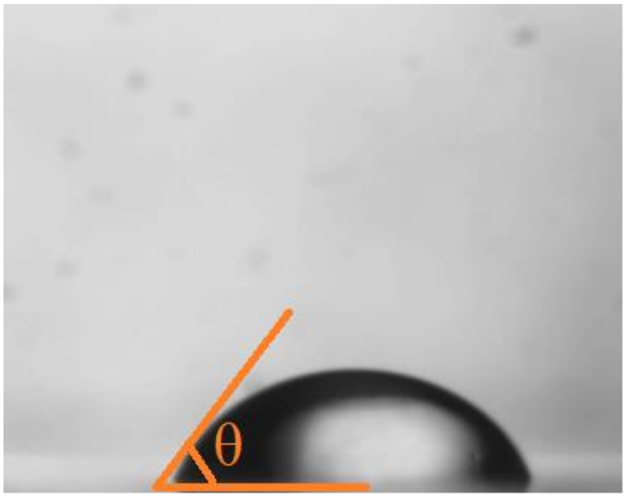

Figure 3.13. Water droplet on microplastic surface, θ is the contact angle.

3.6 Atomic Force Microscopy

Atomic force microscopy (AFM) is a powerful technique utilized for visualizing and quantifying surface topography and roughness with exceptional resolution and precision. Since its invention in 1980s it has found extensive applications in diverse fields including chemistry, physics, biology, materials science, nanotechnology, astronomy and medicine. Unlike more traditional microscopes, AFM does not rely on light or electrons to form an image. Instead, it employs a sharp probe to physically interact with the sample, providing detailed information about its surface characteristics.

There are three distinct modes of AFM based on the extent of contact that occurs between the tip of the probe and the sample surface. These are contact mode, non-contact mode, and intermittent contact or tapping mode[91]. Depending on the operational mode, the tip of the probe either makes direct contact with the sample surface (contact mode) or approaches very closely (0.2 to 10 nm) to the surface (non-contact mode). The primary forces measured in AFM are often attributed to Van der Waals and electrostatic interactions. The probe experiences repulsive and attractive forces in contact and non-contact mode, respectively. In tapping mode, the probe experiences both forces depending on the distance between them[92].

In each mode, the AFM probe is attached to a flexible cantilever serving as a spring that senses the forces between the tip and sample. Images of a sample surface are acquired by moving the tip across the sample surface. As this motion necessarily involves movement of the tip with sub-nanometer precision, it is most commonly done using piezoelectric scanners. These scanners are also used to move the tip towards or away from the sample surface to maintain a constant force between the tip and sample in the constant force imaging mode. Changes in the forces between the tip and sample are sensed by sensing the motions of the cantilever. Cantilever motions are in turn sensed optically. For this purpose, a laser beam is reflected from the back of the cantilever and directed onto a position-sensitive photodetector. As the probe moves across the surface, the light incident on the detector gives a means to measure the bending of the cantilever that supports the AFM probe. These measured deflections give a means to sense changes in force between the probe and the sample, and thus to adjust the probe height above the sample to maintain a constant force in the constant force mode. By recording the height of the AFM probe, an image of the surface topography is obtained. In constant height mode, the optical signal resulting from cantilever deflection can be directly recorded to give an image of the surface based on the strength of the tip-sample interactions (see Figure 3.14).

In the present dissertation, intermittent contact mode was employed to acquire surface topographic images of fresh and artificially aged PET microplastics and to investigate the effect of surface oxidation on its roughness.

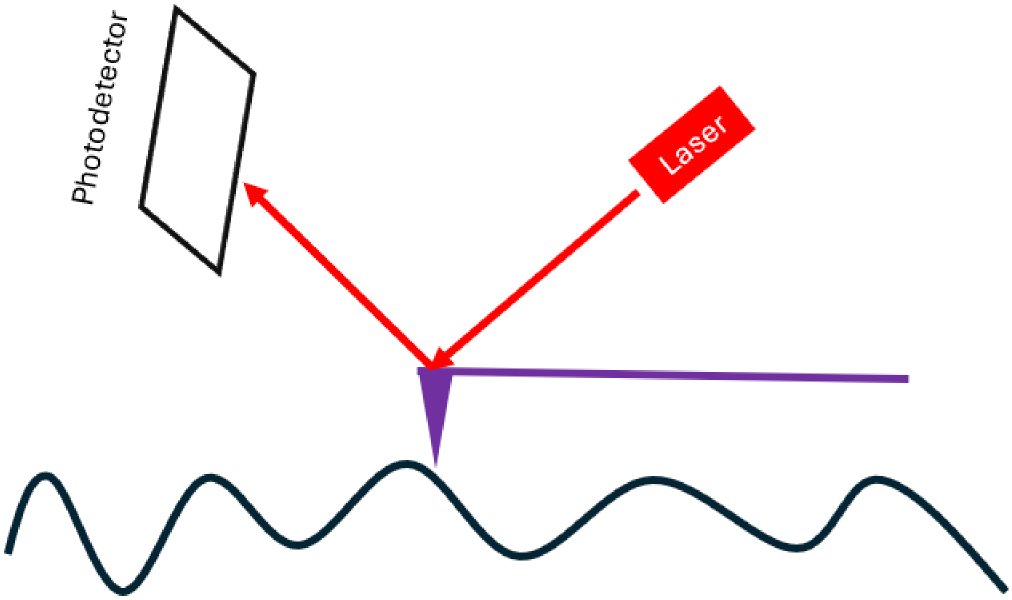

Figure 3.14. Schematic of AFM setup.

Chapter 4 Diffusion of Hydrophilic to Hydrophobic Forms of Nile Red in Aqueous $C_{12}EO_{10}$ Gels by Variable Area Fluorescence Correlation Spectroscopy

Adapted with permission from: Shafiee, O.; Jenkins, S. G.; Ito, T.; Higgins, D. A. Diffusion of hydrophilic to hydrophobic forms of Nile red in aqueous $C_{12}EO_{10}$ gels by variable area fluorescence correlation spectroscopy. *Physical Chemistry Chemical Physics* **2023**, *25*, 2853-2861, Copyright 2023 Royal Society of Chemistry.(https://doi.org/10.1039/D2CP05578C)

4.1 Introduction

Nanostructured lyotropic liquid crystals derived from nonionic surfactants find myriad potential applications in controlled drug release[93-95], chemical separations[96,97], and in the templated synthesis of nanomaterials[98,99]. The concentration-dependent structures and organization of many such materials have been explored by X-ray[100,101] and neutron scattering[102,103], nuclear magnetic resonance spectroscopy[102], polarized light microscopy[39,101], and cryogenic transmission electron microscopy[104,105]. However, the optimization of LLCs for many of their applications also requires knowledge of the mass transport dynamics exhibited by solutes confined within them. Far fewer studies have explored these phenomena, and much less is known about how organized, crowded nonionic LLC nanostructures either facilitate or limit solute diffusion. Relevant prior work in this area includes radio tracer[106], and Taylor Dispersion[107,108] studies of diffusion by both surfactants and probes in relatively dilute micellar solutions. Interestingly, pulsed-field gradient NMR studies have revealed anisotropic diffusion caused by aligned LLC nanostructures[109,110] in more concentrated systems.

Optical microscopic methods offer valuable alternative routes to exploring the rates and mechanisms of solute mass transport in LLCs. Fluorescence correlation spectroscopy (FCS)[111-113] represents a particularly useful method in this regard, having been employed previously to study diffusion in a variety of biologically- and technologically-relevant materials[114-117]. In FCS, a confocal microscope is employed to illuminate a diffraction-limited region of the sample. The sample is doped at low (*i.e.*, pM – nM) concentrations with a luminescent dye so that only a few molecules are present within the detection volume at any instant in time. These molecules diffuse in and out of the detection region, producing fluorescence fluctuations that are easily recorded. Subsequent autocorrelation of the fluorescence time transients obtained allows for determination of the molecular concentration, the average residence time of the molecules in the confocal volume, and their diffusion coefficient, D.

FCS experiments are commonly performed using a detection region of fixed size. Unfortunately, this restriction may prevent full characterization of the diffusion mechanism by masking any variations that occur on sub-micron length scales. To overcome this limitation, variable area FCS (va-FCS) measurements are now regularly employed[71,73,74]. In its most common form, va-FCS employs confocal methods in which the illumination and detection regions are simultaneously varied in size. For Fickian diffusion, the measured diffusion time, τ_D, is expected to be linearly dependent on detection area (or volume), yielding a zero intercept when the data are extrapolated to zero area. The observation of an affine dependence of τ_D (*i.e.*, a non-zero intercept) provides evidence of deviations from Fickian behavior due to confinement by the material structure[71-73]. However, such deviations are difficult to detect in samples with features much smaller than the diffraction limit, unless they cause significant slowing of probe molecule diffusion[70].

In this study, we employ va-FCS to explore the rates and mechanisms of solute diffusion for a series of organic dyes dissolved within polyoxyethylene alkyl ether derived LLC mesophases. The dyes are all derivatives of Nile red (NR)[118,119] and are sufficiently fluorescent to be detected at the single molecule level. The commercial form of NR is employed along with a more hydrophilic, anionic form incorporating a sulfonate group ($NRSO_3^-$) and a hydrophobic form incorporating a fourteen-carbon-long alkane tail (NRC_{14}). Decaethylene glycol monododecyl ether ($C_{12}EO_{10}$) was employed to form the LLCs[39,120]. When mixed with water at appropriate concentrations, this commercially available surfactant readily forms highly viscous, optically transparent gels comprising a hexagonal phase of cylindrical micelles. These gels may incorporate micelles a few hundred nanometers in length[104,105] or other heterogeneities that limit solute diffusion on length scales accessible by diffraction-limited va-FCS methods. Small angle X-ray scattering data are used to verify the formation of the hexagonal mesophase and to quantitatively determine micelle spacing across a range of surfactant concentrations. The results obtained from va-FCS studies are used to quantitatively determine the diffusion coefficient of each dye, to explore its mass transport mechanism, and to obtain possible evidence that its diffusion is confined by the material nanostructure.

4.2 Experimental

4.2.1 Materials

Decaethylene glycol monododecyl ether (see Figure 2.3b) was obtained from Sigma-Aldrich and was used as received. LLC gels were prepared as aqueous solutions and were obtained by first weighing an appropriate amount of $C_{12}EO_{10}$ into a disposable glass vial. The necessary amount of pure water (Barnstead B-pure, 18 MΩ cm) was then added to bring the total mass of the gel to 2 g. This was followed by the addition of a 50 μL aliquot of one of the three dyes (see below) as a 0.8 μM ethanol solution, bringing the final dye concentration in each gel to ∼20 nM. A series of gels having compositions ranging from 55 : 45 wt% up to 70 : 30 wt% were employed in optical experiments. After addition of the dye, the vials were tightly sealed, and the gels thoroughly mixed by repeated inversion and centrifugation. Mixing was facilitated by heating the gels to 60–70 °C to reduce their viscosity. As a final step, they were centrifuged for ∼1 h to obtain optically clear gels that were free of visible air bubbles. The gels were stored for a minimum of one day in the dark prior to use.

Nile red was obtained from Sigma-Aldrich and was used as received. Hydrophilic and hydrophobic derivatives of NR were obtained by modifying a hydroxylated form of Nile red previously synthesized by Dr. Takashi Ito with help from Duy Hua [121]. The structures of all three dyes are shown in Figure 2.6. The hydrophobic form of the dye incorporated a fourteen-carbon-long *n*-alkyl ether tail (NRC_{14}) while the hydrophilic form was obtained as a sulfonated *n*-propyl ether derivative ($NRSO_3^-$).

4.2.1.1 Synthesis of 9-Diethylamino-2-sulfonatopropyl-5H-benzo[a]phenoxazin-5-one, Potassium Salt ($NRSO_3^-$).

The synthesis of $NRSO_3^-$ was performed by Dr. Takashi Ito with help from Duy Hua. The starting material (9-diethylamino-2-hydroxy-5H-benzo[a]phenoxazin-5-one, NROH) used in this synthesis was obtained as described previously[121]. NROH was subsequently modified as shown in Figure 4.1. following procedures described in the literature[122,123]. NROH (FW 354.79; 22.8 mg (0.064 mmol)) and sodium 3-bromopropanesulfonate (Alfa Aesar, FW: 225.05; 0.596 mmol) were dissolved in 2 mL anhydrous methanol, and then K_2CO_3 (Fisher, FW: 138.21; 155.59 mg (1.126 mmol)) was added. Afterwards, the mixture was refluxed under Ar while stirring for 2 days. The mixture was neutralized with an aqueous solution of acetic acid (Fisher) to achieve a 2:1 methanol:

water solution. The final product was purified by reversed-phase silica gel column chromatography (C18-fully-endcapped reversed phase silica gel, Aldrich 60757; eluent: methanol: water = 2:1) to obtain a purple solid (FW: 494.23; 11.2 mg (0.023 mmol), Yield: 36%).

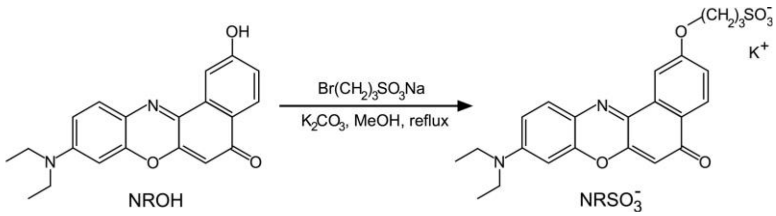

Figure 4.1. Synthesis of $NRSO_3^-$.

4.2.1.2 Synthesis of 9-Diethylamino-2-tetradecyloxy-5H-benzo[a]phenoxazin-5-one (NRC_{14})

The synthesis of NRC_{14} was performed by Dr. Takashi Ito with help from Duy Hua. Here, NROH was subsequently modified as shown in Figure 4.2, following procedures described in the literature[122,123]. NROH (FW 354.79; 17.3 mg (0.049 mmol)) and K_2CO_3 (FW: 138.21; 35.7 mg (0.258 mmol)) was dissolved in 1.5 mL DMF with stirring at 0 °C for 30 min under Ar. Afterwards, 3 mL of toluene was added to dissolve NROH and 1-bromotetradecane (Aldrich, MW: 277.28; 23.03 mg (0.083 mmol)) was added. The mixture was then stirred in an oil bath at 90 °C under Ar overnight. The reaction mixture was next added to an aqueous solution of 0.1 M $NaHCO_3$ and 1 M NaCl, and the crude product extracted into diethylether. The organic solution was subsequently dried with anhydrous $MgSO_4$, and the solvent was removed. The product was purified by silica gel column chromatography (petroleum ether:EtOAc = 3:1) to obtain a purple solid (FW: 530.36; 17.6 mg (0.032 mmol); Yield: 65%).

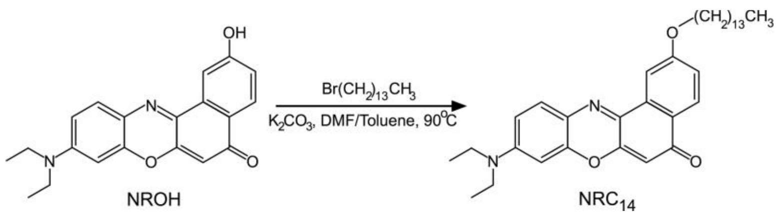

Figure 4.2. Synthesis of NRC_{14}.

4.2.2 Characterization Methods

^{1}H- and ^{13}C-NMR spectra were measured on a Bruker Avance NEO spectrometer (400 MHz for ^{1}H), and chemical shifts were reported in δ values in ppm downfield of tetramethylsilane. Huafang Fan and Herman Coceancigh collected $NRSO_3^-$ NMR data. Exact mass spectroscopy (MS) data were measured at the Mass Spectroscopy Laboratory, University of Kansas.

Figure 4.3 a and b show ^{1}H and ^{13}C NMR spectra for $NRSO_3^-$ respectively. A total of 19 peaks were observed in the ^{13}C NMR when 21 were expected. This difference is attributed to the overlap of peaks within the spectrum, as has been previously observed for similar derivatives of Nile red[122]. Furthermore, the -C-SO_3^- is expected to overlap with the CD_3OH peak. In the case of NRC_{14}, a total of 33 peaks were observed in the ^{13}C NMR when 34 were expected (Figure 4.4a and b). As mentioned above, this difference is also attributed to the overlap of peaks within the spectrum.

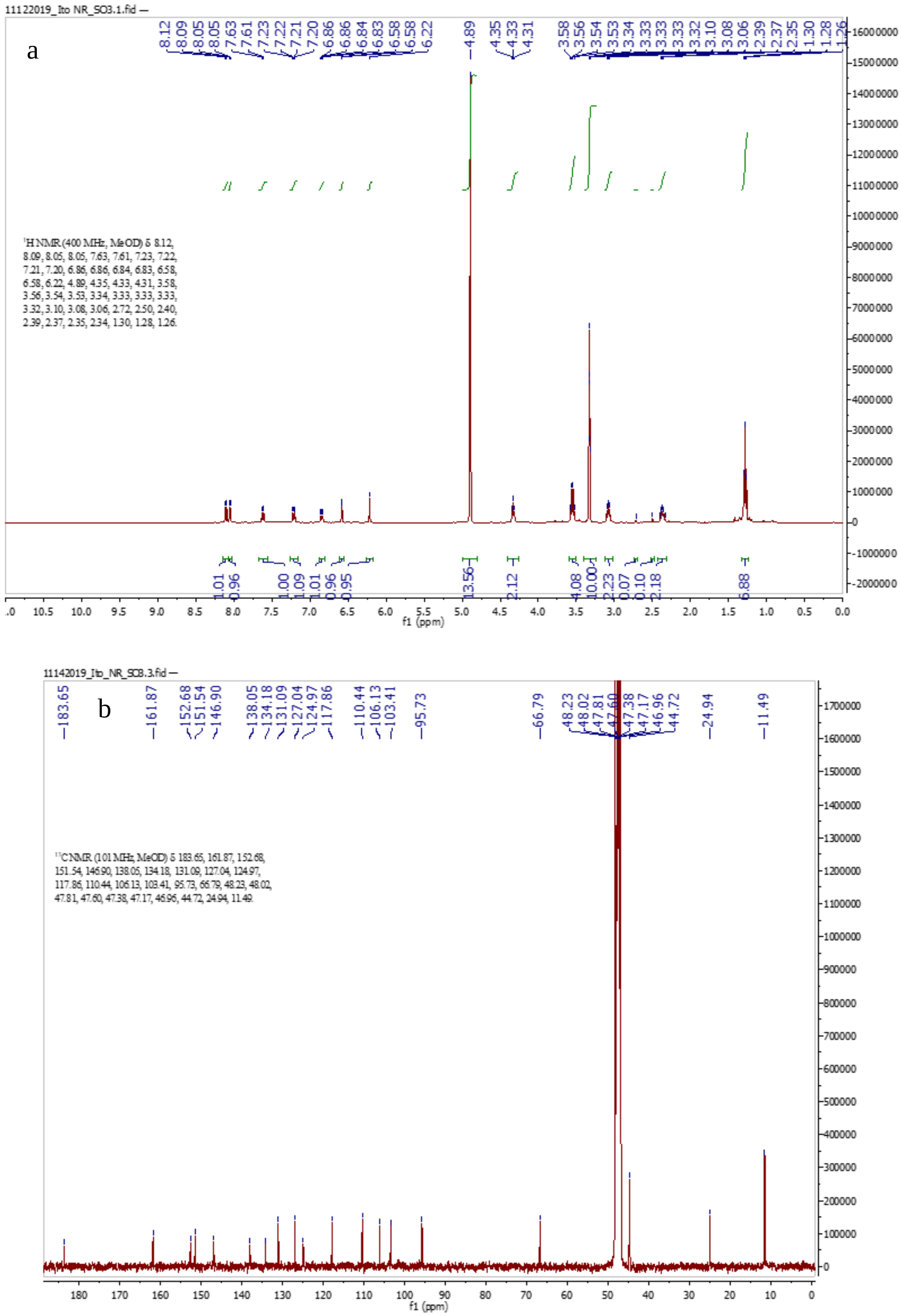

Figure 4.3. a.^{1}H-NMR and b.^{13}C-NMR spectra of $NRSO_3^-$.

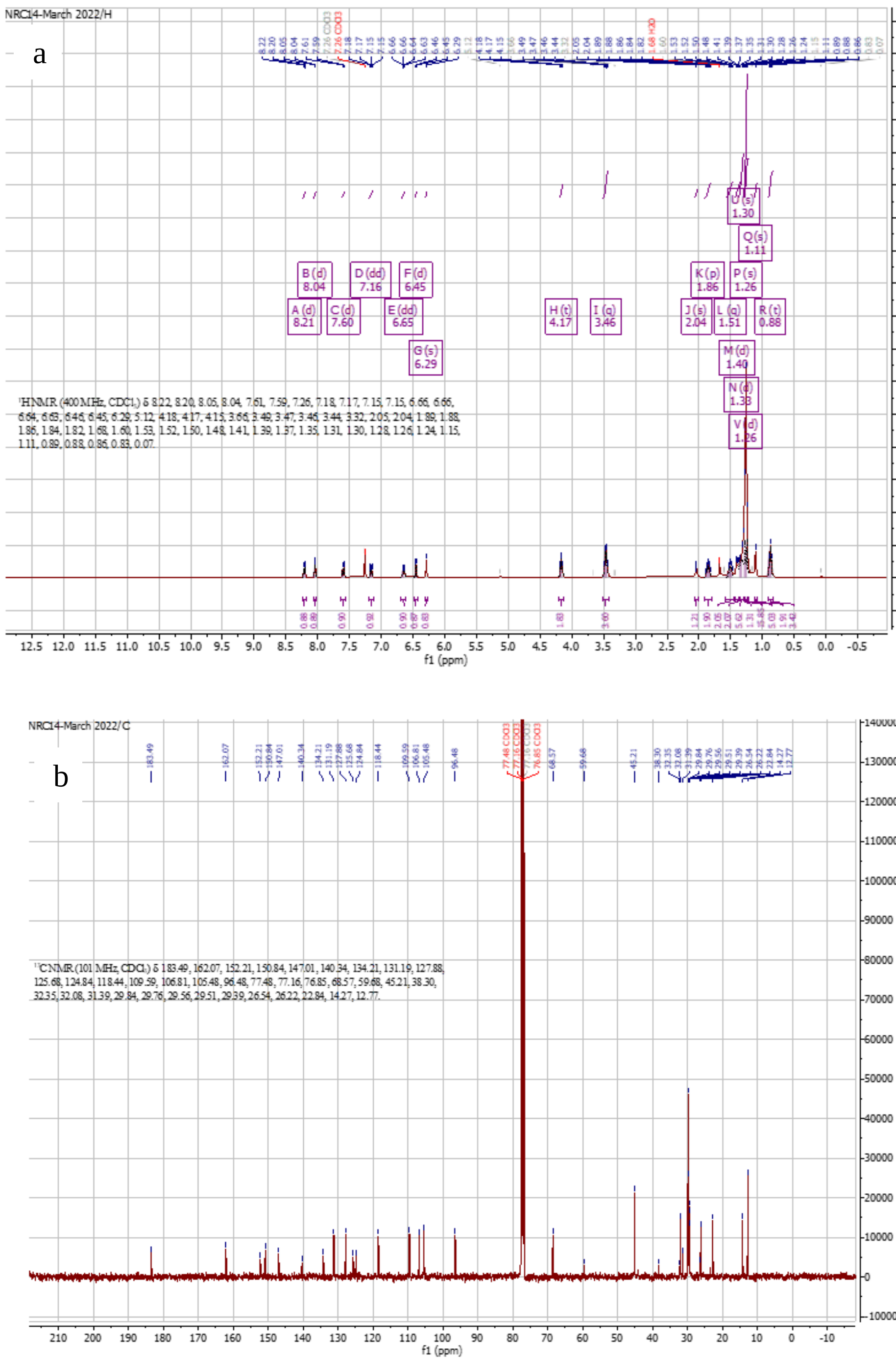

Figure 4.4. a.^{1}H-NMR and b.^{13}C-NMR spectra of NRC_{14}.

Figure 4.5 and Figure 4.6 shows MS spectra of $NRSO_3^-$ and NRC_{14} respectively. The expected mass calculated for $C_{23}H_{23}O_6N_2S^-$ is 455.1277 and was found to be 455.1271. The mass calculated for $C_{34}H_{47}O_3N_2$ is 531.3587 and was found to be 531.3574.

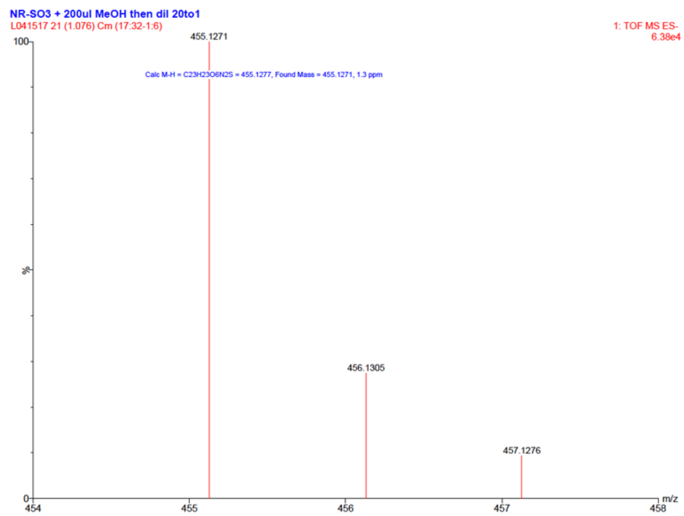

Figure 4.5. Mass spectrum for $NRSO_3^-$.

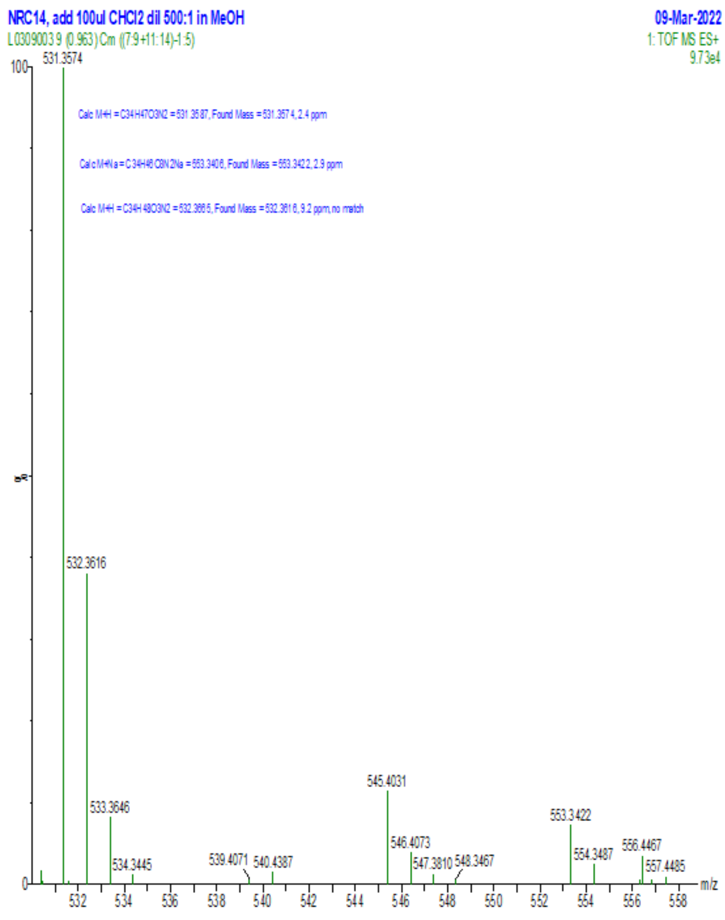

Figure 4.6. Mass spectrum for NRC_{14}.

Small angle X-ray scattering (SAXS) experiments were performed on a Xenocs Ganesha SAXS at the University of Minnesota CharFac. This instrument employs a Cu-Kα X-ray source. Scattered X-rays were detected using an Eiger 1M (Dectris) position sensitive detector. Samples were prepared for these measurements by first warming the gels to 60–70 °C and subsequently loading them into 1 mm diameter boron-rich thin-walled (0.01 mm wall thickness) glass capillaries (Charles Supper) under mild vacuum. Afterwards, the capillaries were sealed with paraffin wax to prevent evaporation of the water. The samples were maintained at ambient temperature under atmospheric pressure during all SAXS measurements. SAXS data were integrated for 300–900 s in each experiment.

Variable area fluorescence correlation spectroscopy (va-FCS) data were acquired on a sample-scanning confocal microscope that was modified from its previously-described configuration[124]. Briefly, the confocal microscope is built upon an inverted fluorescence microscope (Nikon TE-300). It employs an oil immersion objective (Nikon Plan Fluor, 100X, 1.3 NA) for illumination of the sample and for collection of fluorescence emitted by the dye. A single photon counting avalanche photodiode (APD, PerkinElmer SPCM-AQ-141R) was used to detect the fluorescence. Light from a solid-state laser (Coherent Verdi-5W, 532 nm) was used to excite the dye. The laser light was first directed through a telescope to reduce the beam diameter to ~530 μm full-width-at-half-maximum so that it under-filled the back aperture of the oil immersion objective. Under-filling of the objective ensured that a region in the sample a few microns (~2.5 μm) in diameter was illuminated for va-FCS experiments. The laser light was directed into the microscope objective by reflection from a dichroic beamsplitter (Chroma, 550 DCLP). An incident power of 50 μW was typically employed in experiments performed on LLC gels, while 5–10 μW was employed for measurements in pure solvents. The power in each case was measured prior to reflection from the beamsplitter.

Each sample was mounted above the microscope objective within a custom-made cell comprised of a perforated glass slide sandwiched between two microscope coverglasses (FisherFinest, Premium). The gels were transferred into these cells after warming them to 60–70 °C. They were subsequently allowed to cool to room temperature and sealed prior to mounting on the microscope. Unlike previous studies of related materials[125,126], this cell design was not expected to produce well-aligned hexagonal LLCs. Fluorescence was excited in each gel by focusing the incident laser at a distance of ~5 ± 1 μm above the lower coverglass, within the dye-doped gel. The focus was maintained at this position throughout all va-FCS experiments to avoid variations in the FCS results caused by spherical aberrations[127-129].

Fluorescence from the detection volume was collected by the aforementioned objective, passed back through the dichroic beamsplitter, and focused by the internal tube lens of the microscope into a pinhole positioned in its primary image plane. The pinhole employed in each experiment was selected from a series of pinholes on a pinhole wheel (ThorLabs). These pinholes had diameters of 70, 80, 90, 100, and 125 μm. Selection of the different pinhole sizes allowed for the detection area within the sample to be systematically varied. Note that this allows for systematic variation of both the lateral and longitudinal dimensions of the detection region. In contrast, the size of the excitation region was held constant, as has been done previously in imaging FCS experiments[71]. After passage through the pinhole, the fluorescence was sent through an appropriate bandpass filter (Chroma) having a passband centered at 640 nm and a bandwidth of ±20 nm. Finally, the fluorescence was focused onto the photosensitive surface of the APD detector. Individual photon pulses from the APD were counted using a National Instruments counter/timer board (PCIe-6612) configured to operate in the time-stamping mode[130]. Either a 10 MHz or 25 MHz clock was used as the timer for time stamping. The data obtained were used to prepare a series of time transients having bin times of $\geq 10^{-6}$ s. The transients were subsequently processed to obtain autocorrelation functions using C++ written by Eric Higgins and Igor Pro routines written in house. A total of five to ten replicate data sets were acquired from each position within each of the samples over the course of 25 min in each experiment. The individual replicate decays were averaged together to obtain the autocorrelation functions used in the assessment of diffusion rates and mechanisms.

4.3 Results and Discussion

4.3.1 Characterization of $C_{12}EO_{10}$ Gel Nanostructure

Representative SAXS data obtained from a 62.5 wt% $C_{12}EO_{10}$ gel are shown in Figure 4.7 (inset). Three peaks are found at q = 1.268 nm^{-1}, 2.202 nm^{-1}, and 2.522 nm^{-1} in these data. These are assigned to the 10, 11, and 20 Bragg reflections, respectively, of a hexagonal LLC mesophase of cylindrical $C_{12}EO_{10}$ micelles[131]. The 2D SAXS pattern from which these data were derived is provided in Figure 4.8 and reveals that the cylindrical micelles were oriented parallel to the long axis of the glass capillary containing the gel. Figure 2.3b shows a model for the arrangement of $C_{12}EO_{10}$ molecules within the cylindrical micelles, and for hexagonal arrangement of the micelles in the gels. The $C_{12}EO_{10}$ monomer includes a long hydrophilic ethylene oxide segment and a shorter hydrophobic alkane tail. Within the micelles, the alkane segments comprise the nonpolar micelle core, as shown in blue in Figure 2.3b, while the ethylene oxide segments form the more polar corona region, as shown in red[102]. The micelle core is estimated to be ~2.4 nm in diameter based on the fully extended length of the alkane segments, while the corona comprises the remainder of the micelle volume.

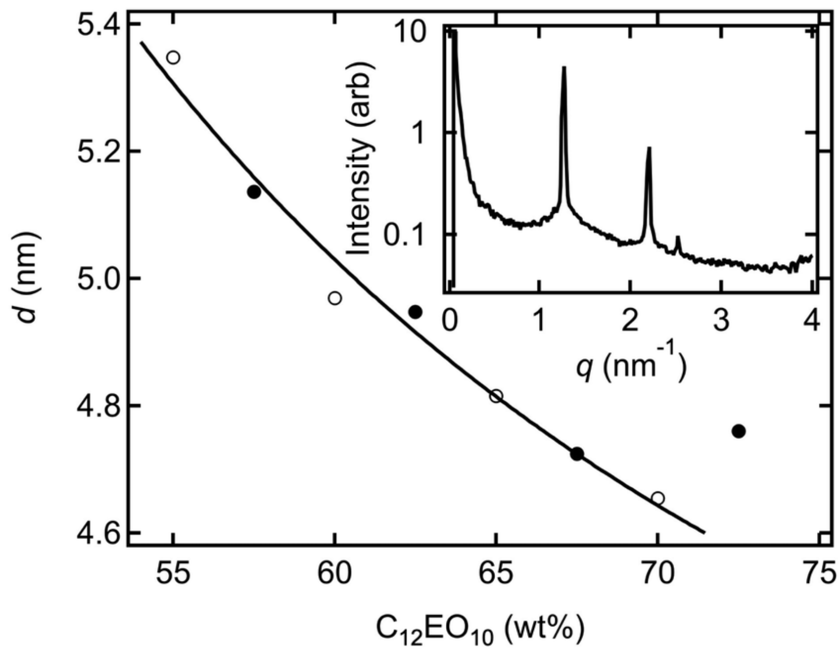

Figure 4.7. Mean SAXS *d* spacing as a function of gel composition for two series of samples prepared on different days (open and filled circles). The inset shows representative SAXS data obtained from a 62.5 wt% $C_{12}EO_{10}$ aqueous gel (300 s integration). The solid line shows a fit revealing the quadratic dependence of *d* spacing on surfactant concentration across much of the range investigated.

Micelle spacing was determined from the 10 Bragg peak, which yields a *d* spacing of 4.96 nm and a lattice *a* parameter of 5.72 nm for the 62.5 wt% gel (Figure 4.7 inset). The distance between micelles was found to decrease with increasing gel concentration. Figure 4.7 plots *d* as a function of concentration for two separate series of samples prepared on different days at 55, 60, 65, and 70 wt% $C_{12}EO_{10}$ and 57.5, 62.5, 67.5, and 72.5 wt% $C_{12}EO_{10}$, respectively. The surfactant concentrations employed are all well above the critical micelle concentration of ~0.10 mM[102,132]. All gels in this range were highly viscous at room temperature and exhibited no evidence of flow over long periods of time.

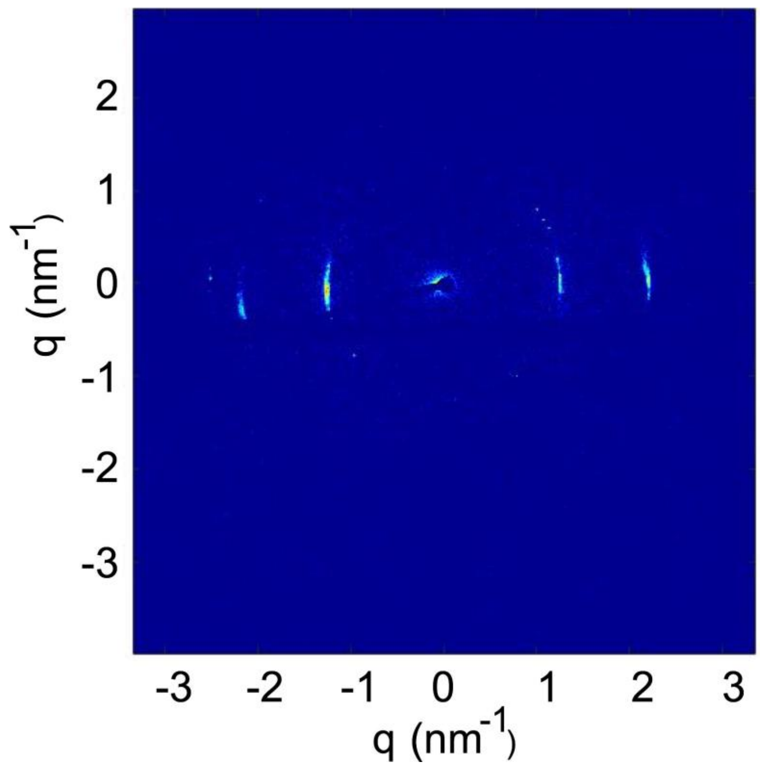

Figure 4.8. Two-dimensional SAXS pattern showing anisotropic scattering from a 62.5 wt% $C_{12}EO_{10}$ gel contained within a thin-walled borosilicate glass capillary. The capillary orientation corresponds to the vertical direction on the image. The results show that the cylindrical micelles are aligned with their long axes oriented along the vertical direction.

Although a detailed phase diagram for $C_{12}EO_{10}$ in water has apparently not yet been reported, phase diagrams for closely related gels (*i.e.* $C_{12}EO_8$[39] and $C_{12}EO_{12}$[101]) have appeared, suggesting a hexagonal phase should be found near the range of concentrations investigated. Indeed, SAXS data acquired from all gels between 55 wt% $C_{12}EO_{10}$ and 70 wt% $C_{12}EO_{10}$ included both 10 and 11 Bragg peaks (data not shown), consistent with hexagonally arranged cylindrical micelles in each case. Data acquired at concentrations above 70 wt% $C_{12}EO_{10}$ exhibited only a single Bragg peak, suggesting a change in phase at higher concentrations.

The trend in d spacing shown in Figure 4.7 is consistent with a $C_{12}EO_{10}$ concentration-dependent increase in micelle packing density. The surfactant aggregation number, and hence, full micelle diameter, likely remain approximately constant across the range of concentrations employed, as has been reported previously[103]. Indeed, a more detailed analysis of the SAXS data reveals an approximately quadratic decrease in d with increasing $C_{12}EO_{10}$ concentration (see fit in Figure 4.7), as expected for a concentration-dependent change in micelle packing density. The only deviation from this trend occurred at >70 wt% $C_{12}EO_{10}$, possibly due to the aforementioned phase transition in the LLC. As a result, the investigations described below were restricted to gels of ≤70 wt% surfactant.

The width of the 10 Bragg peak was also used to determine the correlation length of the organized structures within the gels. The full-width-at-half-maximum (FWHM) was estimated in each case by fitting the diffraction peak (see Figure 4.7) to a Gaussian. The correlation length was calculated as 2π/FWHM, assuming negligible contributions to the width from instrumental broadening. No clear trend was observed as a function of gel concentration. The average correlation length obtained across the range of concentrations investigated was 170 nm ± 90 nm, indicating that the LLCs form domains that remain ordered, on average, over this length scale.

4.3.2 Fluorescence Time Transients and Autocorrelation Functions

The fluorescence time stamping data were used to construct time transients and autocorrelation functions spanning more than six orders of magnitude in time from 1 μs to 3 s. Figure 4.9 shows representative time transients obtained from a 60 : 40 $C_{12}EO_{10}$ gel doped with 20 nM NR dye. These show strong fluorescence fluctuations due to diffusion of dye molecules through the confocal detection region. As expected, the average signal level increases and the time scale over which the fluctuations occur becomes longer with increasing pinhole size. The equation used in autocorrelating the data is given as already given in Equation 3.9.

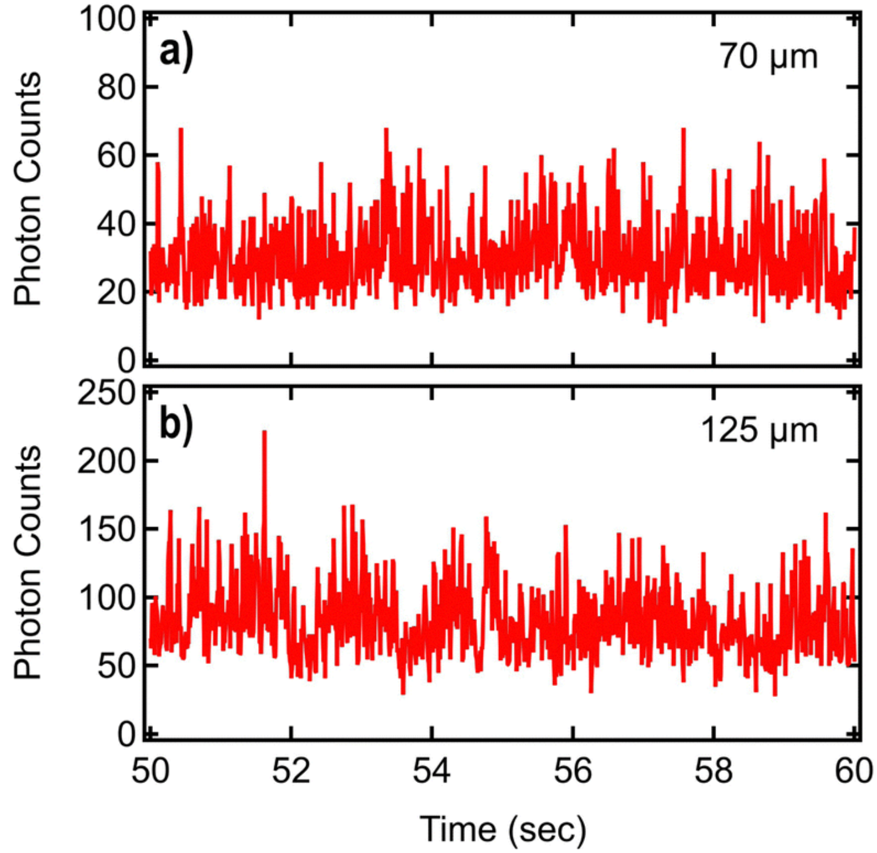

Figure 4.9. Representative segments of time transient data obtained from 20 nM NR in a 60 : 40 $C_{12}EO_{10}$ gel using (a) 70 μm and (b) 125 μm diameter pinholes. These time transients are plotted with 10 ms bin times.

Figure 4.10 plots $G(\tau)$ for two representative data sets. The autocorrelation functions reveal that the fluorescence fluctuations occur on two distinct timescales, producing decays near ∼10 μs and ∼10 ms. The 10 μs fluctuations are too fast to arise from translational diffusion of the dye within the gels. While the fast component is accounted for in fitting the autocorrelation decays (see below), its origins are not relevant to the present studies and are not explored further. The fluctuations occurring in the ∼10 ms range are attributed to diffusion of the dye through the gels and are the sole focus of this study.

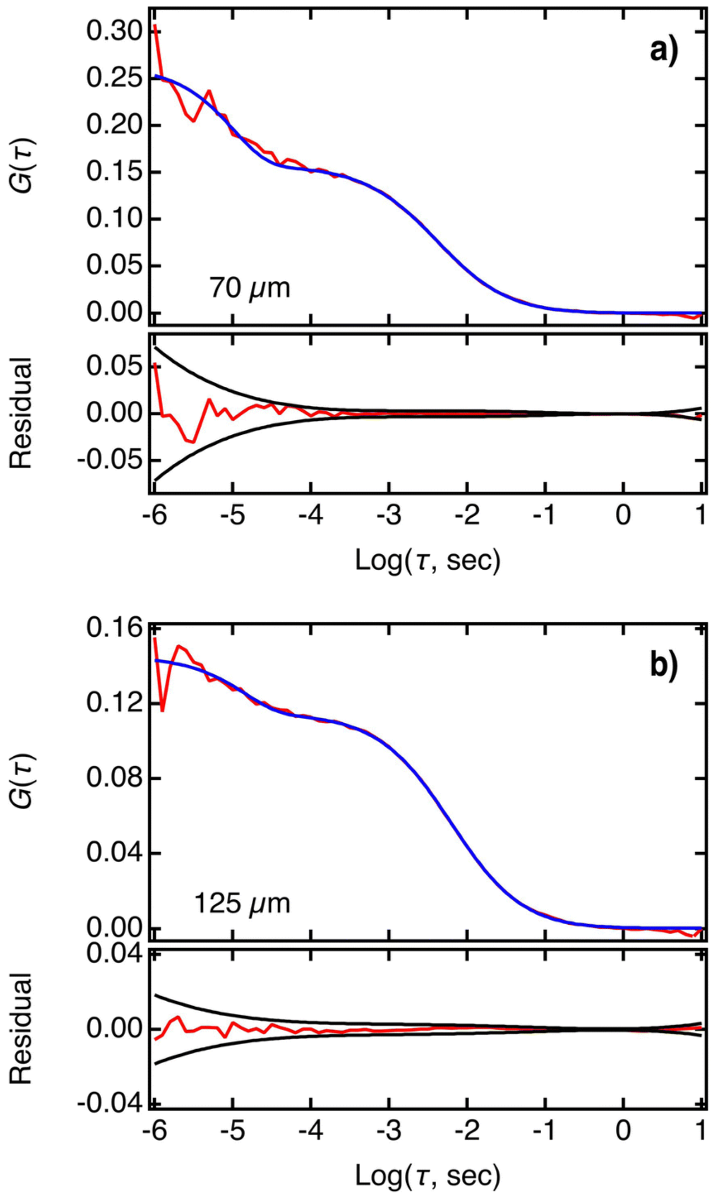

Figure 4.10. Representative FCS data (red lines) obtained from 20 nM NR in a 60:40 $C_{12}EO_{10}$ aqueous gel using (a) 70 μm and (b) 125 μm pinholes. The FCS data depicts the average of five replicate decays. Also shown are their fits (blue lines) to the model given in Equation 4.1. The fitting residuals (red lines) and estimated 95% confidence intervals (black lines) derived from the five replicate decays are plotted below each data set.

The autocorrelation decays afford valuable information on both the rates and mechanisms of dye diffusion. A model that properly describes the diffusion mechanism will afford a good fit to the autocorrelation function, while an incorrect model may not. As it may be possible to fit the data to more than one model, other evidence is usually required to properly assign the diffusion mechanism. According to both the SAXS data obtained (Figure 4.7), and the results of earlier reports[100,125], dye diffusion may be confined to one dimension (1D) by the hexagonally arranged cylindrical micelles of the $C_{12}EO_{10}$ gels . However, as discussed below, all three Nile red dyes appear to be associated with similar environments of relatively high polarity (on average).

The solvatochromism of the Nile red chromophore was used to assess the location of them within the $C_{12}EO_{10}$ gels. In these studies, the emission spectra of NR, $NRSO_3^-$, and NRC_{14} were first investigated in a series of solvent mixtures to confirm that their solvatochromic behaviors are similar. Representative results are shown in Figure 4.11. These data reveal only subtle differences in the response of the three dyes, with $NRSO_3^-$ exhibiting a small (i.e., ~ 3-4 nm) bathochromic shift in its emission, relative to the other two dyes.

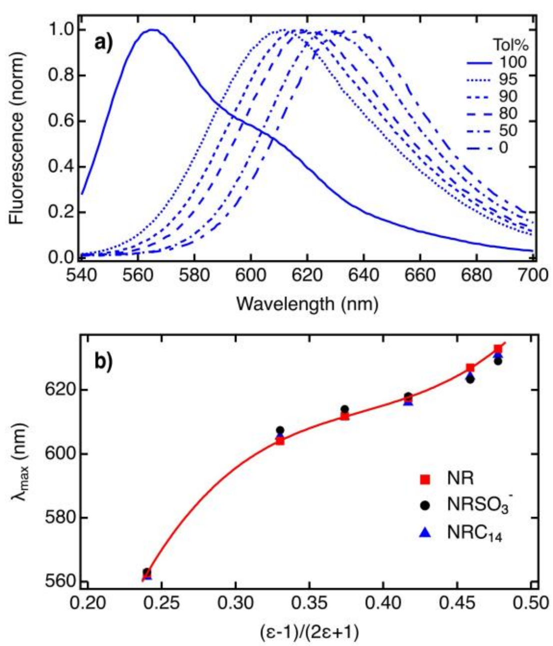

Figure 4.11. a) Representative fluorescence spectra obtained from NRC_{14} in mixtures of toluene and methanol. Each spectrum has been normalized to its peak value. All spectra were excited at 532 nm. b) Emission maximum as a function of estimated solvent Clausius-Mossotti factor for the three dyes (filled symbols).[133] The red line has been added only to better highlight the trend. These data demonstrate that NR, $NRSO_3^-$, and NRC_{14} all exhibit similar solvatochromism.

Ensemble fluorescence spectra obtained from the three dyes in the $C_{12}EO_{10}$ gels were also very similar, as shown in Figure 4.12 for a 60:40 $C_{12}EO_{10}$ gel. The spectra exhibited no clear trends with $C_{12}EO_{10}$ concentration. Interestingly, the $NRSO_3^-$ emission spectrum is shifted to the blue of the NRC_{14} and NR spectra, but only by ~ 2 - 4 nm. These results suggest that the three dyes are found in environments of similar polarity within the gels. Unfortunately, the distance over which the Nile red chromophore responds to the polarity of its environment is unknown. It is also likely that the dye rapidly partitions between distinct environments within the gels, yielding average emission spectra.

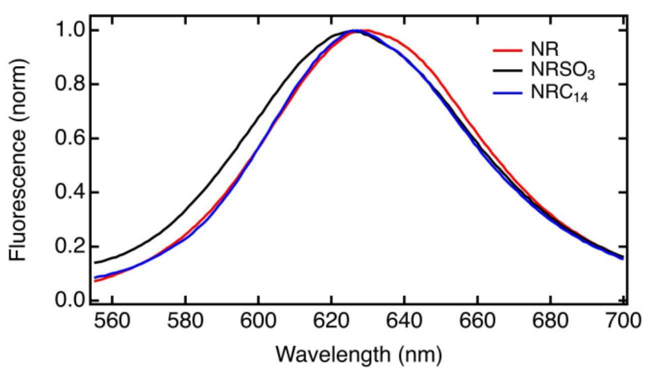

Figure 4.12. NR, $NRSO_3^-$, and NRC_{14} fluorescence spectra in 60:40 $C_{12}EO_{10}$ gels. The spectra were all recorded using 532 nm excitation and each has been normalized to its peak value.

These results suggest they readily partition between the micelle core and corona regions, implying variable contributions from 1D and 3D dye diffusion to the observed fluorescence fluctuations. Indeed, attempts to fit the autocorrelation functions to a model for pure 1D diffusion proved unsatisfactory. Attempts to fit the data to a multicomponent model including both 1D and 3D diffusion yielded highly variable component amplitudes and diffusion times. As a result of these difficulties, a model for anomalous 3D diffusion (Equation 4.1) was instead employed.

$$G(\tau) \approx A + \frac{1}{N}\left[B\left(\frac{1}{1+(\tau/\tau_D)^{\alpha}}\right)\left(\frac{1}{1+(\tau/\tau_D)^{\alpha}(1/\gamma^2)}\right)^{1/2} + Ce^{-k\tau}\right] \qquad \text{Equation 4.1.}$$

Here, A, B, and C are constants defining the contributions of a fixed offset and the amplitudes of the slow and fast fluctuations mentioned above. N is the average number of molecules in the detection region, and k is the rate constant for the fast (~10 μs) fluctuations. The dye diffusion time is given by $\tau_D = w^2_{xy}/4D$, where D is its diffusion coefficient, w_{xy} is the calibrated radius of the detection region and $\gamma = z_0/w_{xy}$. In the latter, z_0 represents the axial dimension of the detection region. The values employed for w_{xy} were quantitatively measured at each pinhole size, as described in the next paragraph. The value of γ was determined to be ~4 from theory, and similar values are reported in the literature[129]. Finally, α describes the occurrence of anomalous diffusion, with $\alpha = 1$ for Fickian diffusion in 3D and $\alpha < 1$ for anomalous sub-diffusion. In these studies, as the dyes were expected to exhibit a combination of 1D and 3D diffusion, values of $\alpha < 1$ were interpreted to reflect the broadening of the autocorrelation decays by the simultaneous occurrence of 1D and 3D dye diffusion. It should be noted that the approximation in Equation 4.1 is valid when $\tau_D \gg 1/k$[134], as is the case in these studies, in which the timescales of fast and slow fluorescence fluctuations differed by a factor of $\sim 10^3$.

The confocal detection area (volume) for each pinhole size was calibrated using solutions of 5nM RhB in ethanol. The diffusion coefficient of RhB in ethanol was determined to be 364 $\mu m^2/s$, as determined from its literature value in water.[135,136] Its diffusion time, τ_D, in ethanol was obtained by analyzing autocorrelation data (fit to Equation 4.1) at each pinhole size. In this case,

a = 1 was used during fitting of the data as no diffusion anomalies are expected in bulk ethanol solution. Calibration was performed for pinholes of 50, 60, 70, 80, 90, 100, and 125 µm diameters. The calibrated radial area of the confocal detection regions was then obtained from Equation 3.6 ($\tau_D = w^2_{xy}/4D$). The results are plotted in Figure 4.13, with the calibrated values of ω_r^2 given on the right ordinate.

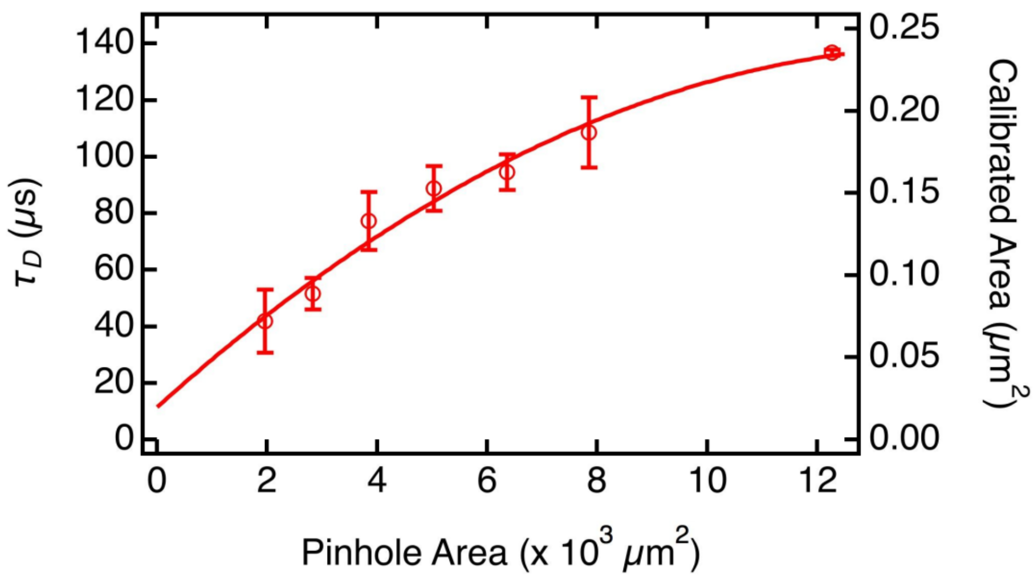

Figure 4.13. Mean diffusion time for Rhodamine B dye in ethanol solution as a function of geometric pinhole area. The error bars show the 95% confidence intervals from three replicate measurements. The calibrated detection area, $\mathbf{w_{xy}^2}$, is shown on the right ordinate. The detection area was determined from $\mathbf{w_{xy}^2 = 4D\tau_D}$, with D = 364 µm^2/s as estimated from its literature value in water[135,136]. The solid line has been appended to better show the trend in the data. The pinholes employed in calibration of the observation area were of 50, 60, 70, 80, 90, 100, and 125 µm diameters.

Figure 4.10 shows representative fits of the autocorrelation data to Equation 4.1. The data were fit from 10^{-6} s to 3 s. The residuals for each fit are shown below each autocorrelation function.

The black lines plotted with the residuals show the estimated 95% confidence intervals. Raw confidence intervals were obtained from the standard deviations of the five replicate decays used to produce the average autocorrelation decays shown. They were subsequently fit to polynomials and the latter are shown as the confidence intervals in Figure 4.10. The residuals all fall predominantly within the 95% confidence intervals, demonstrating the goodness of the fits to Equation 4.1. All FCS data for the three dyes were found to fit best to Equation 4.1, in comparison to the aforementioned alternatives, as judged by the fitting residuals.

Although all autocorrelation data from the gels could be fit well to Equation 4.1, subtle differences in the decays were detected for the three dyes at the different gel concentrations. These imply variations in the molecular-level details of their diffusion mechanisms. In assessing the dye diffusion behaviors, differences in their α values were considered first. The values obtained for all three dyes were found to be independent of pinhole size.

Figure 4.14a. plots their average values as a function of $C_{12}EO_{10}$ concentration. NR yielded the smallest α values of the three dyes. In contrast, $NRSO_3^-$ yielded the largest α values at all but the highest gel concentration, while NRC_{14} exhibited intermediate behavior. The α values obtained from NR and $NRSO_3^-$ in homogeneous glycerin–ethanol mixtures have been included for comparison and are plotted on the right side of Figure 4.14a. Fitting of the data from both of these controls yielded $\alpha = 1$ within experimental error. Data from NRC_{14} in the same glycerin–ethanol mixture appeared to be limited by its low solubility and were not included as a result.

While the exact origins of the smaller α values obtained from NR in the gels remain unknown, it is believed they reflect its greater partitioning into the micelle core regions, and hence, greater contributions of 1D diffusion to its motion. In contrast, the larger values obtained from $NRSO_3^-$ suggest it spends relatively more time in the polar corona regions where it can diffuse in

3D. While NRC_{14} was expected to associate most strongly with the micelle cores, its larger size may prevent it from penetrating the core regions, resulting in its intermediate behavior. In this latter case, transient association of NRC_{14} with the micelle cores may slow its motion while not producing clear 1D diffusion. No clear dependence of α on $C_{12}EO_{10}$ concentration was observed for any of the dyes (see Figure 4.14a.). Therefore, the dimensionality of dye diffusion is believed to be largely independent of micelle packing density at the gel concentrations investigated.

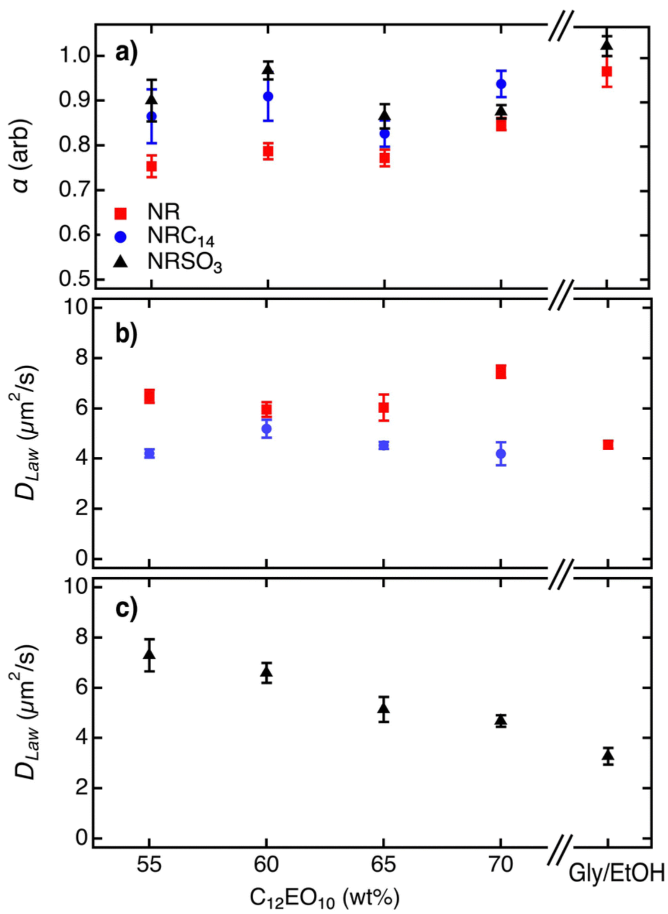

Figure 4.14. (a) Mean α values (Equation 4.1), and (b) and (c) mean diffusion coefficients, D_{Law}, determined by fitting diffusion law plots like those in Figure 4.15 to Equation 4.2 (with $\tau_0 = 0$) for the three dyes at each $C_{12}EO_{10}$ concentration. The data points plotted on the right of each graph

were obtained from homogeneous glycerin–ethanol mixtures (75 : 25). The α values are averaged across all pinhole sizes. The error bars depict the 95% confidence intervals.

Differences in the dye diffusion mechanisms were further revealed by their diffusion coefficients. The latter were obtained by plotting the τ_D values from fits to Equation 4.1 against w^2_{xy}, as shown in Figure 4.15. These plots were subsequently fit to the well-known diffusion law equation, to obtain quantitative measures of D_{Law}[71,73,137]:

$$\tau = \tau_0 + \frac{w_{xy}^2}{4D_{\mathrm{Law}}} \qquad \text{Equation 4.2.}$$

here, w^2_{xy} is the calibrated area of the detection region, and τ_0 is the intercept of the fitted line. Fickian diffusion is expected to yield $\tau_0 = 0$, while domain confined diffusion would yield $\tau_0 > 0$[71,73,137].

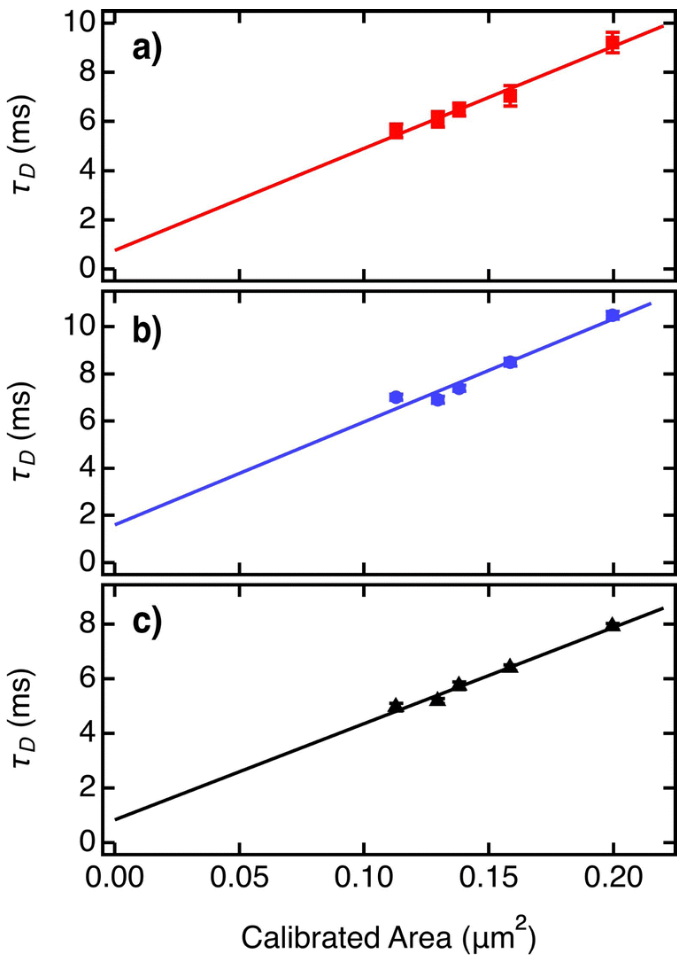

Figure 4.15. Representative diffusion times, τ_D, as a function of calibrated detection area for (a) NR (red squares), (b) NRC_{14} (blue circles), and (c) $NRSO_3^-$ (black triangles) in 60:40 $C_{12}EO_{10}$ gels. All suggest diffusion occurs by a Fickian mechanism. Pinholes of 70, 80, 90, 100, and 125 µm diameters were employed. The solid lines depict fits of the data to Equation 4.2 allowing $\tau_0 \neq 0$. Error bars depict 95% confidence intervals on the autocorrelation fitting parameters.

Confinement of dye diffusion by sub-micron-sized nanostructures has been detected previously in biological samples by diffusion-law analyses like those shown in Figure 4.15, using Equation 4.2[73,74]. Although the lateral dimensions and spacings of the $C_{12}EO_{10}$ micelles are much smaller than the diffraction-limited resolution of the optical microscope employed, the micelles are expected to be a few hundred nanometers in length[104,105], and could therefore yield evidence for domain confined diffusion on similar length scales. Unfortunately, a quantitative statistical test for deviations of diffusion law data from Fickian behavior has not yet been reported in the literature, to our knowledge. A new statistical model and hypothesis test were developed here for this purpose.

The analysis of va-FCS data involves determination of whether plots of the measured diffusion time, τ_D, vs. detection area, ω_r^2, produce a non-zero intercept when a line produced by linear regression of the data is extrapolated to zero area[73,138]. While such an assessment may be qualitatively reasonable, a quantitative statistical analysis of the intercept deviation from zero is challenging. First, the diffraction-limited nature of the method precludes collection of data from detection areas near zero. Statisticians caution against extrapolating to zero under such circumstances[139]. Furthermore, the usual method[57] for assessing the error on the intercept under these conditions does not produce good estimates its value, precluding its use in the usual hypothesis tests.

Here, a simple variant of the above method has been implemented as a means to achieve a valid statistical test of diffusion law analysis results. In this method, the observation area values are simply shifted so that zero corresponds to their mean value, $X_0 = \overline{\omega_r^2}$. The data are then fit by linear regression to a line, $Y = m(X - X_0) + b$. The intercept, b, in this case, falls within the range of measured values and the usual method[57] of estimating its error remains valid. The statistical test employed is the Student's T-test and involves comparing b to the product $m \times \overline{\omega_r^2}$ using the null hypothesis that b = $m \times \overline{\omega_r^2}$. The usual standard errors on the values of m (SE_m) and b (SE_b) are employed, along with that of $\overline{\omega_r^2}$ (SE_{X_0}). Then, the standard error on the product, SE_p, is calculated as:

$$SE_p = \sqrt{\left(\overline{\omega_r^2}\right)^2 SE_m^2 + m^2 SE_{X_0}^2} \qquad \text{Equation 4.3.}$$

The calculated t-statistic is obtained from:

$$t_{calc} = \frac{\left|b - m\overline{\omega_r^2}\right|}{\sqrt{SE_b^2 + SE_p^2}} \qquad \text{Equation 4.4.}$$

The null hypothesis is rejected if $t_{calc} > t_{table}$, where t_{table} is the Student t value obtained at the 95% confidence level, with the specified degrees of freedom. Table 4.1, Table 4.2 and Table 4.3 summarize the results from NR, $NRSO_3^-$, and NRC_{14} in the $C_{12}EO_{10}$ gels and glycerin-ethanol mixtures. Data in the tables were compiled from three replicate measurements on each type of sample.

Table 4.1. Statistical analysis of NR data in $C_{12}EO_{10}$ gels as a function of gel composition (surfactant:water wt%) and in homogeneous 75:25 wt% glycerin-ethanol solution.

NR[a]	**55:45**	**60:40**	**65:35**	**70:30**	**Gly:EtOH**
m (x10^3)	38.0	37.2	39.0	30.1	47.2
SE_m (x10^3)	3.7	4.9	8.6	2.5	3.9
b (x10^3)	5.70	6.22	6.13	4.96	8.14
SE_b (x10^3)	0.11	0.15	0.26	0.07	0.12
$\boldsymbol{m\overline{\omega_r^2}}$ (x10^3)	5.61	5.48	5.76	4.45	6.96
t_{calc}[b]	0.121	0.789	0.252	0.876	1.273
Null Hyp.	accept	accept	accept	accept	accept

[a] In all cases $\overline{\omega_r^2}$ = 0.148 and SE_{X_0} = 0.015.
[b] SE_p and t_{calc} are obtained from Equation 4.3 and Equation 4.4. The value t_{table} = 2.262 (95% confidence, 9 degrees of freedom).

Table 4.2. Statistical analysis of $NRSO_3^-$ data in $C_{12}EO_{10}$ gels as a function of gel composition (surfactant:water wt%) and in homogeneous 75:25 wt% glycerin-ethanol solution.

$NRSO_3^{-}$ [a]	**55:45**	**60:40**	**65:35**	**70:30**	**Gly:EtOH**
m (x10^3)	27.4	29.9	42.7	44.7	60.7
SE_m (x10^3)	7.1	5.2	11.3	6.1	18.2
b (x10^3)	5.10	5.65	7.21	7.94	11.4
SE_b (x10^3)	0.21	0.15	0.34	0.18	0.54
$\boldsymbol{m\overline{\omega_r^2}}$ (x10^3)	4.05	4.41	6.30	6.60	8.96
t_{calc} [b]	0.925	1.384	0.500	1.187	0.831
Null Hyp.	accept	accept	accept	accept	accept

[a] In all cases $\overline{\omega_r^2}$ = 0.148 and SE_{X_0} = 0.015.

[b] SE_p and t_{calc} are obtained from Equation 4.3 and Equation 4.4. The value t_{table} = 2.262 (95% confidence, 9 degrees of freedom).

Table 4.3. Statistical analysis of NRC_{14} data in $C_{12}EO_{10}$ gels as a function of gel composition (surfactant:water wt%). Glycerin-ethanol data were not collected due to limited solubility of the dye.

NRC_{14} [a]	**55:45**	**60:40**	**65:35**	**70:30**	**Gly:EtOH**
m (x10^3)	52.9	41.3	54.1	50.9	NA
SE_m (x10^3)	5.5	7.8	4.0	15.9	NA
b (x10^3)	11.4	9.26	10.5	11.4	NA
SE_b (x10^3)	0.21	0.30	0.15	0.61	NA
$\boldsymbol{m\overline{\omega_r^2}}$ (x10^3)	10.1	7.88	10.3	9.71	NA
t_{calc} [b]	0.883	0.802	0.163	0.533	NA

Null Hyp.	accept	accept	accept	accept	NA

[a] In all cases $\overline{\omega_r^2}$ = 0.191 and SE_{X_0} = 0.019.
[b] SE_p and t_{calc} are obtained from Equation 4.3 and Equation 4.4. The value t_{table} = 2.262 (95% confidence, 9 degrees of freedom).

As mentioned above, the results suggest that all three dyes exhibit Fickian-like diffusion (*i.e.*, τ_0 is not statistically different from zero) in all samples investigated. While the α values reported above suggest different contributions from 1D and 3D diffusion, the diffusion law analysis provides no evidence of domain-confined diffusion[71,73,137]. However, dye motion may actually be confined on length scales too small to detect under diffraction-limited conditions[70]. Note that the LLC correlation length reported above (170 nm) is of similar size to the confocal detection region and suggests that a few (*i.e.* <10) ordered domains are probed in each measurement. These results suggest that all three dyes can diffuse between the organized domains and are not strongly confined by the boundaries between them. They are also consistent with the apparent observation of mixed 1D diffusion within the domains and 3D diffusion between them.

The D_{Law} values obtained, however, do afford additional evidence of differences in the diffusion mechanisms of the three dyes. In this case, the diffusion law plots were reanalyzed with $\tau_0 = 0$ (not shown). Figure 4.14b and c plot the mean D_{Law} values obtained. Data from $NRSO_3^-$ are plotted separately from the other two dyes (see Figure 4.14c) to better highlight the differences in its behavior with $C_{12}EO_{10}$ concentration. A comparison of the D_{Law} values for all three dyes reveals that they are of similar magnitude, as is consistent with the conclusion that the three dyes explore similar environments within the gels (see Figure 4.12). However, a more detailed inspection of the data reveals obvious differences. First, NRC_{14} exhibits the smallest D_{Law} at all gel concentrations, indicating it diffuses most slowly through the gels. NR exhibits modestly larger D_{Law} values, consistent with its smaller size.

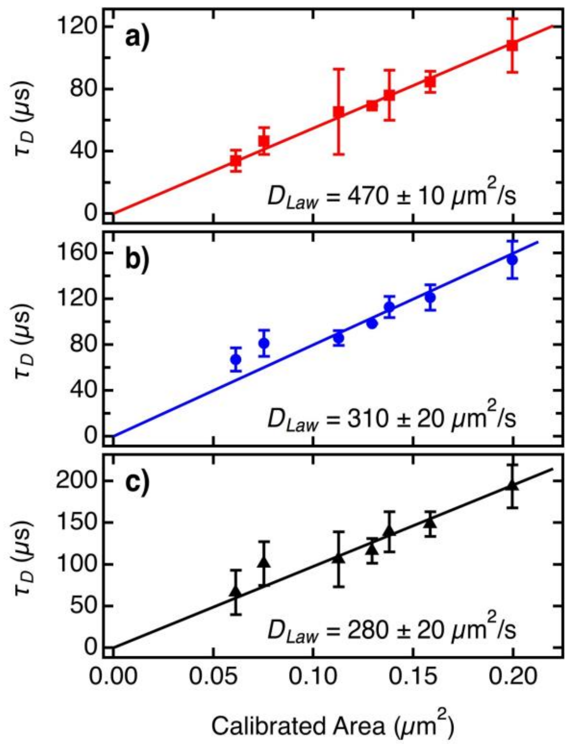

Figure 4.16. a) NR (red squares), b) NRC_{14} (blue circles) and c) $NRSO_3^-$ (black triangles) diffusion times as a function of detection area in ethanol solution. The solid lines depict fits of the data to Equation 4.2 with $\tau_0 = 0$. Mean D_{Law} values obtained from three replicate measurements in each case are shown. The pinholes employed were of 50, 60, 70, 80, 90, 100, and 125 µm diameters. Error bars depict 95% confidence intervals on the autocorrelation fitting parameters.

As it depicted in Figure 4.16, the data obtained for these two dyes in pure ethanol reveal that D_{Law} is 34% smaller for NRC_{14} than for NR in homogeneous bulk solution. Interestingly, NR and NRC_{14} appear to exhibit inverted trends in D_{Law} with gel concentration. NR diffusion appears to be fastest at both low and high gel concentrations and slower at intermediate concentrations. In contrast, NRC_{14} appears to be fastest at intermediate gel concentrations and slower at low and high concentrations. These apparent trends are difficult to explain at present and suggest that their rates of diffusion within the gels may be impacted by several different factors.

Particularly interesting are the data obtained from $NRSO_3^-$, which exhibit a clear monotonic trend to smaller values of D_{Law} with increasing gel concentration, as shown in Figure 4.14c. This trend is attributed to the greater preference of $NRSO_3^-$ for the more polar corona regions of the gel. The dimensionality of $NRSO_3^-$ diffusion may be mostly 3D, as suggested by its larger α values (Figure 4.14a). However, the micelle cores could act as obstacles that confine its motion. As the density of micelles increases, D_{Law} would become smaller as a result. The data shown in Figure 4.14c are consistent with such behavior.

4.4 Conclusions

Variable-area FCS methods were employed to explore the diffusion rates and mechanisms of three Nile red dyes serving as hydrophilic ($NRSO_3^-$), hydrophobic (NRC_{14}), and intermediate polarity (NR) probes of nanostructured hexagonal $C_{12}EO_{10}$ LLC mesophases. The autocorrelation data obtained were analyzed using a model for anomalous 3D diffusion. The results revealed that NR exhibited the most anomalous diffusion, while $NRSO_3^-$ was least anomalous and NRC_{14} exhibited intermediate behavior. These observations were interpreted to reflect increased occurrence of 1D diffusion in this case of NR due to its greater partitioning into 1D micelle core regions. In contrast, $NRSO_3^-$ diffusion likely involves passage through the interconnected micelle corona regions in which it could more readily diffuse in 3D. Indeed, $NRSO_3^-$ yielded a clear monotonic decrease in D_{Law} with increasing gel concentration and micelle density, consistent with confinement of its motions within the gels by the hydrophobic micelle cores. In contrast, NRC_{14} yielded the smallest D_{Law} values at the gel concentrations examined, suggesting its larger size and interactions with the micelle cores slowed its motions. A diffusion law analysis revealed no evidence of domain-confined diffusion on sub-micron length scales for any of the three dyes at the gel concentrations investigated. These results are consistent with dye diffusion occurring by

Fickian-like 1D and 3D mechanisms whose contributions vary between the dyes and with gel concentration within the $C_{12}EO_{10}$ LLCs.

4.5 Acknowledgements

The Division of Chemical Sciences, Geosciences, and Biosciences, Office of Basic Energy Sciences of the U.S. Department of Energy (DE-SC0002362) is acknowledged for partial support of this work. Parts of this work were carried out in the Characterization Facility (CharFac), University of Minnesota, which receives partial support from the NSF through the MRSEC (Award Number DMR-2011401) and the NNCI (Award Number ECCS-2025124) programs. NSF is also thanked for providing the NMR used in characterizing dye structures (CHE-1826982).

Chapter 5 Fluorescence Correlation Spectroscopy Studies of Dye Diffusion on Fresh and Aged Polyethylene Terephthalate

5.1 Introduction

Plastic materials are ubiquitously present in the environment, either escaped from waste streams or carelessly discarded[140]. Over time, these plastics undergo degradation, breaking down into smaller pieces that are called secondary microplastics due to exposure to sunlight, air and mechanical wear by wind and waves[141-143]. This degradation not only causes mechanical breakdown but also gradually changes their chemical composition as their surface undergo oxidization in the air. There are multiple definitions of microplastics, the one that is employed here is provided by Frias et al[144] which says "any synthetic solid particle or polymeric matrix, with regular or irregular shape and with size ranging from 1 μm to 5 mm, of either primary or secondary manufacturing origin⋯"

The physical and chemical properties of plastics are of important ecological and environmental concern. Small microplastics are readily consumed by both terrestrial and aquatic organisms. The ingested microplastics, on their own, are often thought to harmlessly pass through the body[145]. However, multiple recent studies have indicated that microplastics easily adsorb and may later release toxic organic substances, hence playing an efficient role for their transport[146-150]. Insecticides, herbicides, polychlorinated biphenyls, perfluorinated compounds, dioxins, furans, polyaromatic hydrocarbons, pharmaceuticals, dyes, and the metabolites and natural degradation products of all of these are toxic organic pollutants that are known to get adsorbed by the surface of microplastics[141,149,151,152]. Consequently, as microplastics become increasingly prevalent in the environment, the risk of exposure to these substances, and thereby the associated toxic organic chemicals they transport, also escalates[145].

Numerous studies in the literature have explored the sorption phenomenon by microplastics[153-157]. Many of them demonstrating a change in the uptake of organic compounds over the surface of the microplastics as they age[158,159]. The published work focuses mostly on sorption mechanism (i.e., isotherm), strength and kinetics[152,154,160-162]. Most of these studies provide only average results due to the fact that they use bulk methods. As a consequence, there remains a considerable gap in understanding how various organic compounds interact with microplastic surfaces. Specifically, it is unclear whether the organic pollutants permanently adsorb to specific sites or whether they are weakly associated with the sites at first and remain mobile on the surface of the microplastics until they encounter a strong adsorption site. Indeed, a wide range of behaviors is expected depending on the chemical structure of the pollutant and the microplastic and the interaction between them. In order to fully grasp the environmental, ecological and health consequences of microplastics, an improved fundamental understanding of the interactions between organic pollutants and both fresh and aged microplastics is imperative. Additionally, the development of new experimental methodologies is essential for investigating the potential risks they may pose.

One of these methods is fluorescence imaging microscopy which provides a valuable tool to detect sorption of organic pollutants by microplastics[163-165]. Fluorescence correlation spectroscopy or FCS is particularly well-suited approach to these studies[111-113]. It involves measuring fluorescence in time as dye molecules move in and out of the diffraction-limited confocal volume of a confocal microscope. The resulting time transients provide valuable evidence of molecular-level surface adsorption and diffusion. They also serve as a means to quantify the diffusion rate. Furthermore, autocorrelation functions derived from these time transients provide insights into the mechanism and rate of the diffusion. Most significantly, one can explore surface adsorption and diffusion at trace concentrations similar to those at which pollutants are found in the natural environment, by using FCS[166].

In this study, FCS is employed to explore the accumulation and diffusion dynamics of Rhodamine B (RhB) on the surface of synthetic secondary polyethylene terephthalate (PET) microplastics immersed in water. PET is a widely used plastic, especially in drinking water bottles and disposable food packaging due to its good intrinsic barrier properties[167]. Despite its high recyclability, a notable portion of plastic waste present in the environment comprises PET.[147]. RhB serves as a model for toxic organic chemical that can accumulate on PET microplastics in freshwater environments. Its selection is based on several factors: its high fluorescence, excellent water solubility, and possession of functional groups and heteroatoms akin to numerous organic pollutants, their metabolites, and degradation products.[168]. They are also known to be actually released into the environment and accumulate on microplastics[152]. In the current study, the interactions between RhB with both fresh and artificially aged PET microplastics were studied. To artificially age the microplastics, the PET microplastics undergo exposure to the reactive atmosphere within a UV-ozone chamber[159]. Complementary insights were obtained from sessile drop water contact angle measurements, atomic force microscopy, and vibrational spectroscopy.

5.2 Experimental

The synthetic secondary PET microplastics were prepared by sectioning pieces from a single source of virgin biaxially oriented PET plastic sheet (Goodfellow Cambridge). The thickness of the sheet was 100 μm and was optically clear and colorless. Pieces were prepared in ∼2 mm × 3 mm in dimension for ease of handling. In this context, these samples are classified as "synthetic" due to their artificial preparation in the laboratory from larger plastic materials.

The microplastic fragments underwent an initial sonication for approximately 10 minutes in warm soapy water. Subsequently, they were rinsed thoroughly with large amount of deionized (18 MΩ cm) water before undergoing an additional sonication for duration of ∼10 min in warm deionized water. Finally, they were dried under a stream of nitrogen gas. Fresh microplastics were used as obtained after this cleaning process. Artificially aged microplastics were prepared by exposing the clean PET pieces to the reactive atmosphere inside a UV-ozone chamber (Novascan Technologies PSD-UVT), providing UV–C with wavelength of 254 nm, at atmospheric pressure and ambient temperature of 23 °C. The UV-ozone chamber was provided by Dr Takashi Ito. The plastics underwent aging for varying durations, typically ranging from 0.5 to 4 minutes, although in some cases, the aging period extended to as long as 12 minutes.

One method that was employed in this work to study the chemical composition of the fresh and artificially aged PET microplastics was confocal Raman spectroscopy. Raman spectra were obtained initially to verify the composition of the PET plastic and subsequently to explore changes in the chemical composition resulting from aging. These data were obtained on a home-built confocal Raman microscope that was based upon an inverted light microscope (Nikon TE-300). The light source that was utilized was a 532nm laser with power of 1mW. After passing through lenses and polarization optics, the light was reflected from a dichroic mirror (Chroma DCLP 550) and into the back aperture of a high numerical aperture oil-immersion objective lens (Nikon Apo-TIRF, 100X, 1.49 NA). The objective lens focused the laser light through the immersion oil, a cover glass, and through water to a spot of diffraction limited size on the sample surface. The sample was immersed in deionized water and positioned ~ 10 ± 2 μm above the microscope coverglass. Subsequently, the scattered light was collected by the same objective lens, directed back through the dichroic mirror, and focused by the internal tube lens of the microscope onto a 50 μm pinhole positioned in the primary image plane of the instrument. The light then passed through a 532 nm holographic notch filter (Kaiser Optical) into an imaging spectrograph (Acton Research, 300i). Within the spectrograph, the scattered light was dispersed by a 1200 line/mm diffraction grating and imaged onto the photosensitive surface of a thermoelectrically cooled, electron-multiplying CCD camera (Andor, Newton DU-970P-BV). The wavelength axis was calibrated using both a neon lamp and literature results for PET plastic Raman scattering.

Raman spectra in this collaborative project were acquired on the PET plastic samples by Hamid Rashidi. They were acquired by measuring the signal for a total of 25 min. The aforementioned 50 μm pinhole enabled the selective detection of the scattered light with a depth resolution of ~ 825 nm along the laser propagation direction. Since the microscope was focused on the surface of the PET, the Raman scattering spectra thus represents the integrated signal from the first ~ 400 nm of depth of the sample.

Diamond-prism based attenuated total internal reflection Fourier transform infrared (ATR-FTIR) spectroscopy was utilized to further investigate the surface composition of PET microplastics. ATR-FTIR measurements in this collaborative project were performed by Hamid Rashidi. ATR-FTIR was conducted using a Cary 630 benchtop FTIR spectrometer (Agilent) with a single-bounce ATR accessory. To obtain background spectra (64 scans) clean diamond prism was exposed to dry nitrogen gas. Subsequently, a total of 512 scans were averaged during the collection of the sample spectra. The spectra were acquired under dry nitrogen gas with each PET sample pressed face down over the prism using the built-in pressure clamp. The resolution of all spectra was set to 2 cm^{-1}.

Sessile drop water contact angle measurements were conducted using a home-built droplet imaging apparatus that employed a CCD camera and a zoom lens[169]. Freely available software within the ImageJ platform was used to determine the water contact angle from the images obtained[170]. In these measurements, 2.0 μL droplets of deionized water were deposited on each sample and immediately imaged.

Changes to the surface of the microplastics with age were further explored by tapping mode atomic force microscopy (AFM). A Digital Instruments Multimode AFM with Nanoscope IIIa electronics was employed in these studies. Intermittent-contact mode imaging was employed using conical probes (NanoScience Instruments, Aspire) mounted to cantilevers having a resonance frequency of 170 kHz and a spring constant of 50 N/m. For each sample, a minimum of three images of different sample regions ~ 4-5 μm square in size and separated by several hundred microns were acquired. Images were obtained for both fresh and aged samples.

FCS measurements in this collaborative project were conducted by Hamid Rashidi. FCS experiments were carried out on a confocal fluorescence microscope and has been described previously, in detail[31]. This FCS is based upon an inverted light microscope (Nikon TE-200). Fresh and aged microplastic samples were placed in a glass cell. The cell consists of a cylindrical part, attached to a cover glass (FisherFinest Premium) and was positioned above the oil immersion objective lens (Nikon Plan Fluor, 100X, 1.3 NA). The samples were immersed in a solution of 5nM RhB in deionized water. Although PET plastic has a higher density than water (1.30–1.40 g/cm^3)[171], but it was still necessary to secure the PET pieces in place within the cell using a vertically mounted glass capillary. This ensured that the microscope remained focused on the surface of the plastic throughout each experiment. Additionally, the use of the capillary prevented changes in the detection volume caused by optical aberrations when focusing on different depths above the coverslip[127-129].

RhB fluorophores were excited using 2.5 μW (measured prior to entry into the microscope) of 532 nm laser light. The laser followed a similar path to that described earlier for confocal Raman microscopy. In brief, after the laser passes through lenses and polarizing optics, it was reflected from a dichroic mirror (Chroma DCLP 550) and directed into the back aperture of a high numerical aperture oil-immersion objective lens (Nikon Apo-TIRF, 100X, 1.49 NA). The objective lens focused the laser light through the immersion oil, a cover glass, and through water to a spot of diffraction limited size on the PET surface. The emitted fluorescent light was then collected by the same objective lens, directed back through the dichroic mirror, and subsequently focused by the internal tube lens of the microscope into a 50 μm pinhole positioned in the primary image plane of the instrument. The key divergence occurs at this stage. In FCS the fluorescence was collected and refocused through a pair of achromatic lenses and a bandpass filter (Chroma, 580/40m) before reaching the photosensitive element of an APD detector. Pulses from the APD were then counted using a counter/timer board operated in the time-stamping mode[130]. Time transients of arbitrary time resolution of 1 μs to ∼10 s was gained from the time-stamping data by using custom C++ code written by Eric Higgins.

5.3 Results and Discussion

Figure 5.1 presents representative Raman spectra acquired from both fresh and artificially aged PET microplastics.

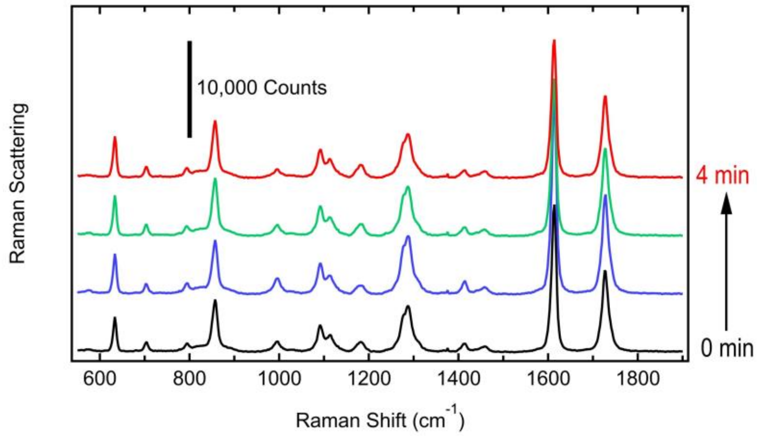

Figure 5.1. Confocal Raman spectra from synthetic secondary PET microplastics as a function of aging time. The spectra were acquired after 0-, 1-, 2-, and 4-min aging times. The spectra have been background corrected and offset vertically to better show each spectrum.

Table 5.1 furnishes a comprehensive list of the observed peaks and compares them to results reported in the literature[172]. Vibrational mode assignments for the individual peaks are also provided. The spectra conform the composition of PET. However, they do not show clear changes in composition as the plastic is aged.

Table 5.1. Comparison of Raman spectra obtained from the synthetic secondary PET microplastics being investigated with literature data.[172] Peak intensity designations: very strong (vs), strong (s), medium (m), weak (w), very weak (vw), broad (br), shoulder (sh).

Lit. Band (cm^{-1}) and Intensity[172]	Band (cm^{-1}) and Intensity	Lit. Assignment[172]
1726 - vs	1727 - vs	C=O stretch
1614 - vs	1613 - vs	Ring C=C stretch
1460 - w	1455 - w	Glycol C-H deformation

1416 - w	1413 - w	Ring C-C stretch
1373 - vw	1375 - vw	Gycol CH_2 wagging
------	1312 - w, sh	
1288 - s	1289 - s	Mixed ring-C=O stretch, O-C stretch, ring CH in-plane bend
------	1283 - m, sh	
1184 - w	1181 - m	Ring CH in-plane bend
1115 - m	1112 - m	Mixed ring CH in-plane bend, glycol C-O stretch
1094 - m	1092 - m	Mixed ring CH in-plane bend, glycol C-O stretch, COC and CCO bend, C-C stretch
998 - w	995 - w	Mixed mode glycol C-C stretch, O-CH_2 stretch and ring torsion
893 - w	------	Glycol CH_2 rocking
858 - s	856 - s	Ring C-C breathing
795 - w	795 - w	Ring CH out-of-plane
703 - w	703 - w	Ring C-C-C out-of-plane bend
632 - m	633 - s	Ring C-C-C in-plane bend

Figure 5.2 depicts a representative ATR-FTIR spectrum obtained for fresh PET plastics while Table 5.2 provides a list of selected peaks observed for it and compares them to results reported in the literature[173]. Furthermore, vibrational mode assignments for the individual peaks are provided. Certain peaks are excluded from the list due to challenges in identifying them amidst the peaks of residual water vapor. Analogous to the Raman data (Figure 5.1 and Table 5.1), even

though the spectra affirm the composition of PET, but it does not show any clear change in composition as it ages. This is attributed to modification of only a thin surface layer because as mentioned before, PET possesses excellent intrinsic barrier properties.

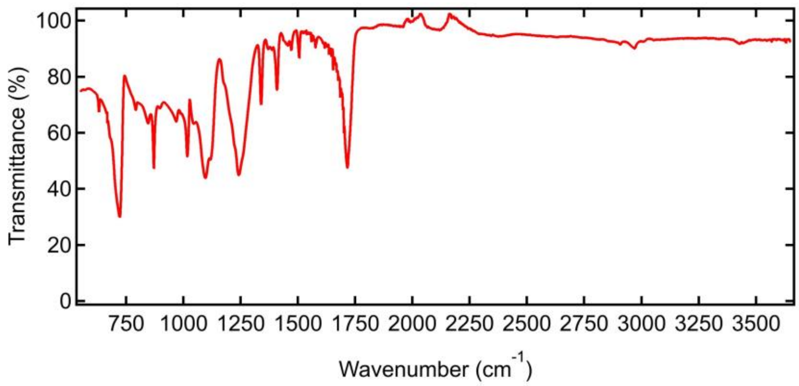

Figure 5.2. ATR-FTIR spectra from fresh PET microplastics. The spectra were acquired under a dry nitrogen atmosphere.

Table 5.2. Comparison of ATR-FTIR spectra obtained from fresh synthetic secondary PET microplastics being investigated with literature data.[173] Peak intensity designations: very strong (vs), strong (s), medium (m), weak (w), very weak (vw), broad (br), shoulder (sh).

Lit. Band (cm^{-1}) and Intensity[173]	Band (cm^{-1}) and Intensity	Lit. Assignment[172]
3560 - w	3540 - vw	OH stretch
3440 - w	3427 - w	C=O overtone
3082 - w	3081 - vw	Ring C-H stretch
3055 - w	3057 - vw	Ring C-H stretch
2970 - m	2970 - m	Asymmetric glycol C-H stretch
2908 - m	2907 - w	Symmetric glycol stretch
1724 - vs	1711 - vs	C=O stretch

1504 - mw	1505 - m	Ring stretch
1410 - s	1409 - s	Combination band550
1343 - s	1340 - s	Ring-C=O stretch
1263 - vs	1243 - vs	Carbonyl C-O stretch
1120 - s	1120 - s	Glycol C-O stretch, crystalline
1100 - s	1096 - s	Combination band with glycol C-O stretch, amorphous
1020 - s	1017 - s	Ring C-H in-plane bend
875 - m	871 - s	Ring C-H out-of-plane bend
727&733 - s	723 - vs	Ring C-H out-of-plane bend

In contrast to the vibrational spectroscopy data, sessile drop water contact angle measurements revealed clear changes in PET surface chemistry with aging. The results are shown in Figure 5.3 for a series of fresh and aged samples. These reveal that the clean, fresh samples are modestly hydrophobic, exhibiting water contact angles of >60°. As the plastics were aged from 0.5 to 4 min, the contact angle gradually dropped to <30°, reflecting an increase in their hydrophilicity. The contact angle remained approximately unchanged from 4 to 12 min of aging. These results are consistent with those from the literature[174]. The enhanced wettability of the aged PET plastic is attributed to the oxidation of its surface.

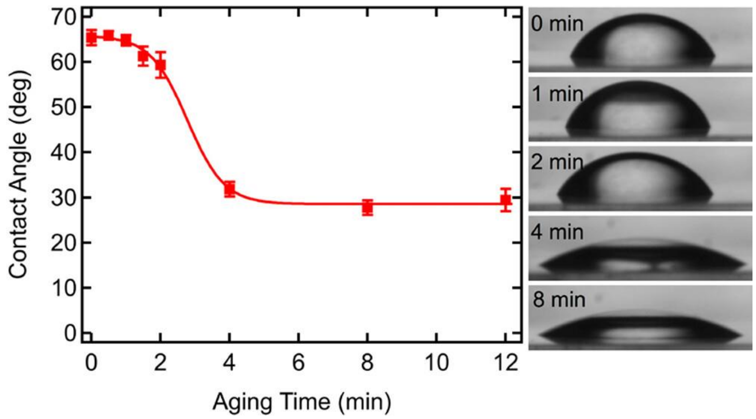

Figure 5.3. Sessile drop water contact angle (filled squares) on synthetic secondary PET microplastics as a function of the aging time. The solid line has been appended to show the trend in the data. The error bars depict standard deviations from three independent measurements. Representative images of each water droplet are shown on the right.

Figure 5.4 provides representative AFM images of fresh and aged PET samples as a function of aging time. Figure 5.5 provides a plot of mean RMS roughness as a function of aging time derived from these images.

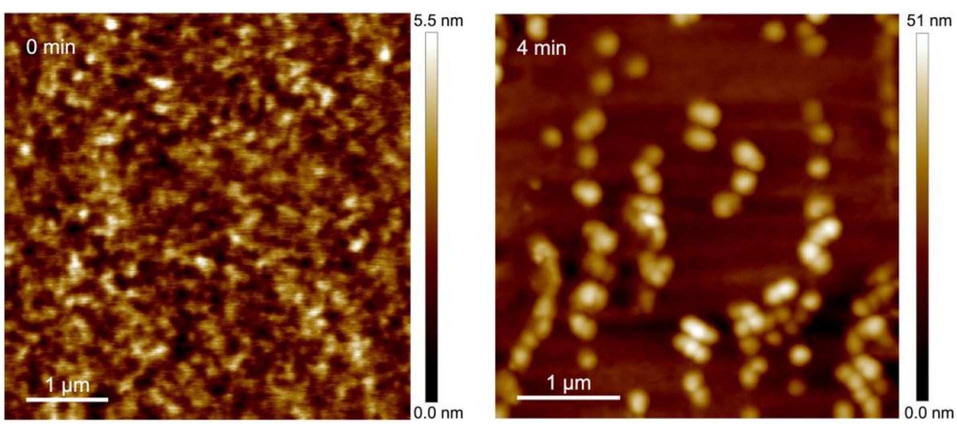

Figure 5.4. Representative intermittent-contact mode AFM images of the microplastic surfaces for both fresh and 4 min artificially aged samples.

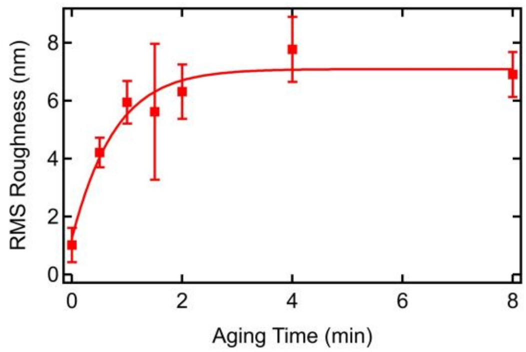

Figure 5.5. Mean RMS roughness for fresh and artificially aged microplastic samples obtained from the AFM images shown in Figure S3 and their replicates (not shown). RMS roughness was determined from the entire image area in each case (~ 20 μm^2). The error bars show the standard deviations on each value. The solid line is included only to show the trend.

The results reveal an average RMS roughness of 1 nm for fresh samples, with roughness growing to ∼7 nm for samples aged for 2 min or longer, as determined over ∼20 μm^2 regions. Images of the fresh samples revealed small irregular features, while the aged samples were dominated by larger round protrusions. Linear features a few nanometers deep are also occasionally observed (not shown) in all samples; these are attributed to the manufacturing process. The observed changes in the surface are similar to those reported previously for PET plastic aging[175,176]. The chemical composition of the protrusions that appear with aging have been attributed to oxidized polymer in the past[175].

Figure 5.6 illustrates representative fluorescence time transients measured on the PET microplastic surface in a 5nM RhB solution. These transients exhibit notable fluctuations in fluorescence emanating from the plastic surface, spanning tens of milliseconds and longer time scales.

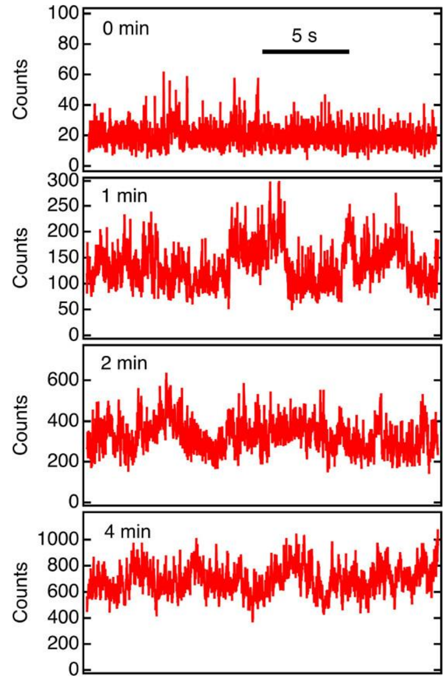

Figure 5.6. Fluorescence time transient segments (counts per 10 ms) acquired from PET microplastics as a function of aging time on a confocal fluorescence microscope. The fluctuations are due to the passage of surface-associated RhB dye through the confocal detection region. The scale bar is 5 s in length. The full transients are ∼150 s in length.

In contrast, the fluorescence time transients acquired from the bulk solution exhibit much weaker fluctuations occurring on sub millisecond time scales, as expected for free RhB diffusion (refer to Figure 5.7a). Figure 5.7b illustrates that the background fluorescence obtained from the microplastic surfaces in the absence of the RhB dye was negligible except for the fresh PET plastic samples. These observations are consistent with adsorption and relatively slow diffusion of the dye across the microplastic surface. Given that PET plastics are known to be glassy and nonporous[177], hence significant sorption of the dye within PET plastics is not likely to occur.

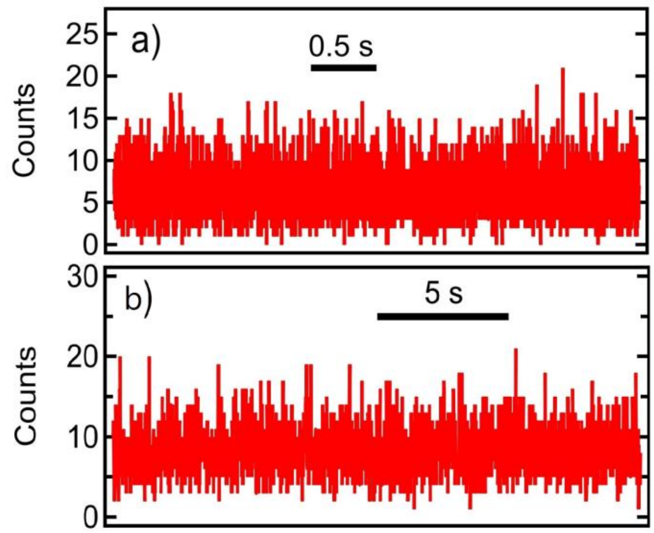

Figure 5.7. Time transient segment showing a) fluorescence signal fluctuations observed at 1 ms time resolution for 5 nM RhB in aqueous solution. The incident laser power at 532 nm was 10 µW and b) background counts observed at 10 ms time resolution from a fresh microplastic surface in the absence of RhB. The incident laser power at 532 nm was 2.5 µW.

Autocorrelation function was employed to quantitatively calculate the rate of RhB diffusion over the PET microplastic surface using Equation 3.9. Figure 5.8 shows representative mean autocorrelation functions obtained from the surfaces of fresh and aged PET microplastics in the presence of 5 nM aqueous RhB solution. The autocorrelation functions were acquired by averaging results from multiple (i.e., ~30) individual data sets and were subsequently normalized to their mean values between τ = 5–15 µs. Figure 5.8 reveals that with aging, the decay times increase monotonically, consistent with the slowing of the dye diffusion process. The rapid decay observed around 1 µs is attributed to triplet blinking of the dye[178] and is irrelevant to these studies.

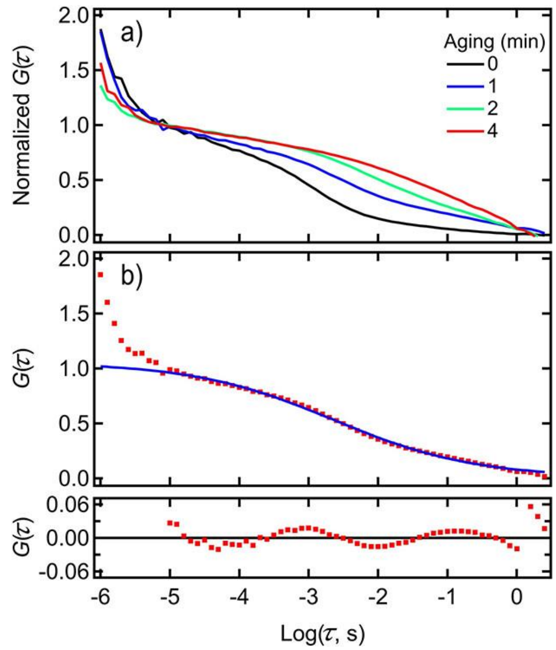

Figure 5.8. (a) Autocorrelation decays obtained from RhB diffusion on the surface of PET plastics as a function of aging time. (b) Representative fit (top, blue line) of autocorrelation data (red dots) for a 1 min aged sample to Equation 5.1 from 10^{-5} to 1 s and the fitting residuals (bottom, red dots). The autocorrelation data in (a) have been normalized based on $G(\tau)$ from $\tau \sim$ 5–15 μs to better show the trend in the data.

The autocorrelation decays were fitted with various models to elucidate the nature of the diffusion mechanism and to quantitatively determine the diffusion time. The decays were found to fit well to Equation 5.1, which approximately models anomalous 2D diffusion[179].

$$G(\tau) = A + \frac{B}{\left(1+(\frac{\tau}{\tau_D})^{\alpha}\right)} \quad \text{Equation 5.1.}$$

In this equation, A represents a negligible constant offset in the autocorrelation function close to zero, B denotes the amplitude of the decay, τ_D is the diffusion time, and α denotes the coefficient of anomalous diffusion. $\alpha = 1$ indicates free Fickian diffusion, $\alpha < 1$ denotes anomalous sub diffusion, and $\alpha > 1$ signifies anomalous super diffusion. Figure 5.8b plots a representative fit (solid blue line) of autocorrelation decay data (red dots) to Equation 5.1. All autocorrelation decays were fit from 10^{-5} to 1 s, with the fits plotted from 10^{-6} to 2.5 s. The fitting residuals are plotted at the bottom of the Figure 5.8b and reveal that the fitted curve deviates from the experimental data by less than 5% across the majority of the fitted range.

Typically, the usual assumption in FCS experiments is that G(0)=1/N, where N represents the mean number of molecules in the confocal volume[111,180]. However, this assumption is not strictly valid in the presence of immobile, surface adsorbed molecules[181], employed in this study. Furthermore, estimating the value of $G(0)$ is challenging due to the sharp rise and poor signal-to-noise ratio in $G(\tau)$ near $\tau \sim 10^{-6}$ s (refer to Figure 5.8a). Nonetheless, a semiquantitative assessment based on the autocorrelation functions from several replicate experiments suggests that N ~ 5 for RhB on fresh plastic and N ~ 20 on 4 min aged plastic, showing greater RhB adsorption as the samples are aged. The latter value corresponds to an approximate surface density of 3.6×10^{10} molecules/cm^2. This value represents an upper bound estimate of the actual surface coverage of mobile molecules and is ~0.03% of a monolayer, assuming 1 molecule/nm^2 represents a complete monolayer.

Figure 5.9a and b depict mean τ_D^{-1} and α values respectively. Figure 5.9a also presents the mean diffusion coefficient, D, as a function of aging time. Here, $D = w^2/4\tau_D$, where w^2 is the calibrated detection area[31]. The mean D value for surface-associated RhB on fresh PET microplastics was found to be ~20-fold smaller than in bulk solution[31]. The rate of diffusion slows substantially as the plastics are aged, resulting in a D value that is ~8000-fold smaller than in solution after only 4 minutes of aging. In addition, the mean α values reveal that RhB motion occurs via anomalous sub diffusion and the diffusion becomes more anomalous as the plastics age.

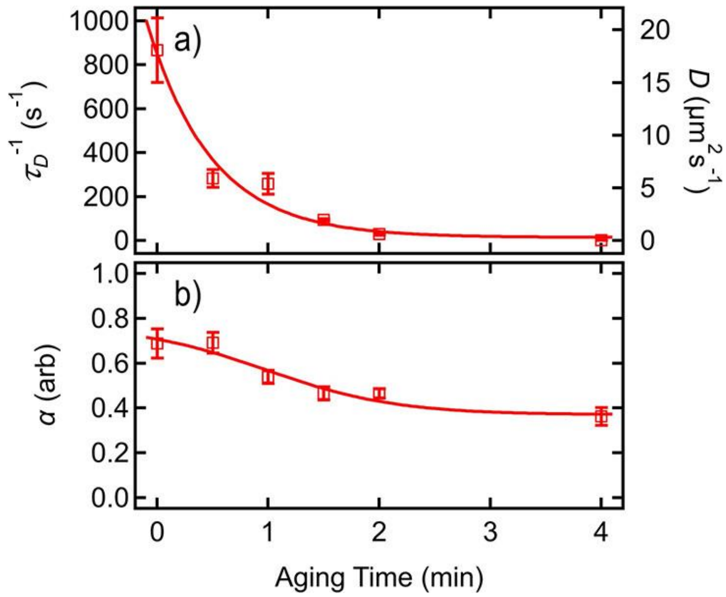

Figure 5.9. (a) Mean rate of diffusion (τ_D^{-1}) and mean diffusion coefficient, *D*, as a function of aging time. (b) Mean coefficient of anomalous diffusion as a function of aging time. The data plotted in parts (a) and (b) were obtained by fitting the autocorrelation decays to Equation 5.1. The error bars depict 95% confidence intervals determined from ~90 replicates. Data at 0-, 1-, 2-, and 4-min aging represent averages from three independent experiments, while the others were repeated twice.

5.4 Conclusions

Altogether, there is substantial evidence showing enhanced interactions between the dye and the plastic surface with increasing aging time. This includes evidence for surface oxidation provided by the water contact angle data and AFM images, the increase in concentration of surface-associated dye, and the dramatic slowing of RhB diffusion. The observed changes could originate from either enhanced ionic interaction between the charged RhB molecules and anionic surface sites or enhanced hydrogen bonding between the dye and surface-associated hydrogen bonding sites (refer to Figure 2.8for RhB molecular structure). However, the exact chemical nature of these interactions requires further study and will be addressed in future works.

The results presented herein demonstrate two distinct phenomena. Firstly, RhB molecules adsorbed on the surface of fresh PET microplastics exhibit mobility, indicative of weak surface association. Secondly, with the aging of PET plastic, the concentration of surface-associated molecules increases dramatically, accompanied by a significant reduction in their mobility. This suggests substantially stronger interactions between the dye and the oxidized surface. A more comprehensive understanding of these phenomena is still needed to properly evaluate the risks of exposure to microplastics and the toxic organic substances that they can accumulate and transport.

5.5 Acknowledgments

Partial support of this work was provided by the U.S. Department of Energy (DE-SC0002362) and the American Chemical Society Petroleum Research Fund (65615-ND9).

Chapter 6 Diffusion Behavior of Nile Red Dye Confined Within Toluene-Ethanol-Filled Anodic Alumina Nanopores

Unpublished work. Sample preparation, FCS and Raman measurements and data analysis were done primarily by the author. Prabhleen Kaur helped with sample preparation, FCS measurements and data analysis and Luqman Olawale helped with data analysis.

6.1 Introduction

Shale rock plays a pivotal role in modern oil and gas production. A published study in 2014 estimated that the global reserves of shale oil comprise approximately about 3 trillion barrels[182] with the United States possessing 68% of these resources. Moreover, shale formations contribute to 50% of the total hydrocarbon production in the US, with 10% of global natural gas production originating from shale rocks[182,183]. The morphology, pore structure, and heterogeneity of shale rocks are critical factors as they influence oil and gas transport within the network of nano- and micro-scale pores and microfractures present in both organic and inorganic matrices. However, despite recent advances, the flow and transport mechanisms in unconventional reservoirs remain incompletely understood[184,185].

Shale rocks exhibit a nanoporous structure with a wide range of porosity reported, from less than 5%[186] up to about 30%[187]. Pore size in shale rocks also spans a wide range, from as small as 2 nm up to as large as 2000 nm[186,188,189]. One study found that pores with 10 nm to 100 nm size constitute 39% of total porosity and contribute most to the pore connectivity and hence to fluid flow[189]. Understanding the flow and diffusion of hydrocarbons confined within these nanopores is of great importance to oil and gas production worldwide. New knowledge in this area will help improve fossil resource production efficiency and will help reveal the mechanisms of resource depletion and aid in the development of new methods for enhanced oil and gas recovery. As the hydrocarbons found in shale rocks constitute complex mixtures, a better understanding of shale porosity on the nanoscale is also certain to aid in the prediction of hydrocarbon composition in liquids produced from these reservoirs. Shale oil contains a myriad of hydrocarbon compounds, including aromatics, as well as straight and branched chain hydrocarbons. It also contains a smaller proportion of oxygenated compounds. Among these, alcohols are the most abundant[190]. The effect of confinement of hydrocarbons in nanosized pores on its phase behavior has been studied extensively[191]. Far fewer studies have explored the effects of confinement on mixtures of hydrocarbons and oxygenated species.

Two main factors of primary interest in understanding the behaviors of liquid mixtures under nanoconfinement are the diffusion mechanisms and diffusion rates[183] of their individual components. While many studies have explored the molecular motions (i.e. diffusion) of pure liquids confined within nanopores, far fewer have looked at how mixtures behave under these same conditions. Hydrocarbon-alcohol mixtures have been studied extensively both experimentally[192-195] and by simulation[196,197] in bulk solution. Most studies of nanoconfined mixtures have involved simulation. Additional experimental data is required to validate the simulation results and to identify any characteristics that may not yet be manifested in model systems. The intricate structure of hydrocarbon-alcohol systems depends on various factors including hydrogen bond association, formation of hydrogen bonded clusters and mesoscopic correlations[193]. In one study, Petterson et al[194], investigated thermodynamic properties of binary hydrocarbon-alcohol systems employing gas chromatography. It was concluded that the mixture thermodynamic properties significantly depend on the alcohol concentration. In dilute alcohol solutions, the thermodynamic properties of the system are determined mainly by hydrogen bonding between alcohol molecules. However, apolar interactions also affect alcohol association. In the mid-concentration range, hydrocarbon πelectron interaction with polar alcohol molecules are dominant while hydrogen bonding takes a secondary role. Finally, in solutions with a high alcohol concentration, apolar interactions primarily define the solution properties.

Abdel Hamid et al.[198] illustrated formation of hydrogen bonded clusters in diluted alcohol mixtures from alcohol monomers. This was also observed using a Kirkwood-Buff model. Mhanna et al.[193] investigated hydrocarbon-alcohol mixtures by small angle neutron scattering, observing an increase in Kirkwood-Buff integrals for low alcohol concentrations. These data also reveal a clustering (or association) of alcohol molecules with each other. Their results suggested that the microstructure of the alcohol depends on size of the alcohol molecule, hydrogen bond interactions and the formation of micellar-like clusters. Ploetz, et al. investigated such mixtures by molecular dynamics simulation and compared the results with experimental data analyzed using the Kirkwood-Buff model in two different studies[196,197]. In both, good agreement was found between the simulation and experimental results. Both studies showed at low concentrations of alcohol (10%-30%) the excess Gibbs free energy of alcohol-alcohol solution shows a maximum. This behavior was interpreted as an indication of extreme clustering of alcohol molecules at low concentrations. As the possibility of hydrogen bonding decreases, greater deviation from a random distribution of alcohol molecules was observed. These studies give valuable insight into the behavior of hydrocarbon-alcohol mixtures in bulk solution. Unfortunately, none of these studies assessed mixture behavior in nanoconfined spaces. Furthermore, there is a notable gap in research concerning the effect of hydrocarbon-alcohol composition on their diffusion properties, both in bulk solution and within porous structures. This gap is particularly crucial when considering the diffusion of hydrocarbon-alcohol mixtures confined within shale pores.

In general, diffusion of fluids through nanopores is influenced by their degree of confinement. Numerous studies have been conducted to evaluate the effects of nanoconfinement on fluid phase behavior[199-202] inside nanoporous shale rocks yet none have specifically addressed hydrocarbon-ethanol mixtures. There are also multiple studies on diffusion[183,203-207] through nanoporous shale rocks. However, the work that has been conducted so far was either by simulation or by using ensemble methods such as NMR. These studies have also focused mainly on diffusion of gases through shale pores, not liquids. Little knowledge on the behavior of liquid mixtures under nanoconfinement can be gained from gas phase data, since intermolecular interactions are largely absent under these conditions. They become very important in the liquid phase.

One drawback of ensemble methods is that they average the behavior of a very large number of molecules. Hence the behavior of each molecule remains unclear. Employing single or near single molecule methods to study diffusion is important specifically for the molecules confined within nanosized spaces such as nanopores. Inside the pores, some molecules might adsorb to the pore surface while others might diffuse through the pore without adsorption. In addition to that, in ensemble methods due to the large detection volume the molecules that are diffusing out of the pores and in the solution will be averaged with the molecules diffusing through the pores. Therefore, a better understanding of molecular diffusion in mixtures under nanoconfinement can potentially be obtained by detecting the motions of individual molecules. This can be done by modern confocal fluorescence microscopic methods.

One method that allows for exploration of the diffusive motions of single molecules (or very small numbers of molecules) is fluorescence correlation spectroscopy or FCS. Importantly, because the associated experiments are performed using a confocal microscope, it affords the means to probe molecular diffusion dynamics within nanoporous materials. Since its inception on 1972[112], FCS has been utilized extensively to study all types of diffusion, including Fickian or non-Fickian[71,72] diffusion in 3D[28], 2D[49], 1D[31]. FCS is a near-single-molecule fluorescent-based technique which employs laser light to excite the fluorescent molecules in the sample and then records the emitted fluorescent light intensity in time under confocal conditions, generating time transient data. The diffusion of molecules in and out of the detection volume changes the number of fluorescent molecules present there, hence varying the fluorescence intensity. The time transients often reveal large numbers of the aforementioned fluctuations, and attempts have been made to analyze these fluctuations individually[208]. However, a more common method for obtaining information on the diffusion of molecules in the sample is to calculate the autocorrelation function for each time transient. The autocorrelation function is then utilized to find the diffusion mechanism and to quantitatively determine the diffusion time and coefficient.

Unfortunately, it was discovered under this project that FCS methods are not applicable to the study of shales because of their high fluorescent background[209,210]. Indeed, the complex hydrocarbon mixtures found in shale rocks are likely to incorporate luminescent molecules that will overwhelm the fluorescence of any purposefully-added tracer species under most conditions. In the present studies, it was therefore necessary to select nanoporous materials that could instead be used as models for natural shales. Various models have been employed previously as models of shale, including graphene, carbon nanotubes, nanoporous carbons, clay minerals, and quartz[211]. Here, anodic aluminum oxide membranes were utilized as a model for shale for the first time, to our knowledge.

Anodic aluminum oxide (AAO) membranes with pore sizes of 10 nm and 20 nm and porosities of 12% were selected as models to mimic the pore structure in shale rocks. Currently, there is limited research on diffusion through nanoconfined pores of AAO membranes[31,212,213]. In one study conducted by the Higgins group, Rashidi et al[31] investigated diffusion of a tracer in ethanol-water mixtures through 10 nm and 20 nm AAO pores. Their findings revealed two distinct diffusion mechanisms inside the pores, namely slow and fast diffusion. The slow diffusion coefficient values ranged from 10 to 100 times smaller than those of fast diffusion. The mixture-dependent trend in the fast diffusion coefficient was similar to that of bulk mixtures of the same composition, revealing its dependence on mixture viscosity. However, the diffusion coefficients were somewhat smaller than in bulk solution. These differences were attributed to hydrodynamic drag and electrostatic interactions between the dye molecules and the pore surface. The slow diffusion values deviated significantly from the composition-dependent trend observed for fast diffusion. In this case, the slow diffusion exhibited a totally different trend compared to the both bulk and fast diffusion coefficient. The latter behavior was attributed to the frequent adsorption of dye molecules onto the pore surface. Consequently, it was concluded that nanoconfinement significantly impacts the diffusion of dye molecules through 10 nm and 20 nm pores filled with ethanol-water mixtures. The effects of nanoconfinement slowed dye motions both by long-range interactions (hydrodynamics and electrostatics) in the case of fast diffusion and by short-range interactions (involving collisions of the dye with the pore surfaces) in the case of slow diffusion.

In the current research, FCS was employed to investigate the mass transport dynamics of NR dye dissolved in a range of toluene-ethanol mixtures confined within the 10 nm and 20 nm pores of AAO membranes. The toluene-ethanol mixture was employed due to the importance of hydrocarbon-alcohol fluids in shale oil production. The time transient data as well as their autocorrelation functions obtained from FCS were employed to evaluate the interactions between the tracer dye and pore surface, to uncover its diffusion mechanism, and to examine the occurrence of any nanoconfinement effects. Furthermore, the FCS also provides quantitative information on the NR diffusion time and diffusion coefficient.

6.2 Materials and Methods

For these experiments, a series of toluene-ethanol mixtures were prepared. The solutions consisted of 0, 20, 40, 60, 70, 80, 90, and 100% (by vol) toluene with the remaining percentage being ethanol. Toluene was procured from Fisher Chemical and ethanol from Decon Labs. Both were used as received. The mixtures were doped with the fluorescent dye NR, at a concentration of 20 nM. NR was obtained from Sigma Aldrich and was used as received. Figure 2.6 displays the molecular structure of NR.

Anodic alumina membranes, measuring 10 mm in size and 50 μm in thickness, were procured from InRedox. They were fragmented and subsequently placed in sample cells for experimental trials. Membranes having pore diameters of 10 nm and 20 nm were used in this study. The 10 nm membranes have a pore density of $1.6 \times 10^{11}\ \mathrm{cm}^{-2}$ and a porosity of 12%. The 20 nm membranes have a pore density of $5.8 \times 10^{10}\ cm^{-2}$ along with a porosity of 12%.

For preparing the sample, the fragmented membrane was immersed in the solution mixture at least overnight. Then, prior to starting the experiment, the membrane was taken out of the mixture and transferred to a sample cell filled with a NR solution (20 nM) of the same toluene-ethanol composition. The sample cell consisted of a cylindrical glass tube with one side glued to a microscope cover slip. The sample cell was then positioned above the microscope objective lens on the confocal fluorescence microscope used for FCS experiments (see below).

Fluorescence correlation spectroscopy was conducted using a custom-built confocal fluorescence microscope. The microscope was built in house by using a commercially available inverted light microscope with a 100X, 1.3 NA oil immersion objective. The objective lens was employed to illuminate the sample and to collect fluorescence emitted by the dye. A 532 nm green laser was employed to excite the sample, with incident power set at either 2.5 μW or 5 μW. The laser light was first directed through a set of two lenses to ensure it is of appropriate diameter and remains collimated. The laser light then reached a dichroic beam splitter which directs it into the back aperture of the objective lens. The objective lens produced a diffraction-limited focused spot of ~ 500 nm lateral dimension in the sample. The light emitted from the sample upon exposure to the incident laser light was collected by the same objective. It then passed through the dichroic beam splitter and was directed onto a 50 μm pinhole. The latter served to define the confocal detection volume in 3D. From the pinhole, the light traveled through a series of lenses and a bandpass filter before reaching the avalanche photo diode (APD) detector. The detector records the number of photons emitted from the sample in time using a National Instruments counter/timer board operating in time-stamping mode. Data acquisition was performed using custom-programmed National Instruments LabView software. Each experiment consisted of ten trials with data acquired from the same position in the sample in each trial. Data collection for each experiment was conducted over a span of 25 minutes. Data analysis was carried out using in-house C++ code and Igor Pro software.

6.3 Results and Discussion

6.3.1 Fluorescence Intensity as a Function of Time: Qualitative Observations

The diffusion of NR fluorophores in bulk solution as well as confined within solvent-filled AAO nanoporous membranes was investigated initially by obtaining and inspecting time transient data from them. Individual dye molecules diffusing through the confocal volume generate short bursts of fluorescence for each event, which are clearly observable in Figure 6.1(a) to (c). This figure depicts representative time transients obtained from 20 nM NR doped 80% toluene-20%

ethanol (X_{Tol}=80% by vol) solution in bulk and in 10 and 20 nm AAO pores. Fluctuations in fluorescence intensity are evident in all three environments.

Despite utilizing the same concentration of NR (20 nM) and laser power for all of the solutions, the fluorescence intensity differs in each case (see Figure 6.1). Variations in fluorescence intensity arise due to several factors. Firstly, the differing duration that each molecule spends in the detection volume creates bursts of different intensities, with molecules that move rapidly producing very little signal. Secondly, the varying number of molecules present in the confocal volume at any given time causes the signal level to increase or decrease proportionately. Finally, the non-uniform laser intensity profile across the confocal volume also contributes a trivial mechanism for intensity variations that is already accounted for in the equations used for data analysis by FCS.

Upon closer examination of the graphs, particularly the expanded version of the time transients provided in the right column, clear differences between the bursts produced by diffusion in bulk solution and from within the pores become apparent. The bursts produced within the pores are much more obvious and are of greater duration than in bulk solution, consistent with a dramatic slowing of dye motions within the pores, when compared to their motions in bulk solution. Furthermore, inside the AAO pores (especially 20 nm AAO pores in this case) there are areas with distinctively higher fluorescence intensity. This is obvious in Figure 6.1 (c) between 39 s to 40 s. Similar slowing of biomolecule and nanoparticle diffusion due to surface adsorption within anodic alumina nanopores has been reported previously[214,215]. This type of behavior is not observed in bulk solution time transients. In addition to these variations between bursts produced in bulk solution and nanopores, the background also differs within nanopores filled with the various toluene-ethanol compositions. This issue will be discussed further, in section 6.3.5.

To quantify the diffusion rate and gain a better understanding of the diffusion mechanism, autocorrelation methods were employed.

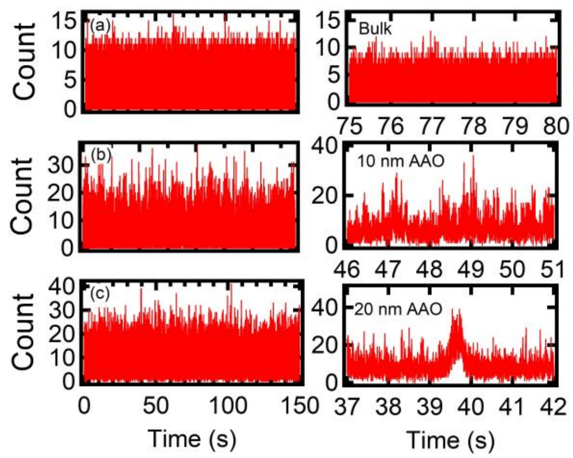

Figure 6.1. Time transient graphs, showing the diffusion of 20 nM NR in X_{Tol}=80% in (a) bulk solution (b) solution-filled 10 nm and (c) 20 nm AAO nanopores. The right column displays an expanded version of each of the time transients. The bulk solution time transient is depicted with 100 µs bin time. The 10 nm and 20 nm AAO time transients are depicted with 1 ms bin times.

6.3.2 Autocorrelation Function and Fitting Results

Autocorrelation analysis of time transient data was employed to find the diffusion mechanism and measure the rate of NR mass transport in both bulk solution and confined within solution-filled 10 nm and 20 nm AAO pores. Equation 6.1 was utilized to obtain autocorrelation data, where G(τ) represents the autocorrelation function, F(t) denotes the time transient at time t, and F(t+τ) represents the time transient at time t+τ. The brackets < > indicate averaging over time.

$$G(\tau) = \frac{\langle F(t)F(t+\tau)\rangle}{\langle F(t)\rangle^2} - 1 \qquad \text{Equation 6.1.}$$

In this study, to enhance the signal to noise ratio, ten autocorrelation functions acquired from the same position in the sample were averaged together. Then, the averaged data was fitted to the appropriate model to determine the diffusion time and rate. Figure 6.2 shows representative autocorrelation data obtained in these experiments.

The autocorrelation decays obtained must be fit by model decay equations in order to establish evidence of the diffusion mechanism and to quantitatively determine the diffusion time and diffusion coefficient. Various fitting models were tested and ultimately employed. Several parameters were considered to identify the best fitting model. Primary factors include the diffusion dimension, the number of diffusion components, and the temporal fitting range. The diffusion dimension is primarily dictated by the environment in which diffusion occurs. For instance, diffusion studied in bulk solution typically corresponds to 3D diffusion, while diffusion over a surface suggests 2D diffusion. Conversely, diffusion through a cylindrical nanopore of relatively great length is likely to be 1D. The number of components of diffusion mainly depends on whether or not there are any interactions between the diffusing molecules and the diffusion environment. For instance, when investigating diffusion inside a 10 nm pore, there could be two components to the diffusion. Some diffusing molecules might interact with the surface of the pore while other molecules might pass through the pore without experiencing any such interactions. In this case, the former may be expected to exhibit slower diffusion compared to the latter. Lastly, the fitting range is also important. Longer diffusion times require a larger fitting range while faster diffusion may allow for fitting only over a narrower range.

Diffusion in bulk solution, outside the membrane, is anticipated to adhere to a 3D diffusion model incorporating only one component. This model is presented in Equation 6.2.

$$G(\tau) = A_0 + \frac{1}{N}\left[\frac{1}{\left(\frac{\tau}{\tau_D}+1\right)\left(\frac{\tau}{\gamma^2\tau_D}+1\right)^{0.5}}\right] \qquad \text{Equation 6.2.}$$

Here, A_0 is an offset, which is close to zero, N denotes the average number of molecules in the confocal volume and τ_D refers to diffusion time. The parameter γ is the ratio of the axial and radial dimensions of the microscope focal volume and remains constant across the measurements. It is believed to be approximately independent of the physical structure (i.e., pore size) of the AAO membranes. A value of $\gamma = 4$ was used in this study[31].

Nile red is anticipated to diffuse in only one dimension within the AAO nanopores. This is justified considering the large difference between the length of the cylinder (50,000 nm) and its diameter (10 nm and 20 nm). Although NR molecules diffuse radially as well as longitudinally within the nanopores, the contribution of radial diffusion is negligible compared to longitudinal diffusion. That is because the radius of confocal volume is 30 to 60 times greater than the radius of the pores and the molecules do not move between pores. The decays obtained from the 10 and 20 nm nanopores (see Figure 6.2, blue and red curves) were too broad, extending from 100 μs to 1 s, to be attributed to one-dimensional (1D) diffusion by a single mechanism alone. Instead, autocorrelation data acquired from within the nanopores were found to fit best to a model incorporating two different 1D diffusion components, characterized as fast and slow mechanisms. As previously mentioned, the slow component of diffusion may be attributed to molecules becoming adsorbed to the pore surface, while the fast component is likely associated with those passing through the pore without experiencing adsorption. Equation 6.3 illustrates this 1D, 2-component model. The first and second terms in the square brackets represent the fast and slow components, respectively. In this model, A_f and A_s represent the fractional contributions of fast and slow diffusion, respectively. Additionally, τ_{Df} and τ_{Ds} denote the fast and slow diffusion times. Equation 6.2 and Equation 6.3 have been employed previously to model 3D and 1D diffusion, respectively[31,216-220].

$$G(\tau) = A_o + \left[A_f \left(\frac{1}{1+\left(\frac{\tau}{\tau_{D_f}}\right)\left(\frac{1}{\gamma^2}\right)} \right)^{1/2} + A_s \left(\frac{1}{1+\left(\frac{\tau}{\tau_{D_s}}\right)\left(\frac{1}{\gamma^2}\right)} \right)^{1/2} \right] \qquad \text{Equation 6.3.}$$

Finally, to obtain diffusion coefficient data, Equation 6.4 was employed.

$$D = \frac{w^2}{4\tau_D} \qquad \text{Equation 6.4.}$$

Here, D represents the diffusion coefficient and w^2 is the calibrated observation area. The value of w^2 is determined by using a solution of a tracer having a known diffusion coefficient. Subsequently, the known value of D for diffusion of the dye was substituted into Equation 6.4 to determine w^2 from the measured value of τ_D.

Figure 6.2 displays autocorrelations of the time transient data presented in Figure 6.1. The black, red, and blue lines correspond to the diffusion of 20 nM NR in X_{Tol}=80% in bulk solution, 10 nm solution-filled nanopores, and 20 nm solution-filled AAO nanopores, respectively. The dashed lines represent the fitted curves for each dataset. The initial decays observable around Log(τ) = -6 (1 μs) are attributed to either triplet blinking of the dye or to detector after pulsing[178,221]. These events are too fast to originate from mass transport even in bulk solution and are not of interest in this study. In some cases, an extra term was utilized in the fitting equations to account for this initial decay in order to ensure accurate data were obtained from later decays. Here, the bulk solution is fitted from 10^{-5} s to 10^{-2} s while the nanopore data is fitted from $10^{-6.4}$ s to 10^{1} s.

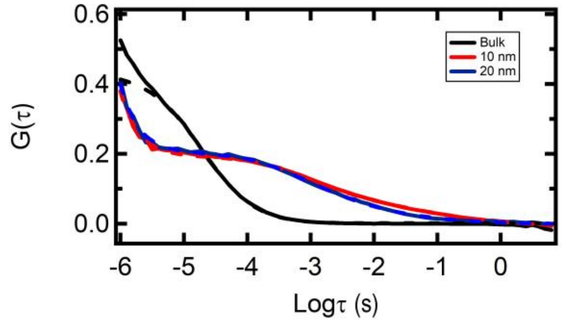

Figure 6.2. Autocorrelation results from the time transients shown in Figure 6.1. The solid lines exhibit the actual autocorrelation data while the dashed lines depict fits of the data to Equation 6.2 and Equation 6.3, for bulk solution diffusion and diffusion inside nanopores, respectively. The bulk solution is fitted from 10^{-5} s to 10^{-2} s while the nanopore data is fitted from $10^{-6.4}$ s to 10^{1} s. The faster decay to zero of bulk solution compared to the results from the 20 nm and 10 nm nanopores is evident in this graph.

The fitting results of the autocorrelation data reveal dramatic differences in the NR diffusion coefficients in bulk solution and confined within the 10 and 20 nm nanopores. The analysis yielded a diffusion coefficient of 750 ± 42 μm^2/s for diffusion of 20 nM NR in bulk 80% toluene-20% ethanol solution. Equation 6.3 was employed to model the diffusion of NR fluorophores confined within 10 nm and 20 nm nanopores. As mentioned above, an extra term (not shown here) was utilized to account for the initial decay around 1 μs. Two diffusion times (fast and slow) were obtained for each pore size using this equation. By substituting their values into Equation 6.4, the fast and slow diffusion coefficients for 10 nm pores were calculated to be 390 ± 25 μm^2/s and 5.9 ± 2.3 μm^2/s, respectively. D_f and D_s for 20 nm pores were calculated to be 580 ± 32 μm^2/s and 56 ± 33 μm^2/s.

Comparing D_f and D_s values of 10 nm and 20 nm pores with each other as well as with bulk diffusion coefficient (D_b) provides valuable initial insights into the effects of nanoconfinement on further slowing of the diffusing molecules. The D_f value obtained is 1.3 times smaller than D_b in the 20 nm pores and 1.9 times smaller than D_b in the 10 nm pores. This shows that the fast diffusion component is moderately hindered, likely by pore-surface interactions, causing molecular motions to slow. Regarding slow diffusion, the difference is more pronounced. While D_s is only 13.5 times smaller than D_b in the 20 nm pores, it is 128 times smaller than D_b in the 10 nm pores. This suggests much stronger interactions, and consequently, a greater slowing of diffusing molecules in 10 nm pores compared to 20 nm pores.

The possible origins of slowed NR diffusive motions within the nanopores are numerous. The NR dye is uncharged, therefore, electrostatic interactions like those believed to lead to surface adsorption of the cationic rhodamine B dye used in other studies[31] cannot occur. Rather, the dominant interactions in the present case likely involve hydrogen bonding, ion-dipole, and dipole-dipole interactions between the diffusing molecules and the charged surface of the pore. Dipole-dipole interactions can happen over longer distances (a few nanometers) compared to hydrogen bonding (a few angstroms). Therefore, hydrogen bonding cannot affect the molecules far from the pore surface. It only influences the molecules that closely approach or collide with the pore surface.

Since toluene is incapable of hydrogen bonding, the main competition for hydrogen bonding to sites on the pore surfaces is between ethanol molecules and NR molecules. With a concentration of 20 nM, there is only 1 NR molecule for every 8.6×10^8 solvent molecules (in pure ethanol solution). This suggests that most of the hydrogen-bonding sites on the pore surface will be occupied by ethanol molecules. Additional experiments were conducted on mixtures having different toluene-ethanol compositions to better understand the effect of pore size, as well as solution composition, on diffusion of NR molecules confined within the pores.

6.3.3 Influence of Solution Composition and Pore Size: Fast Diffusion Component

To comprehensively investigate the effect of solution composition as well as pore size on diffusion within 10 nm and 20 nm AAO nanopores, eight toluene-ethanol mixtures were prepared ranging from 100% toluene to 100% ethanol by volume. The concentration of NR in all samples was 20 nM and the measurements were conducted 5 μm inside the pores. Each mixture was measured 8 times on average. Figure 6.3 (a) illustrates bulk and fast diffusion coefficients as a function of volume percent toluene (X_{Tol}). The bulk diffusion coefficient generally follows the expected trend with viscosity of the mixture, except for 100% toluene solution. The viscosities of toluene-ethanol mixtures have been reported elsewhere[192]. Pure ethanol exhibits the highest viscosity (0.96 mPa·s), which then decreases upon addition of toluene, reaching a minimum (0.52 mPa·s) around 92% toluene. Mixture viscosity subsequently increases slightly to 0.53 mPa·s as the mixture approaches pure toluene. This complex mixture-dependent trend in viscosity could originate from formation and deformation of hydrogen-bonded structures at low ethanol concentrations, as shown previously using Kirkwood-Buff theory[193,196,197]. Since the diffusion coefficient is inversely related to viscosity according to Stokes-Einstein equation, an inverted trend is expected in D_b. This trend is illustrated by the black line in Figure 6.3 (a), in which D_b increases as viscosity decreases with increasing toluene content. The slight increase in pure toluene versus X_{Tol}=90% could originate from temperature instabilities in the lab, or by detection volume variations in the confocal microscope. A mismatch between the refractive index of the immersion medium and the specimen can cause spherical aberrations, which in turn causes variation in confocal volume.

Curriously, NR in X_{Tol}=60% confined within the 20 nm nanopores gave an anomalously small D_f. The reasons behind this anomaly are unknown, but could be the result of experimental error, although replicate measurements did not eliminate its occurrence.

The D_f values for 10 nm and 20 nm pores, while smaller than D_b for mixtures of equal composition, almost exhibit a similar trend as D_b, except for pure toluene. The latter was noted above and will also be addressed later. As can be seen in Figure 6.3 (b), D_f for 20 nm and 10 nm pores is on average 72% and 44% of the bulk diffusion coefficient, respectively. Moreover, comparing D_f values for the 20 nm and 10 nm pores also shows that its value within 20 nm pores is on average 1.6 times greater than in 10 nm pores. Altogether, the results depicted in Figure 6.3 show that while D_f is affected mainly by solvent composition and viscosity of the mixture, it is also clearly hindered by other factors, including by possible interactions between the pore surface and the diffusing molecules that are certain to vary with pore size.

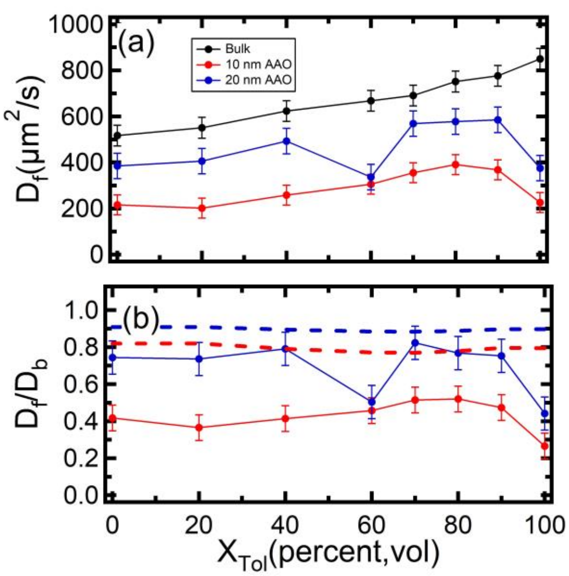

Figure 6.3. (a) Bulk (black solid line) and fast diffusion coefficient of NR molecules confined within solution-filled 10 nm (red solid line) and 20 nm (blue solid line) nanopores as a function of volume percent of toluene. (b) ratio of fast to bulk diffusion coefficient as a function of volume percent of toluene. Dashed lines are predicted values, calculated from the Renkin equation (Equation 6.5). Error bars represent the average 95% confidence interval of all the measurements.

A modified version of Fieller's theorem[222] was employed to calculate the 95% confidence interval of the ratio of means for D_f/D_b.

One possibility that may lead to otherwise unexpected variations in D_f with mixture composition is that the mixture composition within the pores may not be the same as in bulk solution. Such differences in mixture composition have been observed both experimentally and through modeling in other systems such as ethanol-water mixtures[31,223]. Here**,** to compare the compositions of the mixture in bulk solution and confined within the AAO nanopores Raman scattering was utilized. A series of toluene-ethanol mixtures with concentrations ranging from X_{Tol}=90% to pure toluene were made for this purpose. This narrow range of compositions falls in the region where ethanol has been shown to form clusters[193]. Furthermore, it has been shown that quantitative Raman scattering measurements are challenging in all but narrow ranges of mixtures where a linear dependence on composition has been observed[224]. As shown in Figure 6.4, the results of Raman experiments revealed that there is no detectable difference between the composition of bulk solution and that of the solution confined within 10 nm and 20 nm nanopores. This finding contrasts with a previous study from the Higgins group in which water-ethanol mixtures showed some evidence of possible enhancement of the water content within the pores[225].

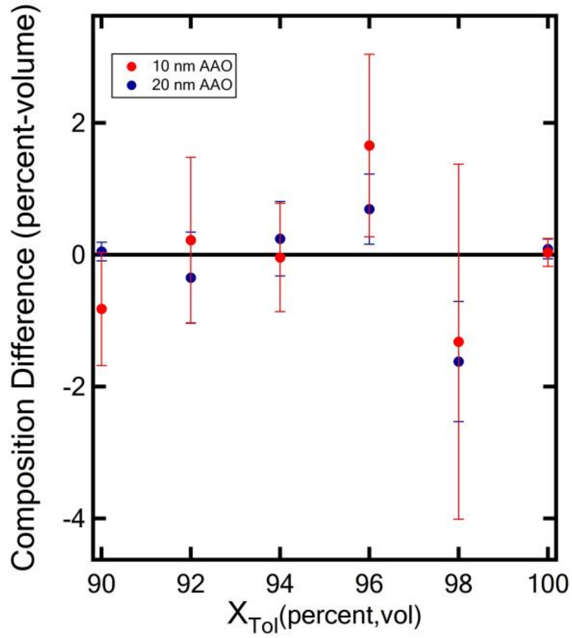

Figure 6.4. Composition difference (bulk-pore) between bulk solution and nanopores. The results show that in almost all cases there is no statistical difference between the composition of the bulk mixtures and the same mixtures within 10 nm and 20 nm pores.

Another phenomenon that can occur inside the nanopores and affect the diffusion coefficient includes the formation of a stagnant layer on the pore surface. This phenomenon has been studied previously in different mixtures including water-ethanol[31,223], non-aqueous phase liquids-water[226], fluorinert-water[227,228] and trichloroethylene-water[229]. While there are apparently no specific studies on toluene-ethanol mixtures, it is possible that a similar phenomenon takes place within toluene-ethanol mixture-filled pores. Given ethanol's polar nature, it is assumed that ethanol molecules can form a stagnant layer over the polar AAO pore surface. In contrast, toluene molecules would be expected to exhibit no such interactions with the pore walls. The stagnant layer of ethanol would introduce hydrodynamic drag on both solvent and solute molecules, slowing down their movements.

The potential impact of such a stagnant layer on the measured diffusion coefficient was further investigated using the Renkin equation[230]. Equation 6.5 presents a modified version of the Renkin equation used previously for modeling hydrodynamic drag monitored inside porous materials alone[31]. Here, D_r is the diffusion coefficient obtained from the Renkin equation, D_b is the bulk diffusion coefficient, r_p is the pore radius and r_{NR} is the hydrodynamic radius of NR obtained from the Stokes-Einstein equation. The D_r/D_b ratios for 10 and 20 nm nanopores are depicted in Figure 6.3 (dashed lines).

$$\frac{D_r}{D_b} = 1 - 2.104\left(\frac{r_{NR}}{r_p}\right) + 2.09\left(\frac{r_{NR}}{r_p}\right)^3 - 0.95\left(\frac{r_{NR}}{r_p}\right)^5 \qquad \text{Equation 6.5.}$$

The calculated D_r/D_b ratios for 10 nm and 20 nm were 0.8 and 0.9, respectively. However, experimental measurements show that D_f/D_b were on average 0.5 and 0.7 for 10 nm and 20 nm pore, respectively. This suggests that factors other than hydrodynamic drag are at play. Since both NR and the solution are uncharged, electrostatic interactions are not a contributing factor. Instead it is believed that ion-dipole and dipole-dipole interactions may play a significant role in further reduction of D_f compared to the Renkin model. It should be noted that only those dye molecules that are slowed down (and not adsorbed to the pore surface) were investigated in this section. The impacts of NR molecules that get adsorbed to the pore surface due to hydrogen bonding are explained in the following section.

6.3.4 Influence of Solution Composition and Pore Size: Slow Diffusion Component

The dependence of the slow diffusion coefficient, D_s, on percent toluene is depicted in Figure 6.5(a). Here, the left and right axes represent D_s for diffusion within 10 nm and 20 nm pores, respectively. Interestingly, while there is no clear trend in this graph for the 20 nm pores, the 10 nm data show a similar trend to what is observed for D_b. This suggests that D_s primarily depends on the interactions between the diffusing molecules and pore surface with a possible secondary dependence on solution composition, and consequently its viscosity. Additionally, comparing D_s values from the 20 nm and 10 nm pores reveals that its value from within the 20 nm pores is on average 11 times greater than in the 10 nm pores. In contrast, as noted above, D_f was 1.6 times greater in the 20 nm pores compared to the 10 nm pores. Figure 6.5 (b) shows the D_s/D_b ratio for 10 nm (red) and 20 nm (blue) nanopores. The ratio for 10 nm pores averages around 0.5% of D_b, whereas for 20 nm pores, its value averages about 5.5%. Altogether, the results show that D_s is even more strongly dependent on pore size than D_f. Smaller pore size leads to more interactions between the NR molecules and the pore surface. As suggested by the time transient data in Figure 6.1, slow NR diffusion is most likely limited by frequent adsorption/desorption of NR molecules to/from the pore walls. While the exact nature of the interactions between NR and the pore surfaces remains unknown, it is plausible that the surfaces provide hydrogen bonding sites as mentioned earlier.

Figure 6.5 (c) plots the contribution of slow diffusion as a function of percent toluene. The results don't reveal any clear trend with mixture composition. However, these data show that while the majority of NR molecules undergo fast diffusion, the population exhibiting such motions is somewhat smaller in the 10 nm pores (~70%) than in the 20 nm pores (~85%). This observation aligns with our expectations, as smaller pore sizes result in molecules being confined within a smaller space, increasing the likelihood of collisions with the pore walls and subsequent adsorption of the dye at those sites. The emergence of the slow diffusion component in nanoporous materials has been reported earlier both experimentally[217,231,232] and by simulation[233].

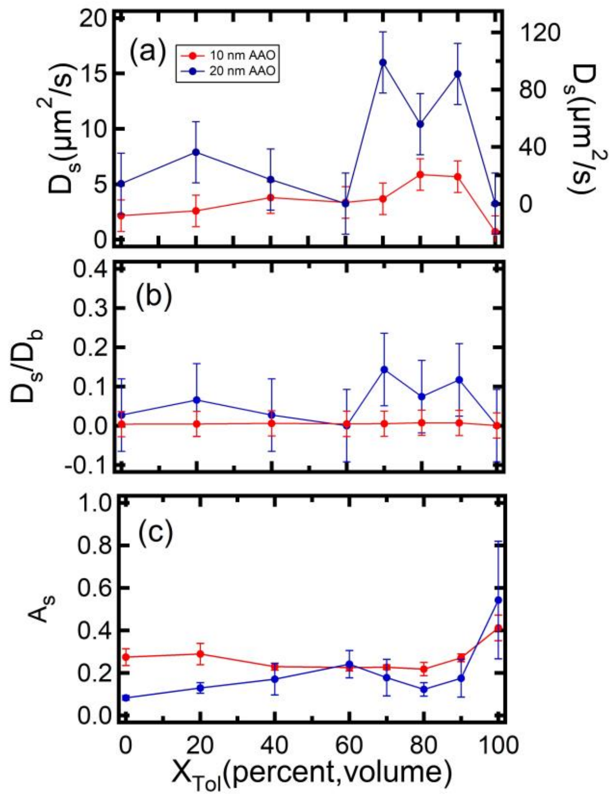

Figure 6.5. (a) Slow diffusion coefficient of diffusion of 20 nM NR confined within 10 nm and 20 nm solvent filled pores as a function of percent toluene. The left and right axis represent D_s for diffusion within 10 nm and 20 nm pores, respectively. (b) the ratio of slow to bulk diffusion coefficient as a function of percent toluene. (c) the relative amplitude of the slow component of the autocorrelation decays as a function of percent toluene. Error bars represent the average 95% confidence interval of all the measurements. A modified version of Fieller's theorem[222] was employed to calculate the 95% confidence interval for the ratio D_s/D_b.

6.3.5 Pure Toluene

Upon closer examination of Figure 6.3 and Figure 6.5 it is evident that 100% toluene behaves differently both in the 10 nm and 20 nm nanopores than in bulk solution. As reported in the literature[192] and as mentioned earlier, the viscosity of pure toluene is slightly larger than that of the 90% toluene-10% ethanol mixture (0.53 vs 0.52 mPa·s). Therefore, the trend shown in D_b

near 100% toluene was unexpected. In contrast to the bulk data, both D_f and D_s exhibit significant drops in their values at 100% toluene in both the 10 nm and 20 nm nanopores. In the 10 nm membrane, D_s is 0.72 ± 0.34 μm^2/s representing the slowest diffusion rate observed. Its value is 7.9 times smaller than D_s for the X_{Tol}=90% mixture. Likewise, D_f for 100% toluene is 230 ± 27 μm^2/s, a value that also demonstrates the slowest rate of diffusion. Its value is 1.6 times smaller than D_f in the X_{Tol}=90% mixture. Regarding the 20 nm membrane, D_s is 0.18 ± 0.18 μm^2/s also marking the slowest diffusion coefficient which is 500 times smaller than D_s of X_{Tol}=90% solution. The D_f for 100% toluene solution is 370 ± 56 μm^2/s displaying the second slowest diffusion coefficient and is 1.6 times smaller than D_f of X_{Tol}=90% solution. These findings suggest that the interactions between the NR molecules and the pore surfaces are significantly stronger in pure toluene than in the mixtures.

In previous discussions concerning the toluene-ethanol mixtures, it was assumed that ethanol predominantly occupies the hydrogen-bonding sites on the pore surface and precluding much hydrogen bonding of the NR dye at these sites. However, in a 100% toluene solution of 20 nM NR, the dye molecules may occupy these same surface sites. This can be seen in Figure 6.5(c), which displays the fraction of NR molecules adsorbed onto the surface (A_s). As shown in this plot, A_s reaches a maximum in the 100% toluene NR solution. This observation is believed to explain the significantly reduced diffusion coefficient of NR molecules confined within the toluene-filled pores. To further investigate the diffusion behavior of 20 nM NR molecules in the toluene-filled nanopores, their time transients have been further examined in depth.

Figure 6.6 presents time transient data for diffusion of 20 nM NR confined within solution filled nanopores. Figure 6.6(a) and (b) illustrate the diffusion of 20 nM NR within toluene-filled 10 nm and 20 nm pores, respectively. Figure 6.6(c) and (d) show the diffusion of 20 nM NR within

90% toluene-10% ethanol-filled 10 nm and 20 nm pores, respectively. The right column shows the expanded version of each of the time transient data shown in the left column. The 100% toluene solutions exhibit fluorescent bursts of longer duration. This is evident in Figure 6.6 (a) between 32 s to 47 s and in Figure 6.6 (b) from 19 s to 24 s. These long (> 1 s) fluorescent bursts are most common in pure toluene only and are not seen in other mixtures. Examination of the expanded versions of the X_{Tol}=90% (other mixtures not shown) figures reveals numerous bursts, albeit with durations less than 1 s. This indicates that while adsorption to the pore surface occurs in both cases (pure toluene and X_{Tol}=90%), in pure toluene solution, the NR molecules move slower on the pore surface and/or desorption from the pore surface is slower. This suggests that the interactions between the dye and pore surface in pure toluene are stronger than in X_{Tol}=90%. As mentioned above, this is attributed to increased hydrogen bonding between NR molecules and the pore surface in the absence of ethanol. These observations deviate from what is expected for simple Brownian motion in 1D.

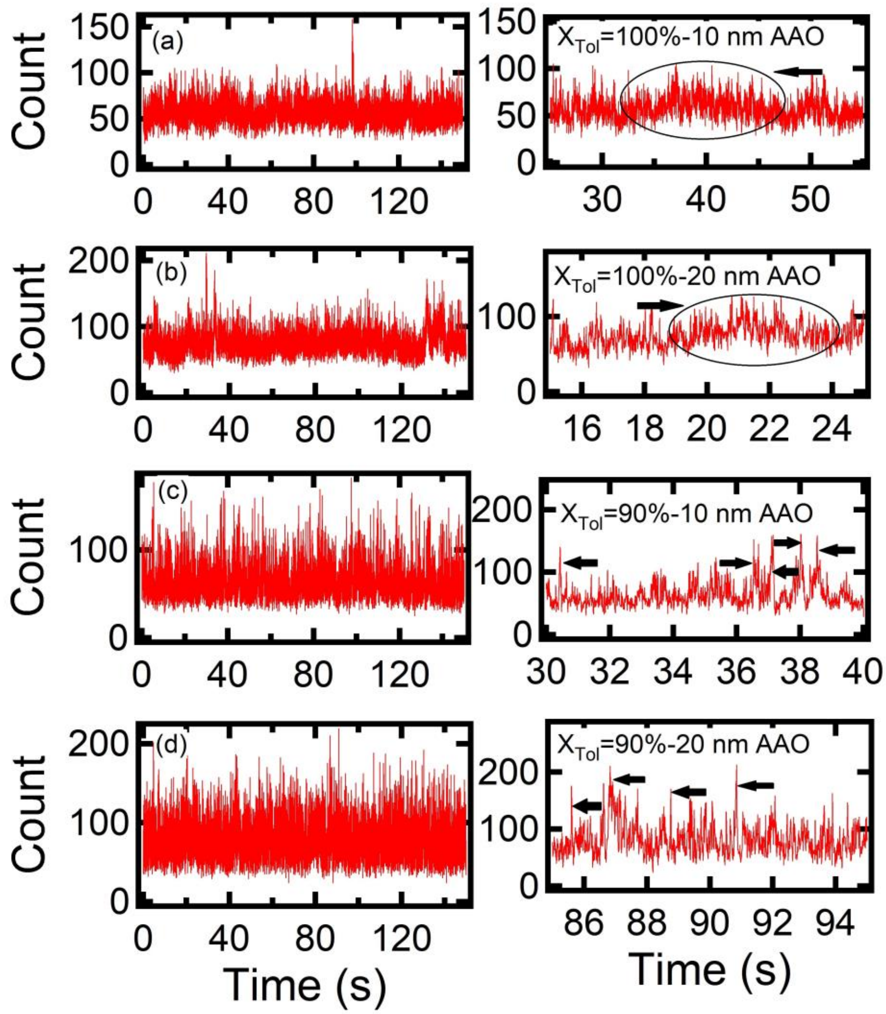

Figure 6.6. Representative time transients displaying burst events that are attributed to NR adsorption on the AAO nanopore surface. The data are depicted for (a) a 10 nm AAO membrane in pure toluene, (b) a 20 nm AAO membrane in pure toluene, (c) a 10 nm AAO membrane in X_{Tol} = 90%, and (d)a 20 nm AAO membrane in X_{Tol} = 90%. The right column shows an expanded version of each time transient. The bin time in each case is 10 ms. The black arrows point to the bursts discussed in the text.

To further investigate the sudden decrease in D_s and D_f for NR in otherwise pure toluene confined within nanopores, a background analysis was performed. The background observed in Figure 6.1 and Figure 6.6, as well as in other time transients (not displayed here), may stem from various phenomena, including light scattering, detector dark counts, membrane autofluorescence, and the adhesion of the dye molecules to the membrane surface. A thorough examination of the background was performed for both 10 nm and 20 nm pores, with the findings illustrated in Figure 6.7. As displayed here, the signal fraction, defined as $\frac{\text{Signal}}{\text{Signal+Background}}$, ranges from 0.1 to 0.2 for both 10 nm and 20 nm pores from pure ethanol to X_{Tol}=90%. However, in pure toluene, the fraction reaches its minimum (~0.043) in the nanopores, regardless of pore size. This indicates a high level of background counts in the 20 nM NR solution of otherwise pure toluene. It suggests a strong adhesion of NR molecules to the AAO membrane surface in the absence of ethanol as expected due to the increased availability of NR hydrogen bonding sites. Furthermore, while the concentration of dye is identical in the two solutions, the amplitudes of the autocorrelation decays due to diffusive motions of the dye are largest in the X_{Tol}=90% filled nanopores and smallest in those filled with toluene. The latter observation is directly attributable to a higher background from immobile NR molecules, which has been demonstrated recently for studies of rhodamine B diffusion in ethanol-water-filled AAO nanopores[225].

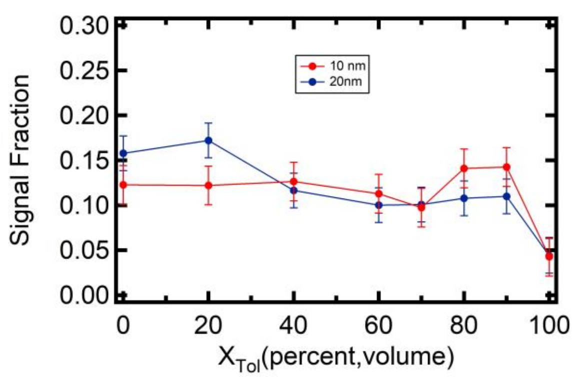

Figure 6.7. Signal fraction as a function of toluene percent. The error bars show the average 95% confidence interval.

Finally, the autocorrelation functions of NR molecules diffusing within pure toluene and X_{Tol}=90% filled nanopores were compared to better observe the differences in their behavior. Figure 6.8 displays the autocorrelation functions of the time transients depicted in Figure 6.6 ((a) to (d)). As can be seen for both 10 nm and 20 nm nanopores, the X_{Tol}=90% solution exhibits a faster decay and reaches zero more quickly compared to pure toluene solution. Diffusion times (τ_{Ds}) of 27±19 ms and 2.6±0.62 ms are obtained for diffusion of pure toluene and X_{Tol}=90% in 10 nm nanopores respectively. These values are 120±67 ms and 0.22±0.09 ms for diffusion in pure toluene and X_{Tol}=90% in 20 nm nanopores respectively. Again, the initial decay around 1 μs is again disregarded as it is too rapid to be associated with diffusion.

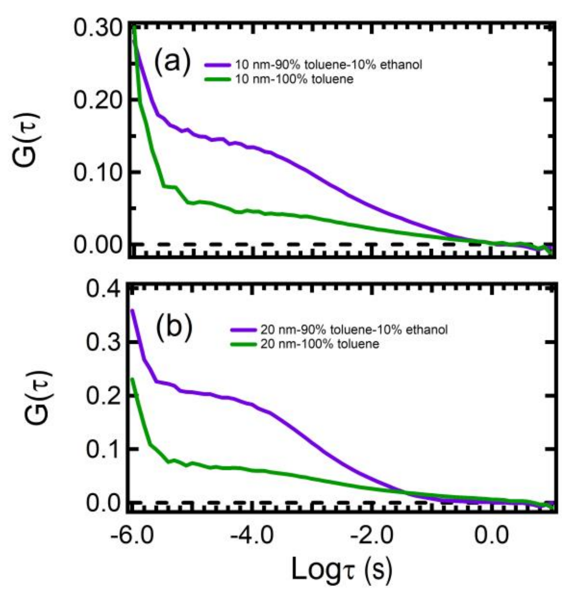

Figure 6.8. Autocorrelation data corresponding to the time transients shown in Figure 6.6. (a) autocorrelation data of diffusion of pure toluene and X_{Tol} = 90% solution-filled 10 nm and (b) 20 nm pores. The black dashed line indicates zero on the y-axis.

6.4 Conclusions

Fluorescence correlation spectroscopy was employed to explore the diffusion behavior of NR doped in a range of toluene-ethanol mixtures confined within 10 nm and 20 nm AAO nanopores. Eight mixtures were prepared with different compositions spanning from pure toluene to pure ethanol. Analysis of time transients obtained by confocal fluorescence microscopy revealed compelling evidence of adsorption and subsequent desorption of dye molecules from the pore surfaces in both 10 nm and 20 nm membranes. Further investigation of the time transients via autocorrelation function analysis revealed two distinct mechanisms for diffusion of NR confined within solvent filled 10 nm and 20 nm AAO membranes, namely slow and fast diffusion. The fast diffusion component was associated with molecules traversing the pore without surface adsorption. The fast diffusion coefficient (D_f) was primarily influenced by the composition of the toluene-ethanol mixture and exhibited a trend consistent with the bulk diffusion coefficient (D_b). The smaller D_f values compared to D_b were attributed to dipole-dipole and ion-dipole interactions between the dye molecules and pore surface. Notably, data obtained from pure toluene exhibited an anomalous slowdown, attributed to the absence of ethanol. The slow component was attributed to dye molecules adsorbing to the surface. Notably, the slow diffusion component exhibited significant dependency on pore size and the interactions between the dye molecules and pore surfaces, with the slow diffusion coefficient (D_s) in 20 nm pores being approximately 11 times greater than that in 10 nm pores. Hydrogen bonding between the pore surface and diffusing molecules was proposed as the underlying mechanism for the surface adsorption. In the absence of ethanol, NR molecules occupied hydrogen-bonding sites on the pore surfaces, resulting in pronounced slowing of their motions in pure toluene. This was evident by comparing autocorrelation data, time transient data, and by a background analysis of pure toluene with

X_{Tol}=90%. The findings of these investigations provide valuable insights into the behavior of solutes and solvents under nanoconfinement within AAO membrane nanopores. The results promise to aid in the understanding of the diffusion of complex hydrocarbon mixtures in nanoporous shale rocks.

6.5 Acknowledgements

The American Chemical Society-Petroleum Research Fund (ACS-PRF) is acknowledged for providing funding for this project through grant number PRF#65615-ND9.

Chapter 7 Conclusion and Future Work

This dissertation describes studies of the mass transport dynamics of molecules confined within soft and hard nano- and micro-structures, by the single molecule spectroscopy method of fluorescence correlation spectroscopy (FCS). The main advantage of using single- or few-molecule spectroscopy methods like FCS in place of ensemble methods is that ensemble methods average the behavior over very large numbers ($\sim 10^{20}$) of molecules. Therefore, the wealth of different behaviors exhibited by individual molecules is masked in ensemble data sets. The FCS studies reported in this dissertation have revealed anomalous diffusion phenomena arising from the adsorption of single molecules to nanostructured surfaces and in nanopores. These phenomena are difficult to detect by ensemble methods. Other characterization techniques such as Raman scattering, AFM, water contact angle measurements, and SAXS were also employed and these have helped to better understand the chemical and physical properties of the soft and hard matter materials investigated in this dissertation. These include $C_{12}EO_{10}$ LLCs, PET microplastics, and AAO membrane nanopores.

In Chapter 4, va-FCS was employed to explore the diffusion rates and mechanisms of three Nile Red dyes, which served as hydrophilic ($NRSO_3^-$), hydrophobic (NRC_{14}), and intermediate polarity (NR) probes of nanostructured hexagonal $C_{12}EO_{10}$ LLC mesophases. The autocorrelation data obtained were analyzed using a model for anomalous 3D diffusion. The results revealed that NR exhibited the most anomalous diffusion, while $NRSO_3^-$ was the least anomalous, and NRC_{14} exhibited intermediate behavior. These observations were interpreted to reflect an increased occurrence of 1D diffusion in the case of NR due to its greater partitioning into the 1D micelle core regions. In contrast, $NRSO_3^-$ diffusion likely involves passage through the interconnected micelle corona regions, allowing for more readily 3D diffusion. Indeed, $NRSO_3^-$ yielded a clear monotonic decrease in the diffusion coefficient (D_{Law}) with increasing gel concentration and micelle density, consistent with the confinement of its motions within the gels by the hydrophobic micelle cores. In contrast, NRC_{14} yielded the smallest D_{Law} values at the gel concentrations examined, suggesting that its larger size and interactions with the micelle cores slowed its motions. A diffusion law analysis revealed no evidence of domain-confined diffusion on sub-micron length scales for any of the three dyes at the gel concentrations investigated. These results are consistent with dye diffusion occurring by Fickian-like 1D and 3D mechanisms, with contributions varying between the dyes and different gel concentrations within the $C_{12}EO_{10}$ LLCs.

For future work, one area to explore is changing the concentration and hence phase of the $C_{12}EO_{10}$ LLCs to investigate its effect on diffusion and partitioning of NR dyes. Another idea involves employing a different type of surfactant yielding the formation of cores with radii comparable to the radius of the observation region. This would help us to obtain more exact data after applying FCS diffusion law. Finally, considering the solvatochromic properties of NR, utilizing two-color FCS could be beneficial to study their behavior. Two-color FCS would allow for the simultaneous measurement of the diffusion of NR dyes in different environments within the LLCs. This technique could provide more detailed information on how the dye molecules partition between different regions, such as the micelle core and corona, and how their environment affects their fluorescence properties. This approach could lead to a deeper understanding of the microenvironments within the LLCs and how they influence the behavior of solute molecules.

In Chapter 5, FCS was utilized to investigate the diffusion of RhB molecules over the surface of fresh and aged PET microplastics. Raman scattering, ATR-FTIR, AFM, and water contact angle measurements were employed to characterize the effects of aging on PET microplastic surface chemical and physical properties. The results demonstrated that RhB molecules adsorbed on the surface of fresh PET microplastics remained mobile, indicating a weak surface association. As the plastics aged, the concentration of surface-associated molecules increased dramatically, while their mobility decreased significantly. This observation suggests much stronger interactions between the dye and the oxidized PET surface. A more detailed understanding of these phenomena is required to properly assess the risks associated with exposure to microplastics and the toxic organic substances that they accumulate and transport.

For future work, one area to study is employing fluorescent probes with different polarities and charge compared to RhB. Such studies would help elucidate the impact of pollutant polarity and molecular charge on the surface adsorption strength and may reveal that more polar molecules accumulate more on aged PET surface compared to RhB. Another idea for future work involves studying the samples in water with different salinity and pH, better mimicking natural bodies of water. The ionic strength of the environment would impact the adsorption of the dye molecules to the PET surface.

In Chapter 6, FCS was employed to explore the diffusion behavior of NR doped in a range of toluene-ethanol mixtures confined within 10 nm and 20 nm AAO nanopores. Eight mixtures were prepared with different compositions spanning from pure toluene to pure ethanol. Analysis of time transients obtained from FCS revealed compelling evidence of adsorption and subsequent desorption of dye molecules from the pore surfaces in both 10 nm and 20 nm membranes. Further investigation of the time transients via autocorrelation function analysis revealed two distinct mechanisms for the diffusion of NR confined within solvent-filled 10 nm and 20 nm AAO membranes: slow and fast diffusion. The fast diffusion component may be associated with molecules traversing the pores without adsorbing to their surfaces. The fast diffusion coefficient (D_f) was primarily influenced by the composition of the toluene-ethanol mixture and exhibited a viscosity-dependent trend consistent with that observed for the bulk diffusion coefficient (D_b). The smaller D_f values compared to D_b were attributed to dipole-dipole and ion-dipole interactions between the dye molecules and the pore surface. Notably, data obtained from pure toluene solutions exhibited an anomalous slowdown, attributed to the absence of ethanol and thus, longer range interactions between charged sites on the pore surfaces and the NR dipole moment. Conversely, the slow component was attributed to dye molecules adsorbing to the surface and subsequently desorbing. This slow diffusion component exhibited significant dependence on pore size and the interactions between the dye molecules and pore surfaces, with the slow diffusion coefficient (D_s) in 20 nm pores being approximately 11 times greater than that in 10 nm pores. Hydrogen bonding between the pore surface and diffusing molecules was proposed as the underlying mechanism for surface adsorption. In the absence of ethanol, NR molecules occupied hydrogen-bonding sites on the pore surface, resulting in pronounced deceleration of its diffusive motions. Enhanced adsorption of the NR dye in pure toluene was made evident by comparing autocorrelation data, time transient data, and background analysis of pure toluene with a mixture of 90% toluene (X_{Tol} = 90%). The findings of these investigations provide valuable insights into the behavior of solutes and solvents under nanoconfinement within AAO membrane nanopores.

For future work, one possible pathway involves changing the polarity of the pore surface by modifying the AAO membranes. This would help to investigate the effects of pore polarity on fast and slow diffusion coefficients. Another field for future work includes using different pore sizes to further explore the effects of nanoconfinement. Finally, measuring NR solubility in toluene-ethanol mixtures and simulation studies both can give better understanding of NR behavior under nanoconfinement. Solubility data enhances the understanding of the FCS data and elucidates the role of interactions between the solvated dye molecules and pore surface in governing NR surface adsorption and slow diffusion. Simulation can be employed to investigate the possibility of formation of a stagnant layer inside the pores.

Chapter 8 References

(1) Nelson, E.: *Dynamical Theories of Brownian Motion*; Princeton University Press, 1967.
(2) Einstein, A.: *Investigations on the Theory of the Brownian Movement*; Dover Publications, 1956.
(3) *Diffusion NMR of Confined Systems: Fluid Transport in Porous Solids and Heterogeneous Materials*; The Royal Society of Chemistry, 2016.
(4) Baer, A.; Wawra, S. E.; Bielmeier, K.; Uttinger, M. J.; Smith, D. M.; Peukert, W.; Walter, J.; Smith, A.-S. *The Stokes–Einstein–Sutherland Equation at the Nanoscale Revisited*. Small, n/a, 2304670.
(5) Liu, Z.; Chen, K.; Davis, C.; Sherlock, S.; Cao, Q.; Chen, X.; Dai, H. *Drug delivery with carbon nanotubes for in vivo cancer treatment*. Cancer research 2008, 68, 6652-6660.
(6) Tasciotti, E.; Liu, X.; Bhavane, R.; Plant, K.; Leonard, A. D.; Price, B. K.; Cheng, M. M.; Decuzzi, P.; Tour, J. M.; Robertson, F.; Ferrari, M. *Mesoporous silicon particles as a multistage delivery system for imaging and therapeutic applications*. Nature nanotechnology 2008, 3, 151-157.
(7) Dong, B.; Pei, Y.; Mansour, N.; Lu, X.; Yang, K.; Huang, W.; Fang, N. *Deciphering nanoconfinement effects on molecular orientation and reaction intermediate by single molecule imaging*. Nature Communications 2019, 10, 4815.
(8) Somerville, S. V.; O'Mara, P. B.; Benedetti, T. M.; Cheong, S.; Schuhmann, W.; Tilley, R. D.; Gooding, J. J. *Nanoconfinement Allows a Less Active Cascade Catalyst to Produce More C2+ Products in Electrochemical CO2 Reduction*. The Journal of Physical Chemistry C 2023, 127, 289-299.
(9) Wordsworth, J.; Benedetti, T. M.; Somerville, S. V.; Schuhmann, W.; Tilley, R. D.; Gooding, J. J. *The Influence of Nanoconfinement on Electrocatalysis*. Angewandte Chemie International Edition 2022, 61, e202200755.
(10) Dong, B.; Mansour, N.; Pei, Y.; Wang, Z.; Huang, T.; Filbrun, S. L.; Chen, M.; Cheng, X.; Pruski, M.; Huang, W.; Fang, N. *Single Molecule Investigation of Nanoconfinement Hydrophobicity in Heterogeneous Catalysis*. Journal of the American Chemical Society 2020, 142, 13305-13309.
(11) Ballester, P. *Effects of Nanoconfinement on Catalysis. Edited by Rinaldo Poli*. Angewandte Chemie International Edition 2017, 56, 7713-7714.
(12) Fichtner, M. *Nanoconfinement effects in energy storage materials*. Physical Chemistry Chemical Physics 2011, 13, 21186-21195.
(13) Nielsen, T. K.; Besenbacher, F.; Jensen, T. R. *Nanoconfined hydrides for energy storage*. Nanoscale 2011, 3, 2086-2098.
(14) Comanescu, C. *Recent Development in Nanoconfined Hydrides for Energy Storage*. International journal of molecular sciences 2022, 23.
(15) Le, T. T.; Pistidda, C.; Nguyen, V. H.; Singh, P.; Raizada, P.; Klassen, T.; Dornheim, M. *Nanoconfinement effects on hydrogen storage properties of MgH2 and LiBH4*. International Journal of Hydrogen Energy 2021, 46, 23723-23736.
(16) Zhang, Q.; Lei, D.; Shi, J.; Ren, Z.; Yin, J.; Jia, P.; Lu, W.; Gao, Y.; Liu, N. *Pressure-Regulated Nanoconfined Channels for Highly Effective Mechanical–Electrical Conversion in Proton Battery-Type Self-Powered Pressure Sensor*. Advanced Materials 2023, 35, 2308795.

(17) Bian, Y.; Liu, K.; Ran, Y.; Li, Y.; Gao, Y.; Zhao, Z.; Shao, M.; Liu, Y.; Kuang, J.; Zhu, Z.; Qin, M.; Pan, Z.; Zhu, M.; Wang, C.; Chen, H.; Li, J.; Li, X.; Liu, Y.; Guo, Y. *Spatially nanoconfined N-type polymer semiconductors for stretchable ultrasensitive X-ray detection*. Nature Communications 2022, 13, 7163.
(18) Khatri, S.; Pandey, P.; Mejia, G.; Ghimire, G.; Leng, F.; He, J. *Nanoconfinement and Crowding Enhanced Single-Molecule Detection of Small Molecules with Nanopipettes*. Journal of the American Chemical Society 2023, 145, 28075-28084.
(19) Yu, R.-J.; Xu, S.-W.; Paul, S.; Ying, Y.-L.; Cui, L.-F.; Daiguji, H.; Hsu, W.-L.; Long, Y.-T. *Nanoconfined Electrochemical Sensing of Single Silver Nanoparticles with a Wireless Nanopore Electrode*. ACS Sensors 2021, 6, 335-339.
(20) Qian, J.; Gao, X.; Pan, B. *Nanoconfinement-Mediated Water Treatment: From Fundamental to Application*. Environmental Science & Technology 2020, 54, 8509-8526.
(21) Ly, Q. V.; Cui, L.; Asif, M. B.; Khan, W.; Nghiem, L. D.; Hwang, Y.; Zhang, Z. *Membrane-based nanoconfined heterogeneous catalysis for water purification: A critical review☆*. Water Research 2023, 230, 119577.
(22) Liu, T.; Xiao, S.; Li, N.; Chen, J.; Zhou, X.; Qian, Y.; Huang, C.-H.; Zhang, Y. *Water decontamination via nonradical process by nanoconfined Fenton-like catalysts*. Nature Communications 2023, 14, 2881.
(23) Meng, C.; Ding, B.; Zhang, S.; Cui, L.; Ostrikov, K. K.; Huang, Z.; Yang, B.; Kim, J.-H.; Zhang, Z. *Angstrom-confined catalytic water purification within Co-TiOx laminar membrane nanochannels*. Nature Communications 2022, 13, 4010.
(24) Nguyen, T. D. T.; Pitchaimani, A.; Ferrel, C.; Thakkar, R.; Aryal, S. *Nano-confinement-driven enhanced magnetic relaxivity of SPIONs for targeted tumor bioimaging*. Nanoscale 2018, 10, 284-294.
(25) Malzahn, K.; Ebert, S.; Schlegel, I.; Neudert, O.; Wagner, M.; Schütz, G.; Ide, A.; Roohi, F.; Münnemann, K.; Crespy, D.; Landfester, K. *Design and Control of Nanoconfinement to Achieve Magnetic Resonance Contrast Agents with High Relaxivity*. Advanced Healthcare Materials 2016, 5, 567-574.
(26) Kang, C.; Kim, D. *Nanoconfinement-mediated cancer theranostics*. Archives of pharmacal research 2020, 43, 110-117.
(27) Yoo, E.; Choi, J. H.; Hoang, N. H.; Lee, J. S.; Vuong, S.; Hur, B.; Han, P.; Oh, K. T.; Fahmy, T.; Kim, D. *Particle-in-Particle Platform for Nanoconfinement-Induced Oncothermia*. ACS applied bio materials 2018, 1, 1927-1941.
(28) Shafiee, O.; Jenkins, S. G.; Ito, T.; Higgins, D. A. *Diffusion of hydrophilic to hydrophobic forms of Nile red in aqueous C12EO10 gels by variable area fluorescence correlation spectroscopy*. Physical Chemistry Chemical Physics 2023, 25, 2853-2861.
(29) Bandegi, A.; Marquez Garcia, M.; Bañuelos, J. L.; Firestone, M. A.; Foudazi, R. *Soft nanoconfinement of ionic liquids in lyotropic liquid crystals*. Soft Matter 2021, 17, 8118-8129.
(30) Zhang, R.; Zeng, X.; Kim, B.; Bushby, R. J.; Shin, K.; Baker, P. J.; Percec, V.; Leowanawat, P.; Ungar, G. *Columnar Liquid Crystals in Cylindrical Nanoconfinement*. ACS Nano 2015, 9, 1759-1766.
(31) Rashidi, H.; Howard, K. J.; Ito, T.; Higgins, D. A. *Random Walks and Sticky Surfaces: Single-Molecule Measurements of Solute Diffusion in Ethanol/Water-Filled Anodic Alumina Nanopores*. The Journal of Physical Chemistry C 2023, 127, 411-420.

(32) Koone, N.; Shao, Y.; Zerda, T. W. *Diffusion of Simple Liquids in Porous Sol-Gel Glass*. The Journal of Physical Chemistry 1995, 99, 16976-16981.
(33) Thompson, W. H. *Solvation Dynamics and Proton Transfer in Nanoconfined Liquids*. Annu. Rev. Phys. Chem. 2011, 62, 599-619.
(34) Reinitzer, F. *Beiträge zur Kenntniss des Cholesterins*. Monatshefte für Chemie und verwandte Teile anderer Wissenschaften 1888, 9, 421-441.
(35) Bisoyi, H. K.; Li, Q. *Liquid Crystals: Versatile Self-Organized Smart Soft Materials*. Chemical Reviews 2022, 122, 4887-4926.
(36) Kumar, S.; Kang, S. W.: *Liquid Crystals*. In *Encyclopedia of Condensed Matter Physics*; Bassani, F., Liedl, G. L., Wyder, P., Eds.; Elsevier: Oxford, 2005; pp 111-120.
(37) Yang, D. K.; Wu, S. T.: *Fundamentals of Liquid Crystal Devices*; Wiley, 2014.
(38) Dierking, I.; Al-Zangana, S. *Lyotropic Liquid Crystal Phases from Anisotropic Nanomaterials*. Nanomaterials 2017, 7, 305.
(39) Mitchell, D. J.; Tiddy, G. J. T.; Waring, L.; Bostock, T.; McDonald, M. P. *Phase Behaviour of Polyoxyethylene Surfactants with Water*. J. Chem. Soc. Farad. Trans. 1 1983, 79, 975-1000.
(40) Dong, R.; Hao, J. *Complex Fluids of Poly(oxyethylene) Monoalkyl Ether Nonionic Surfactants*. Chem. Rev. 2010, 110, 4978-5022.
(41) Topuzlu, E. Y. *investigation on lithium salt - surfactant lyotropic liquid crystalline mesophases: characterization, role of water, and electrochemical behaviors*. BILKENT UNIVERSITY, 2021.
(42) https://www.inredox.com/technology/anodic-aluminum-oxide/.
(43) Amobonye, A. E.; Aruwa, C. E.; Pillai, S.: *Chapter 8 - Biodegradability and current status of polyethylene terephthalate*. In *Biodegradability of Conventional Plastics*; Sarkar, A., Sharma, B., Shekhar, S., Eds.; Elsevier, 2023; pp 155-177.
(44) Crawford, C. B.; Quinn, B.: *4 - Physiochemical properties and degradation*. In *Microplastic Pollutants*; Crawford, C. B., Quinn, B., Eds.; Elsevier, 2017; pp 57-100.
(45) Robertson, G. L.: *Food Packaging*. In *Encyclopedia of Agriculture and Food Systems*; Van Alfen, N. K., Ed.; Academic Press: Oxford, 2014; pp 232-249.
(46) Sin, L. T.; Tueen, B. S.: *2 - Eco-profile of plastics*. In *Plastics and Sustainability*; Sin, L. T., Tueen, B. S., Eds.; Elsevier, 2023; pp 45-89.
(47) Sin, L. T.; Tueen, B. S.: *1 - Plastics and environmental sustainability issues*. In *Plastics and Sustainability*; Sin, L. T., Tueen, B. S., Eds.; Elsevier, 2023; pp 1-43.
(48) Paladhi, A. G.; Vallinayagam, S.; Rajendran, S.; Rathinam, V.; Sharma, V. K.: *Chapter 30 - Microalgae: a promising tool for plastic degradation*. In *Microbes and Microbial Biotechnology for Green Remediation*; Malik, J. A., Ed.; Elsevier, 2022; pp 575-587.
(49) Hamid Rahidi, O. S., Daniel A. Higgins.: *Fluorescence Correlation Spectroscopy Studies of Dye Diffusion on Fresh and Aged Post-Consumer Polyethylene Terephthalate*. 2023.
(50) Jose, J.; Burgess, K. *Syntheses and Properties of Water-Soluble Nile Red Derivatives*. The Journal of Organic Chemistry 2006, 71, 7835-7839.
(51) Martinez, V.; Henary, M. *Nile Red and Nile Blue: Applications and Syntheses of Structural Analogues*. Chemistry (Weinheim an der Bergstrasse, Germany) 2016, 22, 13764-13782.
(52) Golini, C. M.; Williams, B. W.; Foresman, J. B. *Further Solvatochromic, Thermochromic, and Theoretical Studies on Nile Red*. Journal of Fluorescence 1998, 8, 395-404.

(53) Marini, A.; Muñoz-Losa, A.; Biancardi, A.; Mennucci, B. *What is Solvatochromism?* The Journal of Physical Chemistry B 2010, 114, 17128-17135.
(54) *Solvent Effects on Fluorescence Emission*. http://molecularexpressions.com/.
(55) Tahir, H.; Saad, M.: *Chapter 3 - Using dyes to evaluate the photocatalytic activity*. In *Interface Science and Technology*; Ghaedi, M., Ed.; Elsevier, 2021; Vol. 32; pp 125-224.
(56) Lucotti, A.; Villa, N. S.; Serra, G.; Maria Ossi, P.; Tommasini, M.: *Chapter 7 - Thin-layer chromatography–surface-enhanced Raman scattering*. In *Molecular and Laser Spectroscopy*; Gupta, V. P., Ed.; Elsevier, 2022; pp 249-277.
(57) Harris, D. C.; Lucy, C. A.: *Quantitative Chemical Analysis*; W. H. Freeman: Austin, TX, 2020.
(58) *Introduction to Fluorescence Correlation Spectroscopy*. https://www.tcspc.com/doku.php/general:fluorescence_correlation_spectroscopy-_a_short_introduction.
(59) Sommer, M. E.; Elgeti, M.; Hildebrand, P. W.; Szczepek, M.; Hofmann, K. P.; Scheerer, P.: *Chapter Twenty-Six - Structure-Based Biophysical Analysis of the Interaction of Rhodopsin with G Protein and Arrestin*. In *Methods in enzymology*; Shukla, A. K., Ed.; Academic Press, 2015; Vol. 556; pp 563-608.
(60) Kubin, R. F.; Fletcher, A. N. *Fluorescence quantum yields of some rhodamine dyes*. Journal of Luminescence 1982, 27, 455-462.
(61) Schwille, P.; Haustein, E. *Fluorescence Correlation Spectroscopy - An Introduction to its Concepts and Applications*. Spectroscopy 2001, 94(22).
(62) Ries, J.; Schwille, P. *Fluorescence correlation spectroscopy*. BioEssays 2012, 34, 361-368.
(63) *FCS classroom*. https://www.fcsxpert.com/classroom/theory/what-is-confocal-volume.html.
(64) Higgins, D. A. *Chemical microscopy, Kansas State University, CHM940,* 2019.
(65) Busch, K. W.; Busch, M. A.: *Chapter 3 - Light Polarization and Signal Processing in Chiroptical Instrumentation*. In *Chiral Analysis (Second Edition)*; Polavarapu, P. L., Ed.; Elsevier, 2018; pp 73-151.
(66) Paschotta, R.: *Dichroic Mirrors*. In RP Photonics Encyclopedia.
(67) Rottenfusser, R.: *Chapter 3 - Proper Alignment of the Microscope*. In *Methods in Cell Biology*; Sluder, G., Wolf, D. E., Eds.; Academic Press, 2013; Vol. 114; pp 43-67.
(68) *Understanding Microscopes and Objectives*. https://www.edmundoptics.com/knowledge-center/application-notes/microscopy/understanding-microscopes-and-objectives/#.
(69) S, R. *Confocal microscopy and quantitative single molecule techniques for metrology in molecular medicine*. 2007.
(70) Šachl, R.; Bergstrand, J.; Widengren, J.; Hof, M. *Fluorescence correlation spectroscopy diffusion laws in the presence of moving nanodomains*. Journal of Physics D: Applied Physics 2016, 49, 114002.
(71) Veerapathiran, S.; Wohland, T. *The Imaging FCS Diffusion Law in the Prescence of Multiple Diffusive Modes*. Methods 2018, 140-141, 140-150.
(72) Gupta, A.; Phang, I. Y.; Wohland, T. *To Hop of Not to Hop: Exceptions in the FCS Diffusion Law*. Biophys. J. 2020, 118, 2434-2447.
(73) Wawrezinieck, L.; Rigneault, H.; Marguet, D.; Lenne, P.-F. *Fluorescence Correlation Spectroscopy Diffusion Laws to Probe the Submicron Cell Membrane Organization*. Biophys. J. 2005, 89, 4029-4042.

(74) Masuda, A.; Ushida, K.; Okamoto, T. *New Fluorescence Correlation Spectroscopy Enabling Direct Observation of Spatiotemporal Dependence of Diffusion Constants as an Evidence of Anomalous Transport in Extracellular Matrices*. Biophys. J. 2005, 88, 3584-3591.
(75) Skoog, D. A.; West, D. M.; Holler, F. J.; Crouch, S. R.: *Fundamentals of Analytical Chemistry*; Cengage Learning, 2021.
(76) Aswani, K.; Jinadasa, T.; Brown, C. M. *Fluorescence Microscopy Light Sources*. Microscopy Today 2012, 20, 22-28.
(77) Harris, D. C.; Lucy, C. A.; University of North Carolina at Chapel Hill. Department of, C.: *Quantitative chemical analysis*; Ninth edition. ed.; Freeman Custom Publishing: New York, NY, 2016. pp. xviii, 750 pages, various pagings : illustrations ; 28 cm.
(78) Wolverson, D.: *8 - Raman spectroscopy*. In *Characterization of Semiconductor Heterostructures and Nanostructures*; Lamberti, C., Ed.; Elsevier: Amsterdam, 2008; pp 249-288.
(79) Raja, P. M. V.; Barron, A. R. *Raman Spectroscopy*.
(80) Romero, G.; Rojas, E.; Estrela-Lopis, I.; Donath, E.; Moya, S. E. *Spontaneous confocal Raman microscopy--a tool to study the uptake of nanoparticles and carbon nanotubes into cells*. Nanoscale Research Letters 2011, 6, 429.
(81) Romero, G.; Estrela-Lopis, I.; Zhou, J.; Rojas, E.; Franco, A.; Espinel, C. S.; Fernández, A. G.; Gao, C.; Donath, E.; Moya, S. E. *Surface Engineered Poly(lactide-co-glycolide) Nanoparticles for Intracellular Delivery: Uptake and Cytotoxicity—A Confocal Raman Microscopic Study*. Biomacromolecules 2010, 11, 2993-2999.
(82) Puppels, G. J.; de Mul, F. F. M.; Otto, C.; Greve, J.; Robert-Nicoud, M.; Arndt-Jovin, D. J.; Jovin, T. M. *Studying single living cells and chromosomes by confocal Raman microspectroscopy*. Nature 1990, 347, 301-303.
(83) Uzunbajakava, N.; Lenferink, A.; Kraan, Y.; Willekens, B.; Vrensen, G.; Greve, J.; Otto, C. *Nonresonant Raman imaging of protein distribution in single human cells*. Biopolymers 2003, 72, 1-9.
(84) *Applications and Specifics of SAXS*. In *Small-Angle Scattering*, 2021; pp 137-195.
(85) Kikhney, A. G.; Svergun, D. I. *A practical guide to small angle X-ray scattering (SAXS) of flexible and intrinsically disordered proteins*. FEBS Letters 2015, 589, 2570-2577.
(86) Petukhov, A. V.; Meijer, J.-M.; Vroege, G. J. *Particle shape effects in colloidal crystals and colloidal liquid crystals: Small-angle X-ray scattering studies with microradian resolution*. Current Opinion in Colloid & Interface Science 2015, 20, 272-281.
(87) Hiltner, P. A.; Krieger, I. M. *Diffraction of light by ordered suspensions*. The Journal of Physical Chemistry 1969, 73, 2386-2389.
(88) Kipkemboi, P.; Khan, A.; Lindman, B.; Alfredsson, V. *Phase behaviour and structure of amphiphilic poly(ethylene oxide)-poly(propylene oxide) triblock copolymers ((EO)4(PO)59(EO)4 and (EO)17(PO)59(EO)17) in ternary mixtures with water and xylene*. Canadian Journal of Chemistry 2011, 81, 897-908.
(89) Chow, T. S. *Wetting of rough surfaces*. Journal of Physics: Condensed Matter 1998, 10, L445.
(90) Ponomar, M.; Krasnyuk, E.; Butylskii, D.; Nikonenko, V.; Wang, Y.; Jiang, C.; Xu, T.; Pismenskaya, N. *Sessile Drop Method: Critical Analysis and Optimization for Measuring the Contact Angle of an Ion-Exchange Membrane Surface*. Membranes 2022, 12, 765.

(91) Eaton, P. J.; West, P.: *Atomic force microscopy*; Oxford University Press: Oxford, 2018. pp. viii, 248 pages, 4 unnumbered pages of plates : illustrations (some color) ; 25 cm.

(92) Bullen, R. A. W. a. H. A. *Introduction to Scanning Probe Microscopy (SPM), Basic Theory, Atomic Force Microscopy (AFM)*2006.

(93) Seliktar, D. *Designing cell-compatible hydrogels for biomedical applications*. Science 2012, 336, 1124-1128.

(94) Elstad, N. L.; Fowers, K. D. *OncoGel (ReGel/paclitaxel)--clinical applications for a novel paclitaxel delivery system*. Advanced drug delivery reviews 2009, 61, 785-794.

(95) Escobar-Chavez, J. J.; Lopez-Cervantes, M.; Naik, A.; Kalia, Y. N.; Quintanar-Guerrero, D.; Ganem-Quintanar, A. *Applications of Thermoreversible Pluronic F-127 Gels in Pharmaceutical Formulations*. J. Pharm. Pharmaceut. Sci. 2006, 9, 339-358.

(96) Zhou, M.; Kidd, T. J.; Noble, R. D.; Gin, D. L. *Supported Lyotropic Liquid-Crystal Polymer Membranes: Promising Materials for Molecular-Size -Selective Aqueous Nanofiltration*. Adv. Mater. 2005, 17, 1850-1853.

(97) Ulbricht, M. *Advanced Functional Polymer Membranes*. Polymer 2006, 47, 2217-2262.

(98) Dellinger, T. M.; Braun, P. V. *Lyotropic Liquid Crystals as Nanoreactors for Nanoparticle Synthesis*. Chemistry of Materials 2004, 16, 2201-2207.

(99) Wang, C.; Chen, D.; Jiao, X. *Lyotropic liquid crystal directed synthesis of nanostructured materials*. Science and technology of advanced materials 2009, 10, 023001.

(100) Constantin, D.; Oswald, P.; Imperor-Clerc, M.; Davidson, P.; Sotta, P. *Connectivity of the Hexagonal, Cubic, and Isotropic Phases of the C12EO6/H2O Lyotropic Mixture Investigated by Tracer Diffusion and X-ray Scattering*. J. Phys. Chem. B 2001, 105, 668-673.

(101) Sakya, P.; Seddon, J. M.; Templer, R. H.; Mirkin, R. J.; Tiddy, G. J. T. *Micellar Cubic Phases and Their Structural Relationships: The Nonionic Surfactant System C12EO12/Water*. Langmuir 1997, 13, 3706-3714.

(102) Padia, F. N.; Yaseen, M.; Gore, B.; Rogers, S.; Bell, G.; Lu, J. R. *Influence of molecular structure on the size, shape, and nanostructure of nonionic C(n)E(m) surfactant micelles*. The journal of physical chemistry. B 2014, 118, 179-188.

(103) Zulauf, M.; Weckstrom, K.; Hayter, J. B.; Degiorgio, V.; Corti, M. *Neutron Scattering Study of Micelle Structure in Iostropic Aqueous Solutions of Poly(oxyethylene) Amphiphiles*. J. Phys. Chem. 1985, 89, 3411-3417.

(104) Lin, Z.; Scriven, L. E.; Davis, H. T. *Cryogenic electron microscopy of rodlike or wormlike micelles in aqueous solutions of nonionic surfactant hexaethylene glycol monohexadecyl ether*. Langmuir 1992, 8, 2200-2205.

(105) Bernheim-Groswasser, A.; Wachtel, E.; Talmon, Y. *Micellar Growth, Network Formation, and Criticality in Aqueous Solutions of the Nonionic Surfactant C12E5*. Langmuir 2000, 16, 4131-4140.

(106) Johansson, L.; Hedberg, P.; Loefroth, J. E. *Diffusion and interaction in gels and solution. 5. Nonionic micellar systems*. The Journal of Physical Chemistry 1993, 97, 747-755.

(107) Alexander, N. P.; Phillips, R. J.; Dungan, S. R. *Multicomponent Diffusion in Aqueous Solutions of Nonionic Micelles and Decane*. Langmuir 2019, 35, 13595-13606.

(108) Alexander, N. P.; Phillips, R. J.; Dungan, S. R. *Multicomponent diffusion of interacting, nonionic micelles with hydrophobic solutes*. Soft Matter 2021, 17, 531-542.

(109) Yethiraj, A.; Capitani, D.; Burlinson, N. E.; Burnell, E. E. *An NMR Study of Translational Diffusion and Structural Anisotropy in Magnetically Aliged Nonionic Surfactant Mesophases*. Langmuir 2005, 21, 3311-3321.
(110) Gaemers, S.; Bax, A. *Morphology of three lyotropic liquid crystalline biological NMR media studied by translational diffusion anisotropy*. J Am Chem Soc 2001, 123, 12343-12352.
(111) Elson, E. L.; Magde, D. *Fluorescecne Correlation Spectroscopy. I. Conceptual Basis and Theory*. Biopolymers 1974, 13, 1-27.
(112) Magde, D.; Elson, E. L.; Webb, W. W. *THermodynamic Fluctuations in a Reacting System-Measurement by Fluorescence Correlation Spectroscopy*. Phys. Rev. Lett. 1972, 29, 705-708.
(113) Aragon, S. R.; Pecora, R. *Fluorescence Correlation Spectroscopy as a Probe of Molecular Dynamics*. J. Chem. Phys. 1976, 64, 1791-1803.
(114) Hess, S. T.; Huang, S.; Heikal, A. A.; Webb, W. W. *Biological and Chemical Applications of Fluorescence Correlation Spectroscopy: A Review*. Biochemistry 2002, 41, 697-705.
(115) Elson, E. L. *Fluorescence Correlation Spectroscopy: Past, Present, Future*. Biophys. J. 2011, 101, 2855-2870.
(116) Koynov, K.; Butt, H.-J. *Fluorescence correlation spectroscopy in colloid and interface science*. Current Opinion in Colloid & Interface Science 2012, 17, 377-387.
(117) Wöll, D. *Fluorescence correlation spectroscopy in polymer science*. RSC Advances 2014, 4, 2447-2465.
(118) Hungerford, G.; Castanheira, E. M. S.; Real Oliveira, M. E. C. D.; da Graça Miguel, M.; Burrows, H. D. *Monitoring Ternary Systems of C12E5/Water/Tetradecane via the Fluorescence of Solvatochromic Probes*. The Journal of Physical Chemistry B 2002, 106, 4061-4069.
(119) Stuart, M. C. A.; van de Pas, J. C.; Engberts, J. B. F. N. *The use of Nile Red to monitor the aggregation behavior in ternary surfactant–water–organic solvent systems*. Journal of Physical Organic Chemistry 2005, 18, 929-934.
(120) Dong, R.; Hao, J. *Complex Fluids of Poly(oxyethylene) Monoalkyl Ether Nonionic Surfactants*. Chemical Reviews 2010, 110, 4978-5022.
(121) Martin-Brown, S. A.; Fu, Y.; Saroja, G.; Collinson, M. M.; Higgins, D. A. *Single Molecule Studies of Diffusion by Oligomer-Bound Dyes in Organically-Modified Sol-Gel-Derived Silicate Films*. Anal. Chem. 2005, 77, 486-494.
(122) Briggs, M. S. J.; Bruce, I.; Miller, J. N.; Moody, C. J.; Simmonds, A. C.; Swann, E. *Synthesis of Functionalised Fluorescent Dyes and Their Coupling to Amines and Amino Acids*. J. Chem. Soc. Perkin Trans. 1 1997, 1051-1058.
(123) Kucherak, O. A.; Oncul, S.; Darwich, Z.; Yushchenko, D. A.; Arntz, Y.; Didier, P.; Mély, Y.; Klymchenko, A. S. *Switchable Nile Red-Based Probe for Cholesterol and Lipid Order at the Outer Leaflet of Biomembranes*. J. Am. Chem. Soc. 2010, 132, 4907-4916.
(124) Lange, J. J.; Culbertson, C. T.; Higgins, D. A. *Single molecule studies of solvent-dependent diffusion and entrapment in poly(dimethylsiloxane) thin films*. Anal Chem 2008, 80, 9726-9734.
(125) Kirkeminde, A. W.; Torres, T.; Ito, T.; Higgins, D. A. *Multiple Diffusion Pathways in Pluronic F127 Mesophases Revealed by Single Molecule Tracking and Fluorescence Correlation Spectroscopy*. J. Phys. Chem. B 2011, 115, 12736-12743.

(126) Kisley, L.; Brunetti, R.; Tauzin, L. J.; Shuang, B.; Yi, X.; Kirkeminde, A. W.; Higgins, D. A.; Weiss, S.; Landes, C. F. *Characterization of Porous Materials by Fluorescence Correlation Spectroscopy Super-Resolution Optical Fluctuation Imaging*. ACS Nano 2015, 9, 9158-9166.
(127) Enderlein, J.; Gregor, I.; Patra, D.; Fitter, J. *Art and Artefacts of Fluorescence Correlation Spectroscopy*. Current Pharmaceutical Biotechnology 2004, 5, 155-161.
(128) Enderlein, J.; Gregor, I.; Patra, D.; Dertinger, T.; Kaupp, U. B. *Performance of Fluorescence Correlation Spectroscopy for Measuring Diffusion and Concentration*. ChemPhysChem 2005, 6, 2324-2336.
(129) Banachowicz, E.; Patkowski, A.; Meier, G.; Klamecka, K.; Gapinski, J. *Successful FCS Experiment in Nonstandard Conditions*. Langmuir 2014, 30, 8945-8955.
(130) Molteni, M.; Ferri, F. *Commercial counterboard for 10 ns software correlator for photon and fluorescence correlation spectroscopy*. Review of Scientific Instruments 2016, 87.
(131) Hamley, I. W.; Castelletto, V. *Small-angle scattering of block copolymers: in the melt, solution and crystal states*. Progress in Polymer Science 2004, 29, 909-948.
(132) Berthod, A.; Tomer, S.; Dorsey, J. G. *Polyoxyethylene alkyl ether nonionic surfactants: physicochemical properties and use for cholesterol determination in food*. Talanta 2001, 55, 69-83.
(133) Giri, D.; Hanks, C. N.; Collinson, M. M.; Higgins, D. A. *Single-Molecule Spectroscopic Imaging Studies of Polarity Gradients Prepared by Infusion-Withdrawal Dip-Coating*. J. Phys. Chem. C 2014, 118, 6423-6432.
(134) Widengren, J.; Mets, U.; Rigler, R. *Fluorescence correlation spectroscopy of triplet states in solution: a theoretical and experimental study*. The Journal of Physical Chemistry 1995, 99, 13368-13379.
(135) Culbertson, M. J.; Williams, J. T. B.; Cheng, W. W. L.; Stults, D. A.; Wiebracht, E. R.; Kasianowicz, J. J.; Burden, D. L. *Numerical Fluorescence Correlation Spectroscopy for the Analysis of Molecular Dynamics under Nonstandard Conditions*. Anal. Chem. 2007, 79, 4031-4039.
(136) Gendron, P.-O.; Avaltroni, F.; Wilkinson, K. J. *Diffusion Coefficients of Several Rhodamine Derivatives as Determined by Pulsed Field Gradient-Nuclear Magnetic Resonance and Fluorescence Correlation Spectroscopy*. J. Fluoresc. 2008, 18, 1093-1101.
(137) Bag, N.; Ng, X. W.; Sankaran, J.; Wohland, T. *Spatiotemporal mapping of diffusion dynamics and organization in plasma membranes*. Methods and Applications in Fluorescence 2016, 4, 034003.
(138) Veerapathiran, S.; Wohland, T. *The Imaging FCS Diffusion Law in the Presence of Multiple Diffusive Modes*. Methods 2018, 140-141, 140-150.
(139) Milliken, G. A.; Johnson, D. E.: *Analysis of Messy Data, Volume III: Analysis of Covariance*; Chapman & Hall/CRC Press: Boca Raton, FL, 2002.
(140) Williams, A. T.; Rangel-Buitrago, N. *The past, present, and future of plastic pollution*. Marine Pollution Bulletin 2022, 176, 113429.
(141) Alimi, O. S.; Farner Budarz, J.; Hernandez, L. M.; Tufenkji, N. *Microplastics and Nanoplastics in Aquatic Environments: Aggregation, Deposition, and Enhanced Contaminant Transport*. Environmental Science & Technology 2018, 52, 1704-1724.
(142) Yu, Q.; Hu, X.; Yang, B.; Zhang, G.; Wang, J.; Ling, W. *Distribution, abundance and risks of microplastics in the environment*. Chemosphere 2020, 249, 126059.

(143) Richardson, S. D.; Kimura, S. Y. *Water Analysis: Emerging Contaminants and Current Issues*. Analytical Chemistry 2016, 88, 546-582.
(144) Frias, J. P. G. L.; Nash, R. *Microplastics: Finding a consensus on the definition*. Marine Pollution Bulletin 2019, 138, 145-147.
(145) Sapea, A. *Scientific perspective on microplastics in nature and society*. Science Advice for Policy by European Academies, Berlin 2019.
(146) Yu, F.; Yang, C.; Zhu, Z.; Bai, X.; Ma, J. *Adsorption behavior of organic pollutants and metals on micro/nanoplastics in the aquatic environment*. Science of The Total Environment 2019, 694, 133643.
(147) Costigan, E.; Collins, A.; Hatinoglu, M. D.; Bhagat, K.; MacRae, J.; Perreault, F.; Apul, O. *Adsorption of organic pollutants by microplastics: Overview of a dissonant literature*. Journal of Hazardous Materials Advances 2022, 6, 100091.
(148) Kwon, J. H.; Chang, S.; Hong, S. H.; Shim, W. J. *Microplastics as a vector of hydrophobic contaminants: Importance of hydrophobic additives*. Integrated environmental assessment and management 2017, 13, 494-499.
(149) Verla, A. W.; Enyoh, C. E.; Verla, E. N.; Nwarnorh, K. O. *Microplastic–toxic chemical interaction: a review study on quantified levels, mechanism and implication*. SN Applied Sciences 2019, 1, 1-30.
(150) Endo, S.; Takizawa, R.; Okuda, K.; Takada, H.; Chiba, K.; Kanehiro, H.; Ogi, H.; Yamashita, R.; Date, T. *Concentration of polychlorinated biphenyls (PCBs) in beached resin pellets: variability among individual particles and regional differences*. Marine pollution bulletin 2005, 50, 1103-1114.
(151) Andrady, A. L. *Microplastics in the marine environment*. Marine pollution bulletin 2011, 62, 1596-1605.
(152) Du, H.; Zhang, Y.; Jiang, H.; Wang, H. *Adsorption of rhodamine B on polyvinyl chloride, polystyrene, and polyethylene terephthalate microplastics in aqueous environments*. Environmental Technology & Innovation 2022, 27, 102495.
(153) Lee, H.; Shim, W. J.; Kwon, J.-H. *Sorption capacity of plastic debris for hydrophobic organic chemicals*. Science of The Total Environment 2014, 470-471, 1545-1552.
(154) Wu, C.; Zhang, K.; Huang, X.; Liu, J. *Sorption of pharmaceuticals and personal care products to polyethylene debris*. Environmental Science and Pollution Research 2016, 23, 8819-8826.
(155) Goedecke, C.; Mülow-Stollin, U.; Hering, S.; Richter, J.; Piechotta, C.; Paul, A.; Braun, U. *A First Pilot Study on the Sorption of Environmental Pollutants on Various Microplastic Materials*. Journal of environmental analytical chemistry 2017, 4, 1-8.
(156) Seidensticker, S.; Zarfl, C.; Cirpka, O. A.; Grathwohl, P. *Microplastic–Contaminant Interactions: Influence of nonlinearity and coupled mass transfer*. Environmental toxicology and chemistry 2019, 38, 1635-1644.
(157) Hüffer, T.; Hofmann, T. *Sorption of non-polar organic compounds by micro-sized plastic particles in aqueous solution*. Environmental pollution 2016, 214, 194-201.
(158) Al Harraq, A.; Brahana, P. J.; Arcemont, O.; Zhang, D.; Valsaraj, K. T.; Bharti, B. *Effects of Weathering on Microplastic Dispersibility and Pollutant Uptake Capacity*. ACS environmental Au 2022, 2, 549-555.
(159) Bhagat, K.; Barrios, A. C.; Rajwade, K.; Kumar, A.; Oswald, J.; Apul, O.; Perreault, F. *Aging of microplastics increases their adsorption affinity towards organic contaminants*. Chemosphere 2022, 298, 134238.

(160) Hankett, J. M.; Collin, W. R.; Yang, P.; Chen, Z.; Duhaime, M. *Low-volatility model demonstrates humidity affects environmental toxin deposition on plastics at a molecular level*. Environmental Science & Technology 2016, 50, 1304-1312.
(161) Wang, W.; Wang, J. *Different partition of polycyclic aromatic hydrocarbon on environmental particulates in freshwater: microplastics in comparison to natural sediment*. Ecotoxicology and environmental safety 2018, 147, 648-655.
(162) Llorca, M.; Schirinzi, G.; Martínez, M.; Barceló, D.; Farré, M. *Adsorption of perfluoroalkyl substances on microplastics under environmental conditions*. Environmental pollution 2018, 235, 680-691.
(163) Shim, W. J.; Song, Y. K.; Hong, S. H.; Jang, M. *Identification and quantification of microplastics using Nile Red staining*. Marine pollution bulletin 2016, 113, 469-476.
(164) Maes, T.; Jessop, R.; Wellner, N.; Haupt, K.; Mayes, A. G. *A rapid-screening approach to detect and quantify microplastics based on fluorescent tagging with Nile Red*. Scientific reports 2017, 7, 44501.
(165) Erni-Cassola, G.; Gibson, M. I.; Thompson, R. C.; Christie-Oleza, J. A. *Lost, but Found with Nile Red: A Novel Method for Detecting and Quantifying Small Microplastics (1 mm to 20 μm) in Environmental Samples*. Environmental Science & Technology 2017, 51, 13641-13648.
(166) Vasseghian, Y.; Hosseinzadeh, S.; Khataee, A.; Dragoi, E.-N. *The concentration of persistent organic pollutants in water resources: A global systematic review, meta-analysis and probabilistic risk assessment*. Science of The Total Environment 2021, 796, 149000.
(167) Tsironi, T. N.; Chatzidakis, S. M.; Stoforos, N. G. *The future of polyethylene terephthalate bottles: Challenges and sustainability*. Packaging Technology and Science 2022, 35, 317-325.
(168) Baird, C.; Cann, M.: *Environmental chemistry*; Macmillan, 2005.
(169) Giri, D.; Ashraf, K. M.; Collinson, M. M.; Higgins, D. A. *A Single Molecule Perspective on Mass Transport in Condensed Water Layers over Gradient Self-Assembled Monolayers*. J. Phys. Chem. C 2015, 119, 9418-9428.
(170) Stalder, A. F.; Melchior, T.; Müller, M.; Sage, D.; Blu, T.; Unser, M. *Low-bond axisymmetric drop shape analysis for surface tension and contact angle measurements of sessile drops*. Colloids and Surfaces A: Physicochemical and Engineering Aspects 2010, 364, 72-81.
(171) Stubbins, A.; Law, K. L.; Muñoz, S. E.; Bianchi, T. S.; Zhu, L. *Plastics in the Earth system*. Science 2021, 373, 51-55.
(172) Lin, C.-C.; Krommenhoek, P. J.; Watson, S. S.; Gu, X. *Depth Profiling of Degradation of Multilayer Photovoltaic Backsheets after Accelerated Laboratory Weathering: Cross-sectional Raman Imaging*. Solar Energy Mater. Solar Cell 2016, 144, 289-299.
(173) Liang, C. Y.; Krimm, S. *Infrared Spectra of High Polymers Part IX. Polyethylene Terephthalate*. J. Mol. Spectrosc. 1959, 3, 554-574.
(174) Rebollar, E.; Pérez, S.; Hernández, M.; Domingo, C.; Martín, M.; Ezquerra, T. A.; García-Ruiz, J. P.; Castillejo, M. *Physicochemical modifications accompanying UV laser induced surface structures on poly (ethylene terephthalate) and their effect on adhesion of mesenchymal cells*. Physical Chemistry Chemical Physics 2014, 16, 17551-17559.
(175) Teare, D.; Ton-That, C.; Bradley, R. *Surface characterization and ageing of ultraviolet–ozone-treated polymers using atomic force microscopy and x-ray photoelectron*

spectroscopy. Surface and Interface Analysis: An International Journal devoted to the development and application of techniques for the analysis of surfaces, interfaces and thin films 2000, 29, 276-283.
(176) Gotoh, K.; Kobayashi, Y.; Yasukawa, A.; Ishigami, Y. *Surface modification of PET films by atmospheric pressure plasma exposure with three reactive gas sources*. Colloid and Polymer Science 2012, 290, 1005-1014.
(177) Rozman, U.; Kalčíková, G. *Seeking for a perfect (non-spherical) microplastic particle–the most comprehensive review on microplastic laboratory research*. Journal of hazardous materials 2022, 424, 127529.
(178) Ha, T.; Enderle, T.; Chemla, D.; Selvin, P.; Weiss, S. *Quantum jumps of single molecules at room temperature*. Chemical Physics Letters 1997, 271, 1-5.
(179) Krichevsky, O.; Bonnet, G. *Fluorescence correlation spectroscopy: the technique and its applications*. Reports on Progress in Physics 2002, 65, 251.
(180) Koppel, D. E. *Statistical accuracy in fluorescence correlation spectroscopy*. Physical Review A 1974, 10, 1938.
(181) Ye, F.; Collinson, M. M.; Higgins, D. A. *Molecular orientation and its influence on autocorrelation amplitudes in single-molecule Imaging experiments*. Analytical chemistry 2007, 79, 6465-6472.
(182) Papavinasam, S.: *Chapter 1 - The Oil and Gas Industry*. In *Corrosion Control in the Oil and Gas Industry*; Papavinasam, S., Ed.; Gulf Professional Publishing: Boston, 2014; pp 1-39.
(183) An, Y.; Althaus, S. M.; Liu, H.-H.; Chen, J.-H. *Nuclear magnetic resonance measurement of methane diffusion in organic-rich shales*. Fuel 2019, 247, 160-163.
(184) Loucks, R.; Reed, R. *Scanning-electron-microscope petrographic evidence for distinguishing organic matter pores associated with depositional organic matter versus migrated organic matter in mudrocks*. GCAGS Journal 2014, 3, 51-60.
(185) Loucks, R.; Reed, R.; Ruppel, S.; Hammes, U. *Spectrum of pore types and networks in mudrocks and a descriptive classification for matrix related pores*. AAPG Bulletin 2012, 96, 1071-1098.
(186) Goral, J.; Panja, P.; Deo, M.; Andrew, M.; Linden, S.; Schwarz, J.-O.; Wiegmann, A. *Confinement Effect on Porosity and Permeability of Shales*. Scientific Reports 2020, 10, 49.
(187) Li, J.-B.; Wang, M.; Shao, H.-M.; Li, M.; Liu, L.; Lu, S.-F. *Shale porosity measurement by the saturated oil method: Removing the contribution from oils dissolved in kerogen*. Petroleum Science 2023, 20, 3273-3279.
(188) Pan, S.; Zha, M.; Gao, C.; Qu, J.; Ding, X. *Pore structure and fractal characteristics of organic-rich lacustrine shales of the Kongdian Formation, Cangdong Sag, Bohai Bay Basin*. Frontiers in Earth Science 2021, 9, 1038.
(189) Ma, L.; Slater, T.; Dowey, P. J.; Yue, S.; Rutter, E. H.; Taylor, K. G.; Lee, P. D. *Hierarchical integration of porosity in shales*. Scientific Reports 2018, 8, 11683.
(190) Wang, Y.; Han, X.; Gao, Z.; Jiang, X. *Thermal cracking of the large molecular alcohols in shale oil by experimental study and kinetic modeling*. Journal of Analytical and Applied Pyrolysis 2022, 168, 105749.
(191) Jin, B.; Li, L.; Sun, H.; Zhou, D. In *Tilte*2023: D011S020R002.
(192) Nikam, P. S.; Jagdale, B. S.; Sawant, A. B.; Hasan, M. *Densities and Viscosities of Binary Mixtures of Toluene with Methanol, Ethanol, Propan-1-ol, Butan-1-ol, Pentan-1-*

ol, and 2-Methylpropan-2-ol at (303.15, 308.15, 313.15) K. Journal of Chemical & Engineering Data 2000, 45, 559-563.
(193) Mhanna, R.; Lefort, R.; Noirez, L.; Morineau, D. *Microstructure and concentration fluctuations in alcohol–Toluene and alcohol-Cyclohexane binary liquids: A small angle neutron scattering study*. Journal of Molecular Liquids 2016, 218, 198-207.
(194) Pettersson, A.; Saris, P.; Rosenholm, J. B. *Thermodynamic properties of binary alcohol–hydrocarbon systems*. Journal of the Chemical Society, Faraday Transactions 1: Physical Chemistry in Condensed Phases 1986, 82, 2435-2457.
(195) Klauck, M.; Grenner, A.; Taubert, K.; Martin, A.; Meinhardt, R.; Schmelzer, J. *Vapor−Liquid Equilibria in Binary Systems of Phenol or Cresols + Water, + Toluene, and + Octane and Liquid−Liquid Equilibria in Binary Systems of Cresols + Water*. Industrial & Engineering Chemistry Research 2008, 47, 5119-5126.
(196) Ploetz, E. A.; Smith, P. E. *A Kirkwood–Buff force field for the aromatic amino acids*. Physical Chemistry Chemical Physics 2011, 13, 18154-18167.
(197) Ploetz, E. A.; Bentenitis, N.; Smith, P. E. *Developing Force Fields from the Microscopic Structure of Solutions*. Fluid phase equilibria 2010, 290, 43.
(198) Abdel Hamid, A. R.; Lefort, R.; Lechaux, Y.; Moréac, A.; Ghoufi, A.; Alba-Simionesco, C.; Morineau, D. *Solvation effects on self-association and segregation processes in tert-butanol-aprotic solvent binary mixtures*. The journal of physical chemistry. B 2013, 117, 10221-10230.
(199) Song, Z.; Song, Y.; Guo, J.; Feng, D.; Dong, J. *Effect of Nanopore Confinement on Fluid Phase Behavior and Production Performance in Shale Oil Reservoir*. Industrial & Engineering Chemistry Research 2021, 60, 1463-1472.
(200) Song, Y.; Song, Z.; Chen, Z.; Zhang, L.; Zhang, Y.; Feng, D.; Wu, Z.; Wu, J. *Fluid phase behavior in multi-scale shale reservoirs with nano-confinement effect*. Energy 2024, 289, 130027.
(201) Du, F.; Huang, J.; Chai, Z.; Killough, J. *Effect of vertical heterogeneity and nano-confinement on the recovery performance of oil-rich shale reservoir*. Fuel 2020, 267, 117199.
(202) Wang, Y.; Cao, R.; Jia, Z.; Huang, T.; Jia, P.; Cheng, L.; Duan, W.; Sun, Z. *Phase behavior and hydrocarbons distribution in shale oil during EOR with nano-confinement effect*. Frontiers in Energy Research 2023, 11.
(203) Korb, J.-P.; Nicot, B.; Louis-Joseph, A.; Bubici, S.; Ferrante, G. *Dynamics and Wettability of Oil and Water in Oil Shales*. The Journal of Physical Chemistry C 2014, 118, 23212-23218.
(204) Kausik, R.; Minh, C. C.; Zielinski, L.; Vissapragada, B.; Akkurt, R.; Song, Y.; Liu, C.; Jones, S.; Blair, E. In *Tilte*2011: SPE-147198-MS.
(205) Falk, K.; Coasne, B.; Pellenq, R.; Ulm, F.-J.; Bocquet, L. *Subcontinuum mass transport of condensed hydrocarbons in nanoporous media*. Nature Communications 2015, 6, 6949.
(206) Obliger, A.; Ulm, F.-J.; Pellenq, R. *Impact of Nanoporosity on Hydrocarbon Transport in Shales' Organic Matter*. Nano letters 2018, 18, 832-837.
(207) Obliger, A.; Pellenq, R.; Ulm, F.-J.; Coasne, B. *Free Volume Theory of Hydrocarbon Mixture Transport in Nanoporous Materials*. The Journal of Physical Chemistry Letters 2016, 7, 3712-3717.

(208) Watkins, L. P.; Yang, H. *Detection of Intensity Change Points in Time-Resolved Single-Molecule Measurements*. The Journal of Physical Chemistry B 2005, 109, 617-628.
(209) Yang, J.; Hatcherian, J.; Hackley, P. C.; Pomerantz, A. E. *Nanoscale geochemical and geomechanical characterization of organic matter in shale*. Nature Communications 2017, 8, 2179.
(210) Jubb, A. M.; Botterell, P. J.; Birdwell, J. E.; Burruss, R. C.; Hackley, P. C.; Valentine, B. J.; Hatcherian, J. J.; Wilson, S. A. *High microscale variability in Raman thermal maturity estimates from shale organic matter*. International Journal of Coal Geology 2018, 199, 1-9.
(211) Zhang, Y.; Li, D.; Xin, G.; Ren, S. *A Review of Molecular Models for Gas Adsorption in Shale Nanopores and Experimental Characterization of Shale Properties*. ACS Omega 2023, 8, 13519-13538.
(212) Lei, W.; McKenzie, D.: *Enhanced water vapour flow in silica microchannels and interdiffusive water vapour flow through anodic aluminium oxide (AAO) membranes*; SPIE, 2015; Vol. 9668. pp. AU.
(213) Myong, M. S.; Young, R. M.; Wasielewski, M. R. *Excimer Diffusivity in 9,10-Bis(phenylethynyl)anthracene Assemblies on Anodic Aluminum Oxide Membranes*. The Journal of Physical Chemistry C 2021, 125, 24498-24504.
(214) Zhao, L.; Zhong, Y.; Wei, Y.; Ortiz, N.; Chen, F.; Wang, G. *Microscopic Movement of Slow-Diffusing Nanoparticles in Cylindrical Nanopores Studied with Three-Dimensional Tracking*. Analytical Chemistry 2016, 88, 5122-5130.
(215) Ma, C.; Yeung, E. S. *Entrapment of Individual DNA Molecules and Nanoparticles in Porous Alumina Membranes*. Analytical Chemistry 2010, 82, 654-657.
(216) Higgins, D. A.; Park, S. C.; Tran-Ba, K.-H.; Ito, T. *Single-Molecule Investigations of Morphology and Mass Transport Dynamics in Nanostructured Materials*. Annual Review of Analytical Chemistry 2015, 8, 193-216.
(217) Han, R.; Wang, G.; Qi, S.; Ma, C.; Yeung, E. S. *Electrophoretic Migration and Axial Diffusion of Individual Nanoparticles in Cylindrical Nanopores*. The Journal of Physical Chemistry C 2012, 116, 18460-18468.
(218) Chen, F.; Neupane, B.; Li, P.; Su, W.; Wang, G. *Investigating axial diffusion in cylindrical pores using confocal single-particle fluorescence correlation spectroscopy*. ELECTROPHORESIS 2016, 37, 2129-2138.
(219) Hohlbein, J.; Steinhart, M.; Schiene-Fischer, C.; Benda, A.; Hof, M.; Hubner, C. G. *Confined Diffusion in Ordered Nanoporous Alumina Membranes*. Small 2007, 3, 380-385.
(220) Durand, N. F. Y.; Dellagiacoma, C.; Goetschmann, R.; Bertsch, A.; Märki, I.; Lasser, T.; Renaud, P. *Direct Observation of Transitions between Surface-Dominated and Bulk Diffusion Regimes in Nanochannels*. Analytical Chemistry 2009, 81, 5407-5412.
(221) Eid, J. S.; Müller, J. D.; Gratton, E. *Data acquisition card for fluctuation correlation spectroscopy allowing full access to the detected photon sequence*. Review of Scientific Instruments 2000, 71, 361-368.
(222) Fieller, E. C. *Some Problems in Interval Estimation*. Journal of the Royal Statistical Society. Series B (Methodological) 1954, 16, 175-185.
(223) Phan, A.; Cole, D. R.; Striolo, A. *Preferential Adsorption from Liquid Water–Ethanol Mixtures in Alumina Pores*. Langmuir 2014, 30, 8066-8077.

(224) Giles, J. H.; Gilmore, D. A.; Denton, M. B. *Quantitative analysis using Raman spectroscopy without spectral standardization*. Journal of Raman Spectroscopy 1999, 30, 767-771.
(225) Hamid Rashidi, A. N., Xiaoyu Wang, Michael J. Servis, Takashi Ito, and Daniel A. Higgins: *Adsorption and Solvation Modulate Rhodamine B Diffusion in Ethanol/Water-Filled Anodic Alumina Nanopores*. The Journal of Physical Chemistry, 2024.
(226) Gao, H.; Tatomir, A. B.; Karadimitriou, N. K.; Steeb, H.; Sauter, M. *Effect of Pore Space Stagnant Zones on Interphase Mass Transfer in Porous Media, for Two-Phase Flow Conditions*. Transport in Porous Media 2023, 146, 639-667.
(227) Karadimitriou, N. K.; Joekar-Niasar, V.; Babaei, M.; Shore, C. A. *Critical Role of the Immobile Zone in Non-Fickian Two-Phase Transport: A New Paradigm*. Environmental Science & Technology 2016, 50, 4384-4392.
(228) Hasan, S.; Niasar, V.; Karadimitriou, N. K.; Godinho, J. R. A.; Vo, N. T.; An, S.; Rabbani, A.; Steeb, H. *Direct characterization of solute transport in unsaturated porous media using fast X-ray synchrotron microtomography*. Proceedings of the National Academy of Sciences 2020, 117, 23443-23449.
(229) Dou, Z.; Zhang, X.; Zhuang, C.; Yang, Y.; Wang, J.; Zhou, Z. *Saturation dependence of mass transfer for solute transport through residual unsaturated porous media*. International Journal of Heat and Mass Transfer 2022, 188, 122595.
(230) Renkin, E. M. *Filtration, diffusion, and molecular sieving through porous cellulose membranes*. The Journal of general physiology 1954, 38, 225-243.
(231) Ma, C.; Han, R.; Qi, S.; Yeung, E. S. *Selective transport of single protein molecules inside gold nanotubes*. Journal of Chromatography A 2012, 1238, 11-14.
(232) Yamaguchi, A.; Mekawy, M. M.; Chen, Y.; Suzuki, S.; Morita, K.; Teramae, N. *Diffusion of Metal Complexes Inside of Silica−Surfactant Nanochannels within a Porous Alumina Membrane*. The Journal of Physical Chemistry B 2008, 112, 2024-2030.
(233) Nagumo, R.; Takaba, H.; Nakao, S.-i. *Accelerated computation of extremely 'slow' molecular diffusivity in nanopores*. Chemical Physics Letters 2008, 458, 281-284.